Molecular Crystals and Liquid Crystals
Publication details, including instructions for authors and subscription information:
http://www.tandfonline.com/loi/gmcl16

Acoustooptical Phenomena in Liquid Crystals

O. A. Kapustina [a]

[a] N. N. Andreev Institute of Acoustics, Academy of Sciences of the USSR, 4 Shvernik Street, Moscow, 11 7036, USSR

Version of record first published: 20 Apr 2011.

To cite this article: O. A. Kapustina (1984): Acoustooptical Phenomena in Liquid Crystals, Molecular Crystals and Liquid Crystals, 112:1-2, 1-164

To link to this article: http://dx.doi.org/10.1080/00268948408076296

Mol. Cryst. Liq. Cryst., 1984, Vol. 112, pp. 1–164
0026-8941/84/1122-0001/$18.50/0

Printed in the United States of America

Acoustooptical Phenomena in Liquid Crystals

O. A. KAPUSTINA

N. N. Andreev Institute of Acoustics, Academy of Sciences of the USSR, 4 Shvernik Street, Moscow 117036, USSR

Contents

The review considers various aspects of the influence of mechanical deformation on the macroscopic structure and optical properties of liquid crystals: type of deformation (compression or shear); deformation amplitude; relation between the acoustic wavelength, viscous wavelength, and liquid crystal layer thickness; mutual orientation of the wave vector and director; boundary conditions in the liquid-crystal cell (acoustically soft or acoustically rigid boundary); relation between the linear dimensions of the liquid crystal layer and the acoustic beam; acoustic parameters of the substrates of a liquid-crystal cell (stiffness, characteristic impedance, linear dimensions of the substrates vs. the acoustic wavelength). The following physical phenomena responsible for the orientation effects are discussed: acoustic flows, oscillating hydrodynamic flows, sound absorption, interaction between director oscillations and the velocity field. Specific features of acoustooptical phenomena near phase transitions are considered.

INTRODUCTION

The present development of acoustics largely depends on the penetration of its ideas and methods into allied fields, into engineering and technology. For example, the use of these ideas and methods in modern optics, optoelectronics,and laser engineering has led to a new branch of physics, acoustooptics, which studies, both theoretically and experimentally, a wide range of phenomena related to the interaction between acoustic and electromagnetic waves in solids and liquids.

The acoustooptical effect is observed in virtually all media, though it can find practical application only with materials satisfying the following requirements: transparency in a certain optical wavelength region, a rather high acoustooptical figure of merit, low sound absorption at operating acoustic frequencies. Modern liquid-crystal materials satisfy, as a rule, these requirements, and considerable sound absorption, typical of some materials, gives rise to structural transformations, which are rather interesting from the practical point of view.

A specific feature of acoustooptical phenomena in liquid crystals, as compared to true solid crystals, is related to the unique coexistence of the properties of solids and isotropic liquids: a liquid single crystal, just like a solid crystal, experiences a destabilizing torque produced by elastic deformation, and because of the low viscosity of liquid crystals this torque results in a rather quick molecular reorientation. Since the optical properties of liquid crystals are anisotropic, any structural transformation of these crystals can easily be detected by optical methods. Acoustooptical effect in liquid crystals—change in birefringence of nematic crystals under mechanical deformation—was discovered by O. Lehman in 1910 and interpreted by V. Zolina in the 1930's. Further investigations of 1960–70's pioneered by A. Kapustin anticipated many ideas which now underlie the physics and application of acoustooptical effects ("acoustical" dynamic light scattering, formation of spatially modulated structures under mechanical deformation produced by acoustic waves, detection of these deformations by polarization

modulation of light, etc.). However, practical value of these effects have become clear only quite recently, in connection with added interest in optical processing and display of acoustic information, because problems of this kind can be resolved efficiently with the aid of liquid crystals capable of directly converting sound to light.

At present, the acoustooptics of liquid crystals is a branch of physics which studies the influence of elastic deformations on these substances and related phenomena. Practical application of acoustooptical effects has enabled the design and manufacture of essentially new devices.

In recent years, innumerable facts have been gained in the field, certain progress has been made in understanding the physics of the phenomenon, and a number of investigations have been carried out which have important practical value. The major advances made in this field have been given coverage in our review where we have endeavoured to systematize and represent from a common standpoint the fundamental acoustooptical properties of liquid crystals.

I. ACOUSTOOPTICAL EFFECTS IN NEMATIC LIQUID CRYSTALS

All experimental studies of acoustooptical phenomena in liquid crystals under various elastic deformations are usually performed with a cell in which a liquid crystal layer[1] 15–500 μm thick is placed between the bounding surfaces[2,3] (plates or films) (Figure 1). An acoustic transducer[4] is either bonded to the cell via a thin adhesive layer (Figure 1a) or is in liquid[5]; the cell may be immersed in the liquid either completely (Figure 1b) or partially (with one surface) (Figure 1c). In experiments with shear and surface waves plate 3 acts either as the emitter vibrating in the plane (Figure 1d) or as the acoustic medium (Figure 1e). The gap between the plates is usually created by spacers[6] which may occupy the whole perimeter of the cell or only its part. Cells with free ends are also used sometimes. Two modes of the detection (and recording) of the optical effect are possible: transmission and reflection; in the latter case a reflecting coating[7] is deposited on plate 3. Orthoscopic and conoscopic methods are usually used to observe the crystal texture.

Although configurations shown in Figure 1 are rather simple, interpretation, comparison, and systematization of experimental data encounter considerable difficulties. The main point is that the acoustic field in a cell is evaluated only from indirect data (voltage across the acoustic transducer, acoustic intensity in the medium before and after the cell or in free space without cell, etc.). In some papers these data were used to calculate wave field in a liquid crystal layer. From the acoustical standpoint, however, a

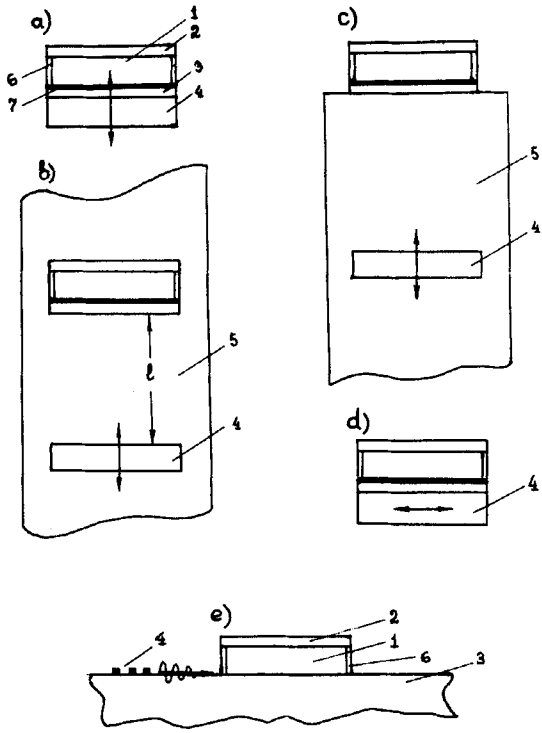

FIGURE 1 Experimental configurations for studying acoustooptical phenomena in liquid crystals. Cells in which a liquid crystal layer (1) is placed between the bounding surfaces (2) and (3) (plates or films). An acoustic transducer (4) is either bonded to the cell via a thin adhesive layer (Fig. 1a) or is a liquid (5); the cell may be immersed in the liquid either completely (Fig. 1b) or partially (with one surface) (Fig. 1c). In experiments with shear and surface waves plate 3 acts either as the emitter vibrating in the plane (Fig. 1d) or as the acoustic medium (Fig. 1e). The gap between the plates is usually created by spacers (6) which may occupy the whole perimeter of the cell or only its part. (7) is a coating deposited on plate 3 for reflection measurements.

cell is a three-layer system with complicated velocity and pressure fields. To find these fields and the input impedance of such a system, one has to solve a particular problem, depending on the vibration frequency, the thickness of the layer and bounding plates, the characteristic impedance of the plates, their stiffness and way of fixing in the cell, and also the vibration pattern on the layer boundaries. The acoustic intensity in the beam or particle velocity at the bounding plates are usually distributed inhomogeneously, and in some cases the wave field in the layer is the result of mixing of different modes. This is the case, for example, with a surface wave propagating at the substrate-liquid crystal interface, because such a wave is the superposition

of inhomogeneous longitudinal and shear waves whose amplitudes decay exponentially away from the interface. In this case a complicated interference pattern of the wave field in the medium can only be calculated by numerical methods.[1,2] The situation is much simpler in shear experiments, for only in this case can the vibrating plate amplitude be measured with a high accuracy.

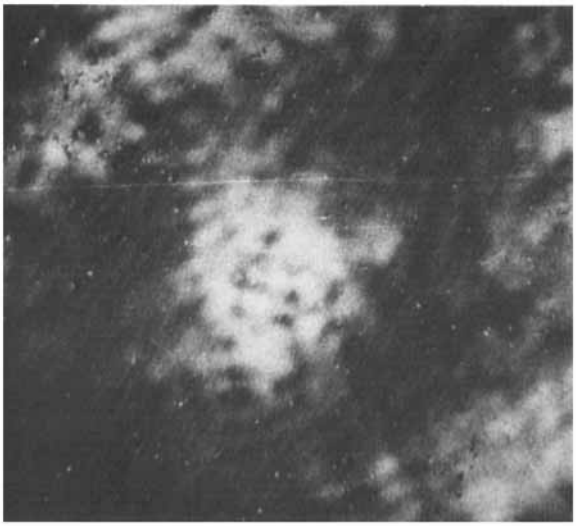

(a)

(b)

FIGURE 2 The clearing pattern of a homeotropic MBBA sample subjected to a homogeneous deformation (crossed polarizers): (a) longitudinal waves; $f = 3.2$ MHz; $d = 40$ μm; (b) surface waves; $f = 18$ MHz; $d = 15$ μm.

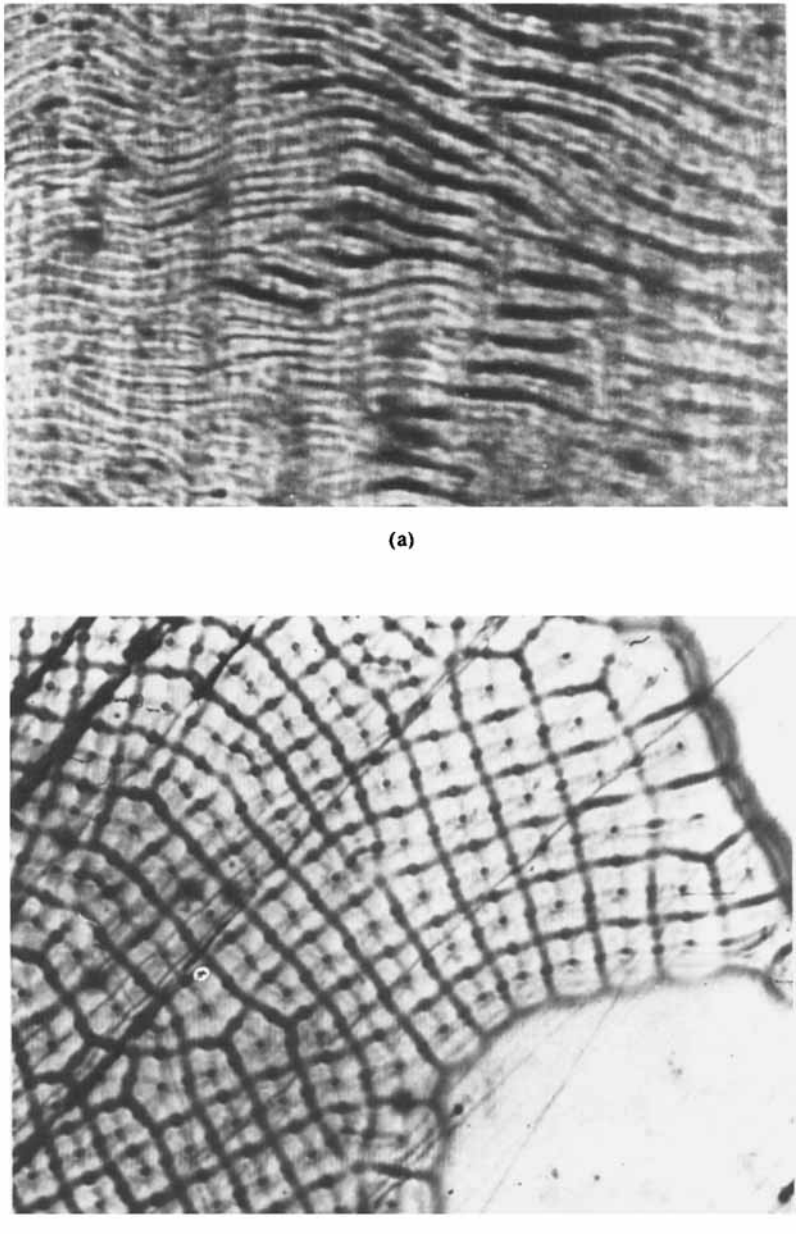

FIGURE 3 The pattern of one-dimensional and two-dimensional spatial-periodic deformation of planar samples: (a) MBBA; $d = 40\ \mu m$; $f = 3.2$ MHz; longitudinal waves; (b) LC-404 (97%) + cholesteryl caprinate (3%); $d = 40\ \mu m$; $P_0 = 4.2\ \mu m$; $f = 3.2$ MHz; longitudinal waves.

(a)

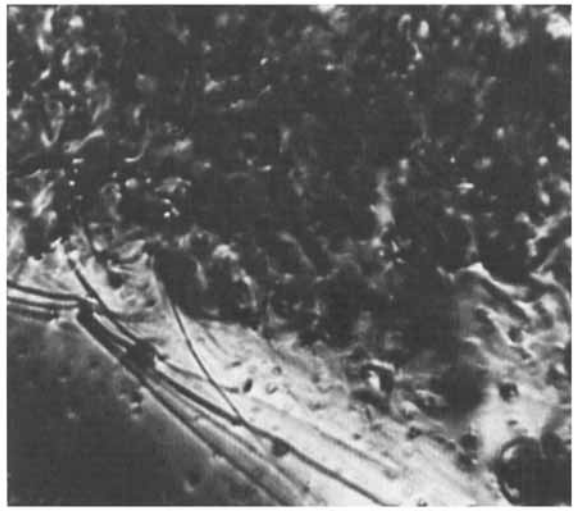

(b)

FIGURE 4 The stage of inhomogeneous deformation. (a) homeotropically oriented MBBA; $d = 40\ \mu m$; $f = 3.2$ MHz; longitudinal waves; (b) LC-404 (97%) + cholesteryl caprinate (3%); $d = 40\ \mu m$; $P_0 = 4.2\ \mu m$; $f = 3.2$ MHz; longitudinal waves.

Besides the factors just mentioned, several different mechanisms[3] may simultaneously take place in experiment or "parasitic vibrations" may be involved,[4] and this is not always taken into account in the interpretation of experimental data.

Acoustic waves propagating in a medium produce compression and shear deformations. These elastic disturbances affect differently the structure of liquid crystals and, therefore, their optical properties, depending on the amplitude and type of deformation, relation between the acoustic wavelength and sample dimensions, orientation of the wave vector relative to the director, and also on experimental geometry (the initial layer structure, boundary conditions at the ends, the width and homogeneity of the acoustic beam, stiffness of the bounding plates, etc.).

With respect to deformation amplitude, one may distinguish three stages of structural transformations, each being characterized by a certain degree of the director field disorder:

a) homogeneous deformation, when the oscillating or stationary distortion of the layer orientation duplicates the distribution (over the layer plane) of the disturbing factor (acoustic intensity, displacement, etc.) (Figures 2a and b);

b) spatially periodic deformation, producing one-dimensional or two-dimensional periodic structure in the layer, which reflects the director orientation distribution (Figures 3a and b);

c) inhomogeneous deformation, when the structure is completely disordered and a polycrystalline texture with random director distribution arises (Figures 4a and b).

Below we shall consider all these stages of structural transformations in homeotropic- and planar-oriented nematic crystals for two types of mechanical deformation: compression and shear.

I.1. Homogeneous deformation

I.1.1. Homeotropic orientation

The effect of mechanical deformation on birefringence was first observed by O. Lehman[5] for a homeotropically oriented layer of ethyl para-azoxycinnamate placed between rotating glass plates (observations were made by the conoscopic method). More recent experiments have shown that the conoscopic pattern depends on the rotation speed, layer thickness, and temperature.[6,7] By an elegant experiment with samples of variable thickness V. Zolina has clearly demonstrated that the mechanical disturbance alters the direction of the molecular axes.[8] A. Kapustin was the first to observe periodic oscillations of the director by applying a single mechanical pulse (of momentum 4 g cm/sec) to a homeotropic nematic layer.[9] Some time

later, a similar effect was observed in a 20 μm layer of ethyl *p*-ethoxybenzalamino-α-methylcinnamate in the nematic phase (93–122°C) at frequencies 20 Hz–20 kHz under shear deformation.[10] In the works just mentioned only qualitative results were obtained, so that these papers are cited in the literature rather seldom. Nevertheless, they have anticipated many contemporary trends in the field. For example, in Ref. 9 a possibility was reported, for the first time, of using liquid crystals for detecting mechanical deformation.

To describe the optical properties of nematics under deformation, we consider a homeotropic liquid crystal (of thickness d and width L) in a parallel polarized light beam which passes through the layer along the director orientation **n**. No birefringence is observed in this case; but as the layer is deformed so that the director tilts through the angle $\varphi(x, z)$, birefringence does appear. The familiar formula of crystal optics,[11] in which variation of the molecular orientation over the layer thickness is taken into account, leads to the following expression for the intensity of light passing through the layer and analyser:

$$I = I_0 \sin^2\left[\frac{\Delta n}{2} k_0 \int_{-d/2}^{d/2} \varphi^2(x, z)\, dz\right] \sin^2 2\theta_0. \tag{1}$$

Here I_0 is the intensity of the incident linearly polarized light, $\Delta n = n_{\parallel} - n_{\perp}$, $n_{\parallel}$ and $n_{\perp}$ are the refractive indices along the director orientation and in the transverse direction, respectively, k_0 is the wave vector of light in vacuum, θ_0 is the angle between the polarization plane of incident light and the plane (x, z). Depending on the deformation amplitude and, therefore, the phase delay $nk_0 \int_{-d/2}^{d/2} \varphi^2(x, z)\, dz$ between the ordinary and extraordinary rays, the transmitted intensity of light oscillates, the maximal oscillation amplitude being at $\theta_0 = 45°$.

The layer structure distortion and the change in the director orientation are caused by two competing factors: the stabilizing elastic moment $K_i(\partial^2\varphi/\partial z^2)$ and the deformation-induced destabilizing torque (K_i is Frank's elastic constant).

We now consider the theoretical models for the mechanisms of this destabilizing torque and discuss, relying upon these models, the most important experimental results.

A. Compression deformation

Depending on the relationship between the layer thickness d and viscous wavelength $\lambda_{vis} = 2\pi/q_{vis}$ we distinguish three frequency regions: 1) $\lambda_{vis} \ll d$; 2) $\lambda_{vis} \gg d$; 3) $\lambda_{vis} \sim d$. Here $q_{vis} = \sqrt{\rho\omega/2\eta}$ is the viscous wave

number, ρ and η are the density and dynamic viscosity of the nematic crystal in question. The choice of λ_{vis} as a criterion for these frequency regions is by no means arbitrary. The fact is that the spatial scales (the ratio of the size of the region where acoustic field is produced to the acoustic wavelength) have such values that, from the acoustical standpoint, we deal only with thin layers where viscous wave fields become especially important.[12] Indeed, strong absorption of viscous waves gives rise to high particle velocity gradients in a thin layer, which in turn leads to significant torques. We shall see below that these torques may suppress the stabilizing elastic moment, thereby resulting in reorientation of the molecular ensemble in the layer.

High frequencies. First, we consider the most common case of high frequencies where the layer thickness is much larger than the viscous wavelength. Depending on mutual orientation of the director and wave vector, two situations are possible, which are characterized by qualitatively different effects.

(a) The wave vector $k \| \mathbf{n}$ and coincides with the normal to the layer.

In Refs. 13–15 the tilt of molecules under periodic compression is interpreted as a threshold effect caused by non-linear stress proportional to the tilt angle and particle velocity. However, the theoretical values of the threshold acoustic intensity thus obtained are 2–3 orders of magnitude higher than the values usually attained in experiment.† Furthermore, most recent experiments[16–18] performed on homogeneously deformed nematic crystals have revealed no characteristic thresholds other than the "apparent" thresholds caused by the sensitivity limit of measuring instruments[16,17] (e.g., by the degree of opacity of crossed polarizers[18]). Thus, the models[13–15] predicting the existence of a threshold have failed and become inadequate now.

Nagai, Peters, and Candau suggested a mechanism based on the second-order effect—acoustic flows—and performed calculations for a bounded acoustic beam when the effective "acoustic force" $\mathbf{F}$ caused by sound absorption in the medium and producing flows in the insonified region is of the form[19]:

$$\mathbf{F} = \begin{cases} 0, \quad 0, \quad \dfrac{2\alpha J_s}{c}; & |x| < \mathscr{D}/2 \\ 0, & \mathscr{D}/2 < |x| < L/2 \end{cases} \tag{2}$$

†Only Nagai and Iizuka[14] could obtain high acoustic intensities which correlated with their threshold deformation model. Unfortunately, the paper does not report the experimental procedure for measuring these threshold values.

Here α is the absorption coefficient, J_s is the incident acoustic intensity, c is the acoustic velocity in the medium, $\mathscr{D}$ is the transducer diameter. The hydrodynamic problem is thus reduced to finding the flow velocity spatial distribution in the insonified region from the Navier-Stokes equation which describes the behaviour of an ordinary isotropic liquid[20] with an allowance for specific features inherent in a nematic: viscosity anisotropy and correla-

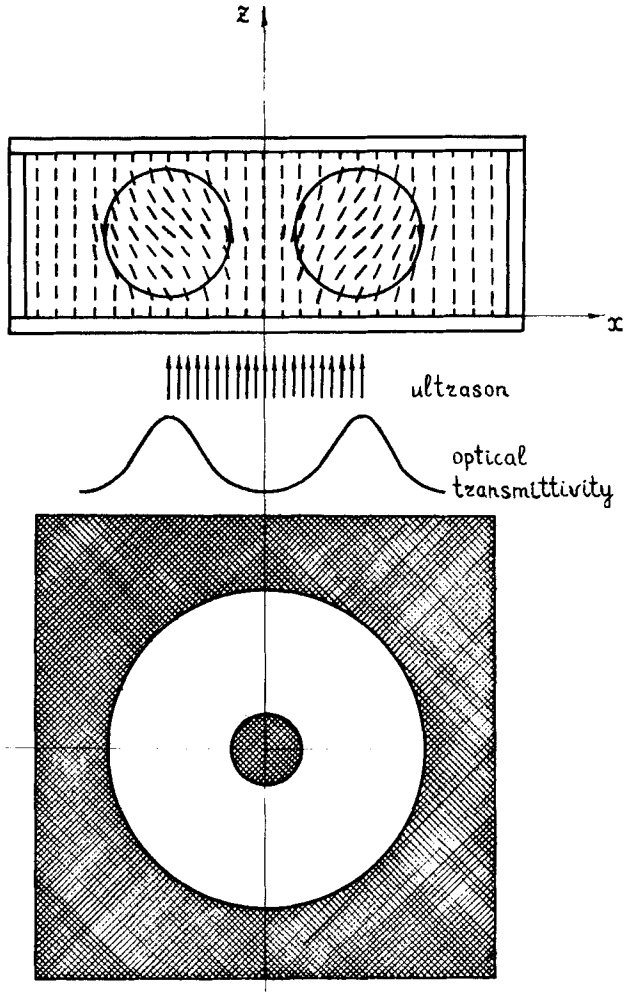

(a)

FIGURE 5 The Nagai-Peters-Candau model for the mechanism of director reorientation in an acoustic field (a); the distribution of streamlines and velocity isolines (b) (oblique incidence of sound).

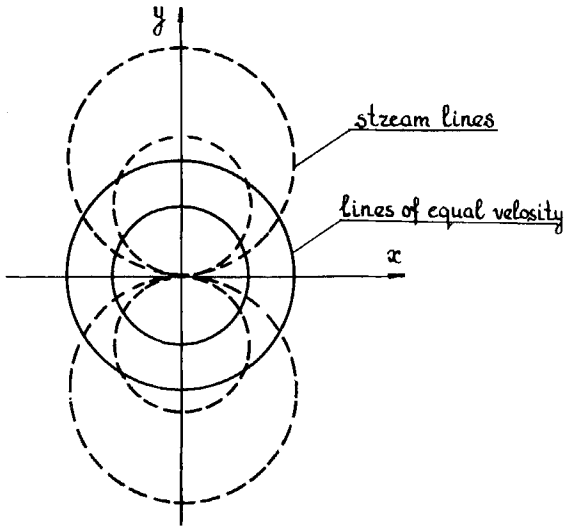

(b)

FIGURE 5 (*Continued*)

tion between the flow direction and molecular orientation.[21] For a bounded acoustic beam (condition (2)) this distribution shows that within the irradiated region the flow is directed along the z-axis away from the transducer and outside the region, in the opposite direction (Figure 5a). The steady-state flow results in reorientation of the molecules. Omitting bulky calculations, we write down only the final results for the orientation pattern

$$\varphi_2(x, z) = \alpha J_s. \tag{3}$$

An analysis of the complete expression for $\varphi_2(x, z)$ (which is not presented here) shows that this distribution has the following specific features: 1) φ_2 is maximal along z at $z = d/2$ and symmetric about the x-axis; 2) at $z = d/2$, the variation of φ_2 along the x axis is symmetric about point $x = 0$; φ_2 attains a maximal value at the beam boundary ($x = \mathscr{D}/2$) where the flow velocity gradient is maximal and vanishes at $x = 0$ and $x = L/2$; 3) for $z = d/2$ and $\mathscr{D}/L = \text{const}$, φ_2 increases with the radius $L/2$ of the insonified region; 4) the value of φ_2 corresponding to the beam boundary depends on the ratio $\mathscr{D}/L$, reaching a maximum at $\mathscr{D}/L = 0.5$. However, this orientation pattern (Figure 5a) does not correlate with the pattern observed in practice. Experiment reveals maximal clearing of the layer in the central region of the acoustic beam, rather than at the boundaries. Nor does

experiment confirm the theoretical values of optical transmissivity as calculated by Eq. (1) for the distribution $\varphi_2(x, z)$ predicted by this model. For example, the estimates show that with a 100 μm MBBA sample for $\mathscr{D}/L = 0.5$ and $L = 3$ cm the optical transmissivity $I/I_0 = 0.3$ can be obtained with acoustic intensity 2 W/m^2, which is about two orders of magnitude less than the value observed under experimental conditions corresponding to this calculation.[19] The authors of the model attribute this discrepancy to a more complicated flow pattern in a real cell due to acoustic field inhomogeneities.

In our opinion, there are more profound reasons for this discrepancy. Acoustic flows in a travelling wave field with $\mathscr{D}/L \simeq 0.3$ were studied in Ref. 22 where it was found that such a flow becomes steady-state at a distance not less than $z_{\max} = 1/2\alpha$ (α is the sound absorptance). At frequencies 2.1 and 6.3 MHz the experimental values of $z_{\max}$ are 1 cm and 0.5 cm, respectively, which exceeds the liquid crystal thickness in actual cells.[22] Furthermore, expression (2) for the flow intensity in the Nagai-Peters-Candau theory is valid only under travelling-wave conditions for $\alpha d > 1$, which is not true in real cells. Thus, the steady-state structure distortion cannot be explained within the framework of this theory.

In the papers discussed above the effect of boundary conditions at the layer edges was not taken into account. The importance of this fact was first pointed out by Sripaipan, Hayes, and Fang[23] who suggested an interesting physical interpretation of director reorientation in a layer with free edges $x = -L/2$, $x = L/2$ (the so-called acoustically soft boundary) (Figure 6).

We now consider this model, defining the motion of the bounding plates in the form

$$V_z|_{z=d/2} = V_z|_{z=-d/2} = V_0\psi(x)\cos\omega t; \qquad V_x|_{z=\pm d/2} = 0. \tag{4}$$

The function $\psi(x)$ describes the compression distribution over the layer width; $\psi(x) \leq 1$.† Since the layer edges are free, vibration of the bounding plates gives rise to a periodic motion of the liquid along the axis Ox, thereby resulting in a longitudinal standing wave with node and anti-node lines parallel to the layer free edges. This wave induces flows with a scale determined by the acoustic wavelength (Rayleigh flows),[24] so that the director orientation **n** is distributed periodically along the Ox axis (see Figure 6).

†If the layer is placed in an acoustic field, $\psi(x)$ describes the acoustic intensity distribution over the layer width.

A rigorous theoretical treatment of the model† for the case where $\psi(x) = \sin kx$‡ gives the following expressions for the director tilt and optical transmissivity[25]:

$$\varphi_2(x, z) = -\frac{\rho_0 V_0^2 \eta_1}{4K_3\mu} \sin 2kx \left(-\frac{z}{2} + \frac{2z^3}{d^2}\right)\left(-\frac{\alpha_2}{\eta_2}\right) B, \tag{5}$$

$$\frac{I}{I_0} = \sin^2\left[\frac{25\Delta n k_0 d^3 \rho_0 \xi_0^4 \omega \eta_1^2 c^2 \alpha_2^2}{7 \cdot 2^7 \mu^2 K_3^2 \eta_2^2} \sin^2 2kx B^2\right] \sin^2 2\theta_0, \tag{6}$$

where

$$B = \left[1 - \frac{\mu_3 + \alpha_1 + \alpha_6 + \alpha_2}{\eta_1} - 4\frac{\mu_3 + \alpha_5 - \alpha_2 - \eta_1}{\mu}\right],$$

α_i and μ_i are Leslie's viscous coefficients, $\eta_1 = (\alpha_2 + \alpha_5 + \alpha_6)/2$, $\eta_2 = (-\alpha_2 + \alpha_4 + \alpha_5)/2$, ξ_0 is the vibration amplitude.

Expression (5) implies that the spatial period of the distribution of **n** along the Ox axis is 0.25λ. This agrees with experimental results obtained (under conditions adequate to the theoretical model) for MBBA samples 25 μm and 70 μm thick in the frequency range 640–1330 kHz. According to these results, the period of the layer clearing pattern, which represents alternating bright and dark fringes parallel to the free edges, is $(0.29 \pm 0.08)\lambda$.[23] Figure 7 shows the transmitted intensity of light I passing through a bright fringe area and analyser as a function of the transducer voltage U ($d = 70$ μm, $f = 669$ kHz) (experiment is performed in the transmission mode, in accordance with configuration of Figure 1a).

The first transmissivity maximum on this curve is observed at acoustic intensity $J_s^{\max} = 200$ W/m^2, which agrees within an order of magnitude with the theoretical value predicted by Ref. 6.

Solution of the problem for an arbitrary function $\psi(x)$ gives the following expressions[25]:

$$\varphi_2(x, z) = -\frac{2\pi V_0^2 \alpha_2^2}{\omega K_2 k^2 L \eta_2}\left(1 - \frac{\eta_1}{2\alpha_2}\right)\psi(x) F(x)\left(\frac{z^3}{d^3} - \frac{z}{4d}\right), \tag{7}$$

†While calculating waves in a liquid crystal layer, Sripaipan *et al.* used incorrect dispersion relations. Hydrodynamics of liquid crystals does not predict waves (considered in their theory[23]) with the wave number $\kappa \simeq (1 + i)k^2/2q_{vis}$ ($\kappa^2 = k^2 - p_m^2$), where $p_m = 2\pi m/L$ are the characteristic wave numbers of the cell. This also led to the wrong expression for the transmissivity.

‡The bounding plate vibration amplitude obeys this law provided the wave number in the liquid crystal **k** for a frequency ω is close to one of the characteristic wave numbers p_m of the cell, i.e. the inequality $|k^2 - p_m^2| \ll (\mu/2\eta_1) p_m^2/q_{vis} d$ is valid.

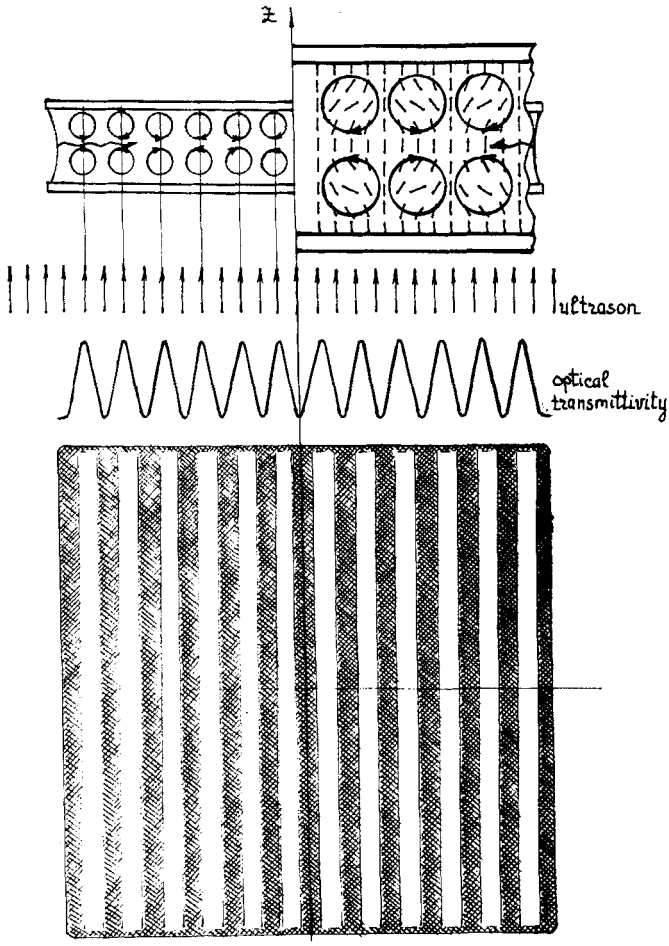

FIGURE 6 The Sripaipan-Kozhevnikov model for the mechanism of director reorientation in an acoustic field; the layer edges are free (acoustically soft boundary).

where

$$F(x) = \sum_{m=1}^{\infty} \frac{b_m m\left[1 - \frac{p_m^2}{k^2}\left(1 - \frac{\mu}{\eta_1}\frac{2}{q_{\text{vis}}d}\right)\right]\cos p_m x}{\left[1 - \frac{p_m^2}{k^2}\left(1 - \frac{\mu}{\eta_1 q_{\text{vis}}d}\right)\right]^2 + \left[\frac{p_m^2}{k^2}\frac{\mu}{\eta_1 q_{\text{vis}}d}\right]^2},$$

$$\frac{I}{I_0} = \sin^2\left[\frac{\pi^2 \Delta n k_0\, d\rho_0\, \alpha_2^4 \xi_0^4 c^4}{820\eta_1 K_3^2 L^2 \eta_2 \omega}\left(1 - \frac{\eta_1}{2\alpha_2}\right)\psi^2(x) F(x)\right]\sin^2 2\theta_0. \quad (8)$$

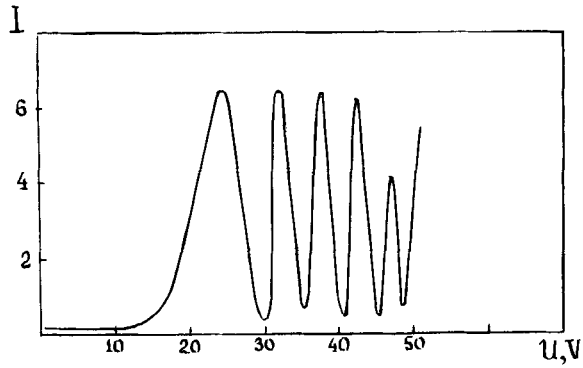

FIGURE 7 Optical transmittance, I, of monochromatic light vs. U, the voltage across the acoustic transducer; MBBA; $d = 70\ \mu$m; $f = 669$ kHz; $\lambda_0 = 6327$ Å.

To obtain numerical estimates, we set $\psi(x) \equiv 1$. For an MBBA sample of $d = 100\ \mu$m and $L = 2$ cm we obtain at a frequency of 1 MHz: $F(x) \cong 30 \cos kx$ and $J_s^{\max} = 160$ W/m^2. In this case the layer with free edges reveals a pattern of alternating bright and dark fringes whose width and contrast depend on the bounding plate vibration amplitude. The walls of a gas bubble inserted in a layer may act as free edges; in this case the fringes are circular. Such a pattern of alternating circular fringes (rings) was observed[23] in a 70 μm MBBA sample at 0.84 MHz. Unfortunately, there are no reliable quantitative data obtained under experimental conditions corresponding to this calculation.

We now consider the behaviour of a layer when the incident acoustic beam of finite width passes through the layer and is partially reflected from a rigid boundary to result in a compression standing wave whose aperture is equal to the beam width. In this case boundary conditions (6) take the form

$$V_z|_{z=d/2} = V_0\psi(x)\cos\omega t, \qquad V_z|_{z=-d/2} = 0. \tag{9}$$

If the intensity of the acoustic beam drops very sharply at its periphery, rather strong pressure gradients will arise at the beam border (irrespective of the boundary conditions at the layer edges) because the pressure is zero outside the beam. These pressure gradients give rise to longitudinal particle vibrations in the liquid layer, that is to longitudinal waves propagating along the Ox axis both into and outside the beam. Moreover, if the acoustic intensity is distributed non-uniformly across the beam, longitudinal waves are also excited in the layer inside the beam area. Besides longitudinal motion, the layer also experiences compression inside this area. The time-averaged forces, proportional to the product of the velocities of these

vibrations, result in a steady-state flow, and the velocity gradients of this flow make the director tilt (Figure 8).

In an infinitely extending layer, when the liquid flow and molecular alignment are confined to the plane (x, z) (two-dimensional case), the hydrodynamic destabilizing moment $\gamma(dV_x^{(2)}/dz)$ in a steady-state flow causes the director to tilt through the angle[26]

$$\varphi_2(x, z) = \frac{\rho V_0^2 \gamma}{2\sqrt{2}\, k q_{\text{vis}} \eta_2 K_3} \times \left\{ F_1(x) \left[\left(\frac{z}{d}\right)^3 + \frac{1}{2}\left(\frac{z}{d}\right)^2 - \frac{1}{4}\left(\frac{z}{d}\right) - \frac{1}{8} \right] + F_2(x)(kd)^{0.5} \left(\frac{\rho c d}{2\eta}\right)^{0.5} \left[\frac{1}{60}\left(\frac{z}{d}\right)^5 + \frac{1}{24}\left(\frac{z}{d}\right)^4 - \frac{1}{120}\left(\frac{z}{d}\right)^3 - \frac{1}{48}\left(\frac{z}{d}\right)^2 + \frac{1}{960}\left(\frac{z}{d}\right) + \frac{1}{384} \right] \right\}, \tag{10}$$

where

$$F_1(x) = \left\{ \cos\left[k\left(\frac{l}{2} - x\right) - \frac{\pi}{4} \right] e^{\delta(x - l/2)} - \cos\left[k\left(\frac{l}{2} + x\right) - \frac{\pi}{4} \right] e^{-\delta(x - l/2)} \right\} \psi(x),$$

$$F_2(x) = \left\{ \sin\left[k\left(x + \frac{l}{2}\right) \right] e^{-\delta(x - l/2)} + \sin\left[k\left(x - \frac{l}{2}\right) \right] e^{\delta(x - l/2)} \right\} \psi(x).$$

$\gamma = \alpha_3 - \alpha_2$; $\eta_2 = \frac{1}{2}(-\alpha_2 + \alpha_4 + \alpha_5)$; $\delta = k/2q_{\text{vis}}d$ is the attenuation coefficient for longitudinal waves in the layer. This leads to the following expression for the transmissivity:

$$\frac{I}{I_0} = \sin^2\left\{ \frac{\Delta n k_0\, d\rho\, V_0^2 \gamma^{2\eta}}{840 k^2 \omega \eta_2 K_3^2} N(x) \right\} \sin^2 2\theta_0. \tag{11}$$

Here

$$N(x) = F_1^2(x) = -3.15 \cdot 10^{-2} (kd)^{2.5} \left(\frac{\rho c d}{2\eta}\right)^{0.5} F_1(x) F_2(x) + 2.9 \cdot 10^{-4} \frac{(kd)^5 \rho c d}{2\eta} F_2(x)$$

is the function describing the transmissivity distribution over the layer. Outside the beam (for $|x| > l/2$) the function $N(x) \equiv 0$. The transmissivity

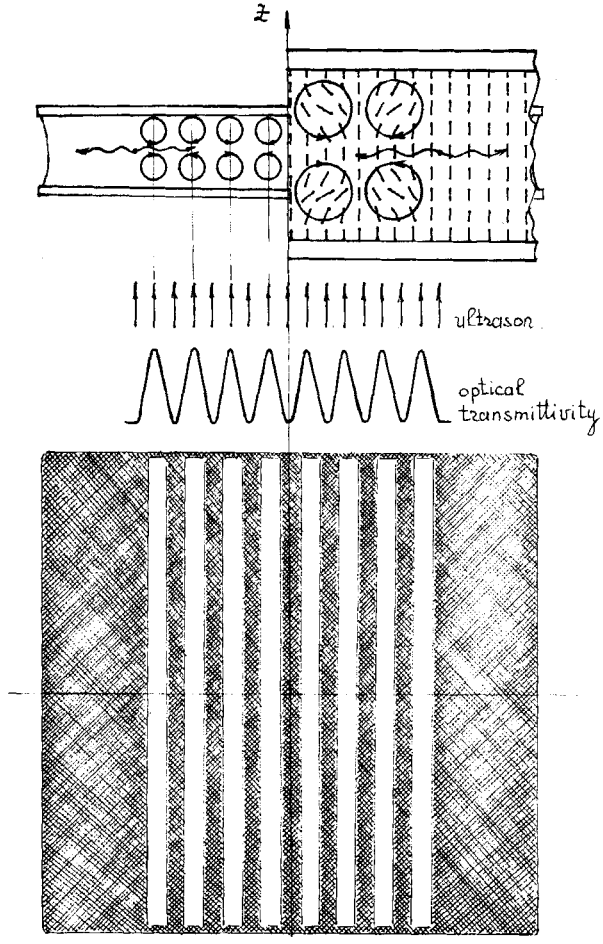

FIGURE 8 The Kozhevnikov model for the mechanism of director reorientation in an acoustic field; an infinitely wide layer.

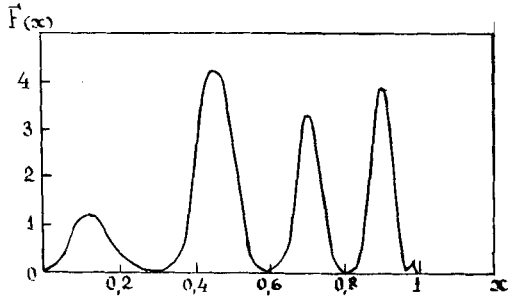

FIGURE 9 Distribution of optical transmittance across the layer width within the acoustic beam; MBBA; $d = 100\ \mu$m; beam width = 1 cm; $f = 1$ MHz.

distribution within the beam area is illustrated in Figure 9 for a 100 μm MBBA sample, beam width $l = 2$ cm, and frequency 1 MHz. It can be seen that for $|x| \leq l/2$ the layer exhibits a pattern of alternating dark and bright fringes spaced at about the acoustic wavelength.

Expressions (10) and (11) describe, respectively, the steady-state structure distortion and optical effect in the two-dimensional case where the beam cross-section is an elongated strip of constant width. For a circular acoustic beam of radius R with boundary conditions (9) (in which $\psi(x)$ is replaced by $\psi(R)$), the hydrodynamic destabilizing torque $\alpha_2(\partial V_r^{(2)}/\partial z)$ in a steady-

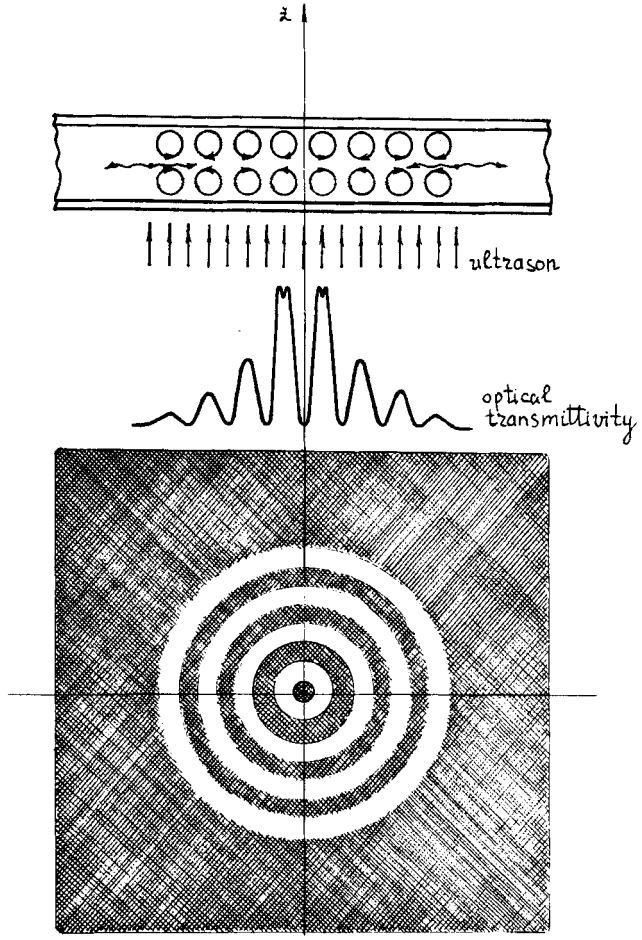

FIGURE 10 The Kozhevnikov model for the mechanism of director reorientation in an acoustic field; infinitely wide layer; bounded acoustic beam of radius R.

state flow tilts the director through the angle (Figure 10),[27]

$$\varphi_2 = (r, z) = \frac{V^2 \rho d_2}{\eta_2 K_3 k q_{\text{vis}} d} \left\{ \frac{1}{4} \left(\frac{2z^3}{d^2} + \frac{z^2}{d} - \frac{z}{d} - \frac{d}{4} \right) F_1(r) + \frac{3}{q_{\text{vis}}} \left(\frac{r^3}{d^3} - \frac{r}{4d} \right) F_2(r) \right\}, \tag{12}$$

where the functions F_1 and F_2 describe the radial distribution of the molecular axes tilt

$$F_1 = \sqrt{\frac{R}{r}} \left\{ e^{-\delta(R-r)} [\cos k(R-r) + \sin k(R-r)] + e^{-\delta(R+r)} [\cos k(R+r) + \sin k(R+r)] \right\} \psi(r),$$

$$F_2 = \frac{R}{r} e^{-\delta R} \cos 2kr \psi(r).$$

The layer transmissivity is given by

$$\frac{I}{I_0} = \sin^2 \left[\frac{\Delta n k_0 \alpha_2^2 V_0^4 \rho^2 d}{840 K_3^2 \eta_2^2 k^2 q_{\text{vis}}^2} F(r) \right] \sin^2 2\theta_0, \tag{13}$$

where the function

$$F(r) = F_{1(r)}^2 + \frac{3}{2q_{\text{vis}} d} F_1(r) F_2(r) + \frac{9}{2(q_{\text{vis}} d)^2} F_2^2(r)$$

describes the clearing distribution over the layer width. Outside the beam $F(r) \equiv 0$; within the beam area the distribution depends on the layer thickness. Figure 11 shows the behaviour of $F(r)$ for 10 μm and 100 μm MBBA samples (curves 1 and 2, respectively); $f = 1$ MHz. In a thicker layer, when $\delta R = kR/2q_{\text{vis}} d < 1$, longitudinal waves attenuate weakly and are focused at the layer centre where the optical effect (clearing) should be maximal. In a thinner layer, where $\delta R > 1$, attenuation of longitudinal waves makes the effect less pronounced at the centre and more pronounced at the edges. In both cases the layer reveals a pattern of alternating dark and bright fringes spaced at about the acoustic wavelength. If the sound intensity is homogeneous within the beam area, dark regions corresponding to the angles $\theta_0 = \pi/2p$ ($p = 0, 1, 2, 3$) should be observed in the layer plane.

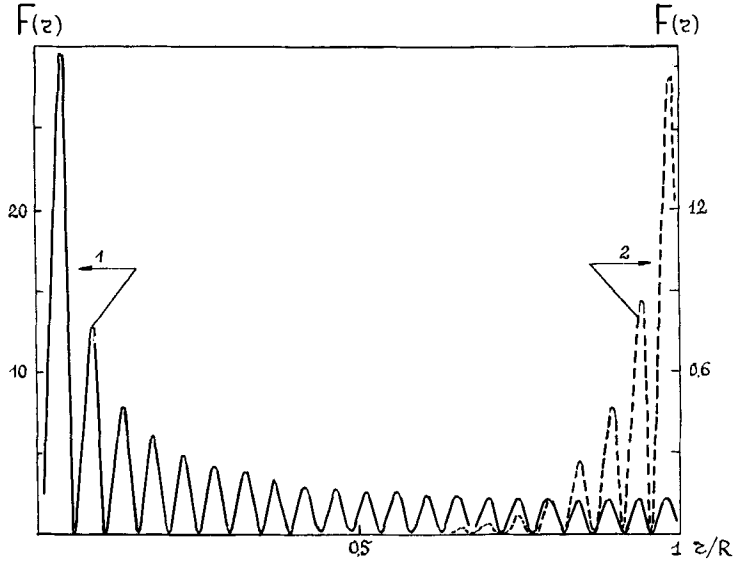

FIGURE 11 Distribution of optical transmittance across the layer width within the acoustic beam; MBBA; $f = 1$ MHz; $d = 100$ μm (curve 1); $d = 10$ μm (curve 2).

Expressing the amplitude of particle velocity V_s in the incident acoustic beam in terms of the plate vibration amplitude V_0 by the relation $V_s \simeq V_0/2kd$, we can write (13) in the form

$$\frac{I}{I_0} = \sin^2\left\{\frac{4\Delta n k_0 \eta \alpha_2^2 \omega d^5 J_s^2}{105 K_3 \eta_2^2 c^4} F(r)\right\} \sin^2 2\theta_0, \tag{13a}$$

where $J_s = \rho c V_s^2$. This expression implies that for small J_s the ratio $I/I_0 \sim J_s^4$. Introducing the effective clearing threshold J_s^{th} as the acoustic intensity at which $I/I_0 = 10^{-2}$, we obtain from (13a)

$$\begin{aligned} J_s^{\text{th}} &\sim \omega^{-0.5} d^{-2.5} && \text{for } \delta R < 1 \text{ (thick layer)} \\ J_s^{\text{th}} &\sim \omega^{-0.5} d^{-2.5} e^{-\delta(R-r)} && \text{for } \delta R > 1 \text{ (thin layer).} \end{aligned} \tag{14}$$

For a 100 μm MBBA layer at 1.6 MHz and $\theta_0 = \pi/4$ we have the following numerical estimates for $R = 1$ cm and $r = 0.04R$ when $F(r) \simeq 30$: $J_s^{\text{th}} = 1.68$ W/m^2 and $J_s^{\max} = 4.5$ W/m^2.

Bruchmüller[18] studied the effect of a focused acoustic beam of small cross-section area on a 55 μm MBBA layer. He did observe both steady-state flows and alternating dark and bright fringes. The transmissivity within one

fringe area was found to be proportional to $J_s^{3.9}$, which also agrees with theoretical predictions. However, the experimental ratio I/I_0 is as low as 0.1 for an acoustic intensity of 90 W/m^2 (f = 890 kHz), indicative of higher J_s^{th} values as compared to those predicted by the theory. This discrepancy can be attributed to beam geometry. As was pointed out by Guyon and Pieranski,[28] a focused beam induces additional flows which close up outside the irradiated region and distort the layer structure. This distortion is not taken into account by the theory developed for a flat acoustic beam and an infinitely extending layer. The latter condition ($L \to \infty$) seems to be rather important. For example, in flat-beam experiments performed with a 200 μm MBBA sample at 1.9 MHz (the ratio of the transverse dimensions of the beam and cell is $\sim$ 0.5) the threshold acoustic intensity J_s^{th} is $\sim$ 40 W/m^2,[19] which is an order of magnitude higher than the theoretical value for a layer of infinite width.

Let us now turn to the optical effect observed in a liquid crystal layer of radius R in a cell with fixed periphery (acoustically rigid boundary). One of the bounding plates is fixed, the other (thin plate or film) can move perpendicular to the layer plane everywhere except the region adjacent to the layer periphery. In this case, inhomogeneous layer compression near the fixed boundary due to plate bending produces longitudinal waves which, in turn give rise to a steady-state flow. As is shown in Ref. 27, if the centre of the plate moves according to the law $V_0 \cos \omega t$, the area of flexure and inhomogeneous compression has the size $b \simeq (A/\rho_p H\omega^2)^{1/4}$, where $A = E_p H_2^3/[12(1 - \nu_p)^2]$ is the plate flexural stiffness; E_p, ν_p, and ρ_p are Young's modulus, Poisson's ratio, and density of the plate, respectively; H is the plate thickness ($H < \lambda$). If $kb < 1$, the amplitude of the longitudinal particle velocity in the layer is

$$V_r|_{r=R-b} \approx V_0 \frac{b}{d}$$

For $r < R - b$, the problem is reduced to that considered above when an acoustic beam of radius ($R - b$) falls onto an infinitely extending layer, so that expression (13a) is valid if $R - b$ is substituted for R and the factor $(2kb)^2$ is inserted into the expression in curly brackets. We have then

$$J_s^{\text{th}} \sim \omega^{-1} d^{-2.5}. \tag{15}$$

The clearing pattern is the same as for an infinitely extending beam. Let us make some estimates. For a 100 μm MBBA sample at 1.6 MHz we obtain

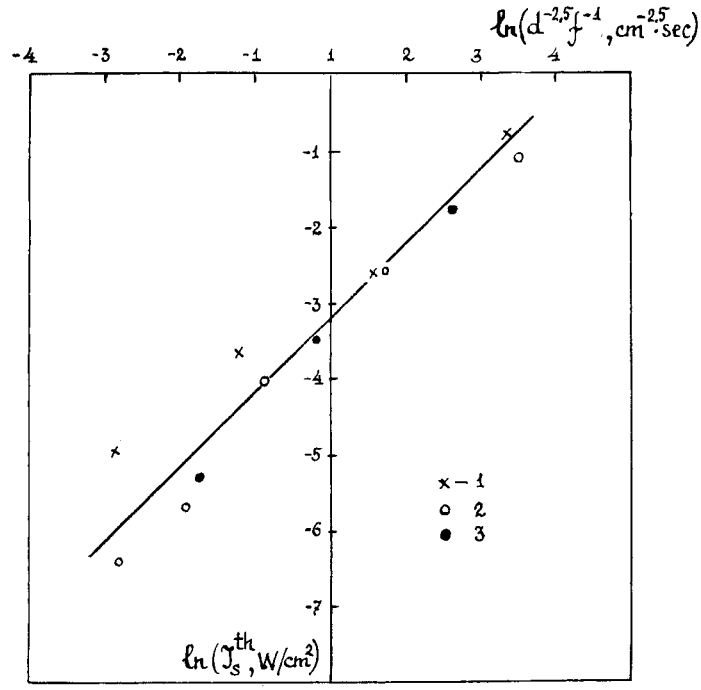

FIGURE 12 Effective clearing thresholds for 10–126 μm MBBA sample in the ultrasonic frequency range. 1: 3.2 MHz; 2: 400 kHz; 3: 1 MHz.

$b \simeq 100$ μm and $V_r|_{r=R-b} \simeq V_0$.† The corresponding values for J_s^{th} and J_s^{max} are very nearly those calculated in the preceding case for a bounded acoustic beam incident on an infinite layer.

The optical effect in a cell with fixed edges (one of the plates is made of lavsan film) was observed in Ref. 29. The results obtained agree with the theory. The values of the effective clearing threshold for 10, 40 and 90 μm MBBA samples at frequency 3.2 MHz are shown in Figure 12 (item 1). It can be seen that $J_s^{th} \sim d^{-2.5}$, which follows from (15). Experimental results for 21, 42, 81, and 126 μm MBBA samples at frequencies 400 kHz and 1 MHz[30,31] also confirm relation (15) (see Figure 12; items 2 and 3 for 400 kHz and 1 MHz, respectively). Distortion of the clearing pattern can be attributed to the inhomogeneous transducer field (Figure 2).

(b) The wave vector **k** makes the angle β with **n**. This case is more difficult to analyze, for it admits (simultaneously) several mechanisms of the layer structure destabilization. At the same time, this case is more interest-

†In calculation we used the following data: $E_p = 10^{11}$ kg m^{-1} s^{-2}; $\nu_p = 0.3$; $\rho_p = 2.5 \cdot 10^3$ kg m^{-3}.

ing, since it reveals qualitative peculiarities of the optical behaviour of nematics as compared to the case of normal incidence.

As in case (a), we start by considering the mechanisms responsible for the destabilizing torque.

Dion *et al.*[16,17,32-35] suggested that the molecular axes are tilted as a result of sound attenuation anisotropy $\Delta\alpha = \alpha_{\parallel} - \alpha_{\perp}$, where $\alpha_{\parallel}$ and $\alpha_{\perp}$ are the attenuation coefficients along **n** and in the transverse direction. Indeed, the energy density $E_s = J_s/c$ in a plane acoustic wave propagating in a nematic can be written in the form $E_s = J_s^0/c \exp[-2(\alpha_{\parallel} - \Delta\alpha \sin^2\beta)z]$,† where J_s^0 is the intensity at point with coordinate $z = 0$. This expression shows that the energy density depends on sample orientation relative to the wave propagation direction. Since a system always tends to be in a state with minimal potential energy, the molecules tilt so as to make attenuation of acoustic waves as low as possible. This mean that the molecular axes should be perpendicular to **k**. Energy dissipation due to sound absorption in the layer produces the torque

$$M_r = \frac{\Delta\alpha}{\rho c^2} d p_s^2 \sin 2\beta, \tag{16}$$

where p_s is the alternating sound pressure. Equating the elastic moment and torque, we find

$$\varphi_2(x, z) \simeq \frac{\Delta\alpha d^3}{cK_3} J_s, \tag{17}$$

which gives, by virtue of Eq. (1), the layer transmissivity. It was shown that for a constant layer thickness $I/I_0 \sim J_s^4$; but for $J_s = \text{const}$, $I/I_0 \sim d^{10}$. Figure 13 (curves 1–3) shows how the director orientation varies within the layer. The distributions were calculated for a 250 μm MBBA sample at 3.5 MHz and $\beta_1 = -36°$ for acoustic intensities 39, 163, and 940 W/m^2. At the middle of the layer the theoretical values of maximal director tilt are proportional to J_s, in accordance with (17). The profile of the director tilt distortion, as constructed for a sample located in the acoustic transducer radiation zone, is shown in Figure 14. It can be seen that the central bright region is surrounded by circular dark and bright fringes, the dark fringes corresponding to intensity minima in the Fraunhofer zone.

Experiments with crystals of positive and negative dielectric anisotropy (layer thickness = 122–250 μm) performed to determine incidence angles corresponding to minimal internal reflection in a cell yielded results which agree qualitatively with the theory.[16,17,32,34] As an example, Figure 15 shows experimental curves (1–3) of the relative light intensity incident on a layer

†As is shown in Refs. 36–38, in nematics the attenuation coefficient α depends on the angle β as $\alpha = a + b\sin^2\beta + c\sin^2 2\beta$ where a, b, and c are coefficients dependent on the medium viscosity coefficients. Generally, $b \gg c$, so that $\alpha = a + b\sin^2\beta = \alpha_{11} - \Delta\alpha \sin^2\beta$.

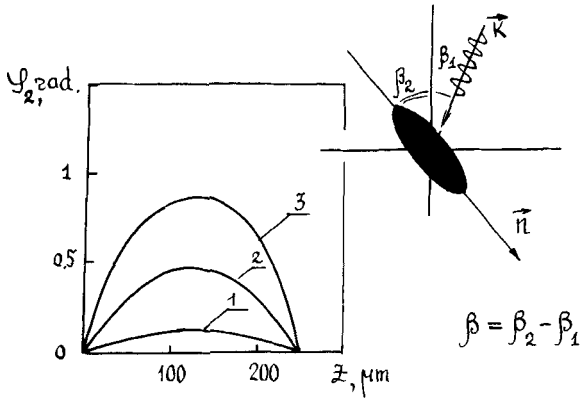

FIGURE 13 Theoretical distribution of the director tilt across the layer thickness for acoustic intensities 1: 39, 2: 163, and 3: 940 W/m^2; MBBA; $d = 250$ μm; $f = 3.5$ MHz; $\beta_1 = -36°$.

at 0, 4, and 6° as a function of the transducer voltage, and also the calculational results for normal incidence (curve 1). To fit the experimental data to the calculational results, one of the experimental values was set equal to the corresponding calculated value (here $d = 250$ μm, $f = 3.5$ MHz, $\beta_1 = -45°$ and $-36°$ for experiment and calculation, respectively). As for quantitative agreement, we should point out that the calculations of Dion and Jacob were based on the wrong assumption that sound is absorbed at a distance smaller than the layer thickness. Rigorous calculation shows that the effect can be observed at intensities 10^3 W/m^2,[39] while in the Dion experiments the values of J_s^{th} and J_s^{max} are equal to 10 W/m^2 and 25 W/m^2, respectively. For such J_s values the clearing effect caused by the absorption anisotropy is masked by more pronounced effects, which are discussed below.

Reference 40 considers the role of the flow mechanism suggested by Nagai, Peters, and Candau for normal incidence of a bounded acoustic beam on a layer of finite extension. In the case of oblique incidence, the effective "acoustic force" F inducing the flow is of the form

$$\mathbf{F} = \begin{cases} F\cos\beta_1; \quad 0; \quad F\sin\beta_1 & \text{for } |x| < \mathscr{D}/2 \\ 0 & \text{for } |x| > \mathscr{D}/2. \end{cases} \tag{18}$$

In this case the acoustic flow in the insonified region and around it has a more complicated structure. To simplify the hydrodynamic problem, only that part of the layer is usually considered which lies far away from the region occupied by the acoustic beam. It is usually assumed that in this part the acoustic flow (generated by the x-component of the effective force) is

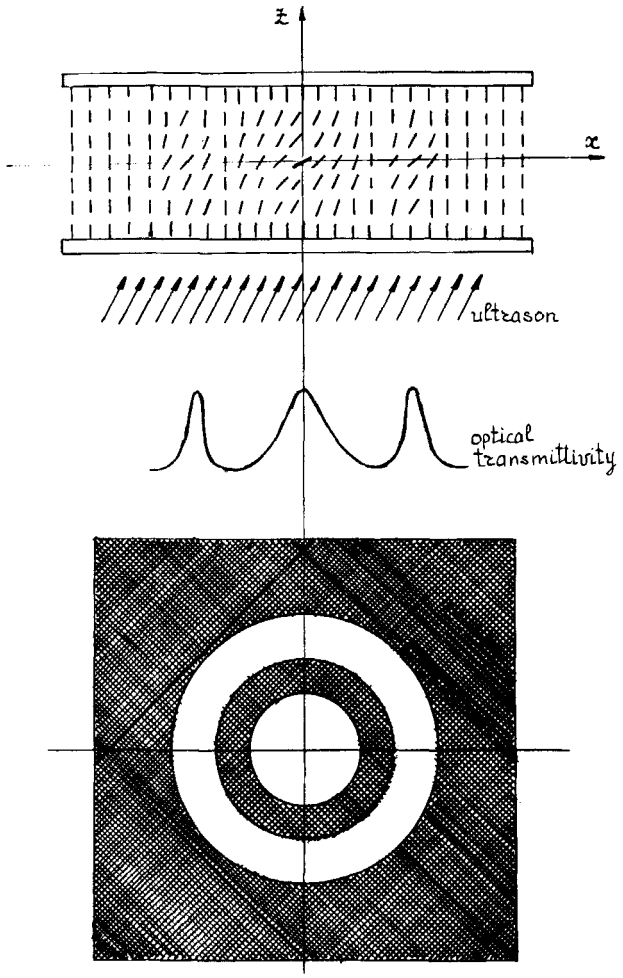

FIGURE 14 The Dion model for the mechanism of director reorientation in an acoustic field (oblique incidence of sound).

two-dimensional and closes up outside the irradiated region. The corresponding pattern of streamlines and velocity isolines is shown in Figure 5b. If the flow velocity $V^{(2)}$ obeys Poiseuille' distribution along the z-axis, the director tilt under the torque $\alpha_2(\partial V^{(2)}/\partial z)$ is given by

$$\varphi_2(r, z) = \frac{\alpha_2 d^2 \alpha J_s}{3\eta r^2 K_3} Z \left[\frac{z^2}{(d/2)^2} - 1 \right]. \tag{19}$$

The optical transmissivity is related to J_s and d by

$$\frac{I}{I_0} \sim \frac{\alpha^4 J_s^4 d}{\eta^4} \tag{20}$$

and the clearing pattern represents dark rings corresponding to velocity isolines; the radii of the rings satisfy the condition

$$\gamma r_\gamma^4 = \text{const.} \tag{21}$$

Here r_γ is the radius of the γth ring, which is related to the acoustic intensity and layer thickness by

$$\frac{J_s}{r_\gamma^2} = \text{const,} \tag{22}$$

$$\frac{J_s^2 d^7}{r_\gamma^2} = \text{const.} \tag{23}$$

Elegant Candau's experiments[40] with an annular cell have shown that the local action of the acoustic beam on a layer gives rise to a transverse acoustic flow at a large distance from the insonified region, so that layer clearing is observed within the entire ring. (To eliminate accidental insonifi-

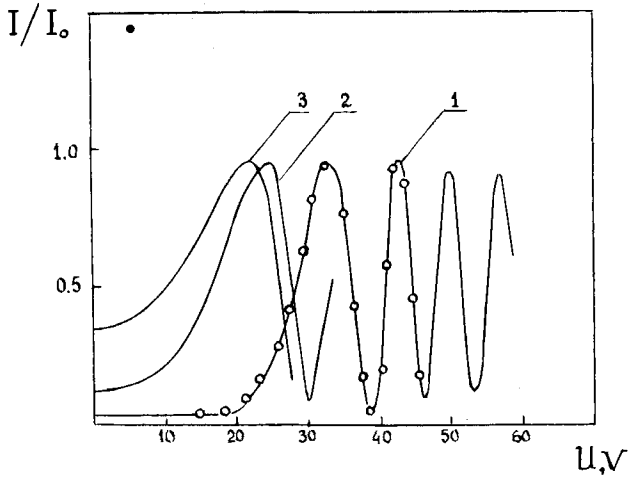

FIGURE 15 Optical transmittance of monochromatic light passing through the layer at 0, 4, and 6° vs. the transducer voltage; MBBA; $d = 250$ μm; $f = 3.5$ MHz.

cation of the whole ring, only its lower part was inserted in the immersion liquid).

It was found in these experiments that $I/I_0 \sim J_s^{3.3}$, which differs slightly from the theoretical dependence (see Eq. (20)), and the angular distribution of I/I_0 reveals a sharp maximum near $\beta_1 = 41°$ correlating with the maximum of the cell acoustic transmission. These data refer to a 200 μm PCB sample ($f = 2.82$ MHz).

Experiments with cylindrical cells[40] irradiated in the central region with a focused acoustic beam have shown that the clearing pattern depends on the relationship between the acoustic wavelength and the layer thickness. In thick samples ($d > \lambda/2$) the streamline and clearing patterns are similar to those predicted by the two-dimensional flow model, and the ring radius r_γ satisfy conditions (21) and (22).† Comparison of r_γ values for layers of different thickness, observed under maximal acoustic transmission, shows that relation (22) is also valid. For example, in 200 μm and 500 μm PCB samples the ratio $J_s^4 d^7/r_1$ amounts to $1.35 \cdot 10^{-9}$ and $1.52 \cdot 10^{-9}$ W^4 cm^3, respectively. For $d < \lambda/2$, the flow structure becomes more complicated, and the optical effect cannot be interpreted within the framework of the model considered.

As is shown in Ref. 41, only by introducing boundary forces in the insonified region can one describe quantitatively the optical effect under oblique incidence of sound. Indeed, since a liquid crystal and bounding plates have different acoustic properties, an oblique acoustic wave produces, besides longitudinal waves, two viscous waves propagating deep into the layer perpendicular to the layer surfaces. The boundary forces, proportional to the time-averaged product of particle velocities in the longitudinal and viscous waves, give rise to a steady-state flow along the Ox axis (Figure 16).

Consider a more general case where an acoustic wave is incident on a layer placed between hard plates of thickness H_1 and H_2. The vibration velocities of the layer boundaries can be written in the form

$$V_x|_{z=0} = V_x|_{r=d} = V_{Ox} e^{-i(\omega t - k \sin \beta_1 x)},$$
$$V_z|_{z=0} = V_z|_{r=d} = V_{Oz} e^{-i(\omega t - k \sin \beta_1 x)} \qquad (24)$$

(β_1 is the incidence angle). Solving the wave equation for the motion of the liquid in the layer with boundary conditions (24), we obtain the equation for

†Experimental values obtained for r_γ show that the exponent differs slightly from the theoretical one and takes the values from 3.2 to 3.9, depending on the ratio d/λ and incidence angle.

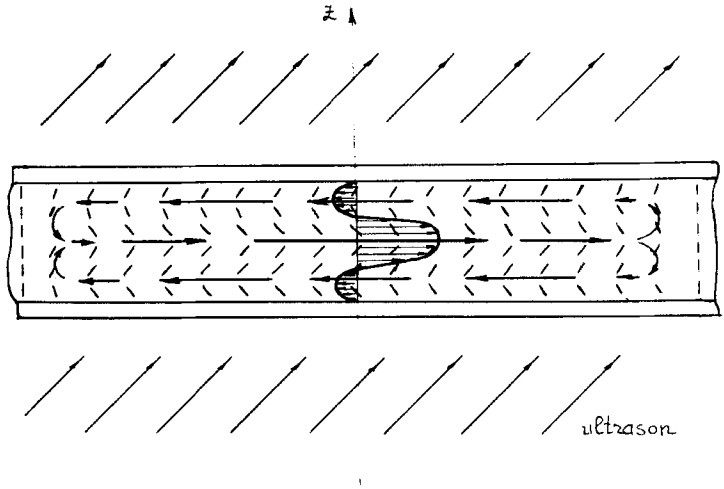

FIGURE 16 The Kozhevnikov model for the mechanism of director reorientation in an acoustic field (oblique incidence of sound).

the steady-state flow velocity $V^{(2)}$

$$\eta_2 \frac{d^3 V_x^{(2)}}{dz^3} = \rho \frac{d^2}{dz^2} \langle V_x V_z \rangle + (*)$$

$$V_z^{(2)} = 0. \tag{25}$$

Here $(*)$ stands for the terms $\alpha(d^2/dz^2)\langle \varphi \nabla V \rangle$ and $\alpha(d^2/dz^2)\langle V \nabla \varphi \rangle$ which contribute little to the solution, and $\langle\ \rangle$ denotes time-averaging. The destabilizing moment $M_h \cong \alpha_2 (dV_x^{(2)}/dz)$ makes the director tilt through the angle

$$\varphi_2 = \frac{\rho V_0^2 \alpha_2 d}{2 q_{\text{vis}} \eta_2 K_3} \left[Q \frac{z}{d} + (Q - 2S) \left(\frac{z}{d} \right)^2 + (Q - 2S) \left(\frac{z}{d} \right)^3 \right], \tag{26}$$

where Q and S depend on the angle β_1, the frequency and amplitude of vibrations, and also on the cell parameters (the expressions for Q and S are omitted, for they are too bulky). The optical transmissivity in this case is given by

$$\frac{I}{I_0} = \sin^2 \left\{ \frac{\Delta n k_0 d}{32} \left(\frac{\rho V_0^2 d_2 d}{K_3 q_{\text{vis}} \eta_2} \right)^2 A_1 \right\} \sin^2 \theta_0, \tag{27}$$

where

$$A_1 = \frac{1}{105}Q^2 + \frac{1}{70}QS + \frac{1}{105}S^2.$$

Let us make some estimates for a cell in water. Figures 17a and b show the parameter A_1 and acoustic transmittance of the cell D_1 as a function of the angle β_1, as calculated for 10, 30, and 100 μm MBBA samples (curves 1–3) at 1 MHz for the following cell parameters: $H_1 = 0.02$ cm; $H_2 = 0.3$ cm; $E_p = 0.425 \cdot 10^{12}$ g cm^{-2}; $\mu_p = 0.225 \cdot 10^{12}$ g cm^{-1} sec^{-2}. It can be seen that A_1 and, therefore, the optical transmissivity are maximal for maximal acoustic transmittance, which is confirmed experimentally.[3,19,42,43]

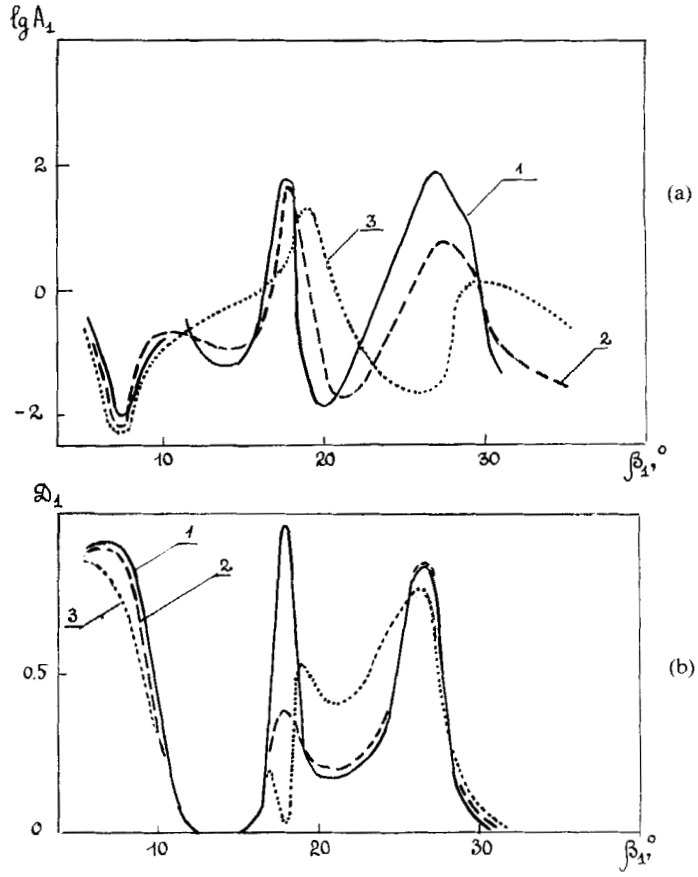

FIGURE 17 The parameter A_1 (a) and the acoustic transmission coefficient D_1 (b) as a function of incidence angle for MBBA samples. 1: 10 μm; 2: 30 μm; 3: 100 μm.

A slight shift of peak A_1 values along the abscissa axis for different layer thickness d means that the angles of maximal clearing are determined by the bounding plate parameters. For example, when H_1 and H_2 were much larger than the acoustic wavelength, high optical signal was observed only in a narrow incidence interval.[44] At 2.64 MHz for $H_1 \simeq H_2 = 1$ mm and $d = 100$ μm this interval was 27–30°. For thin plates ($H_1 \simeq H_2 = 100$ μm, $d = 50$ μm) the angular dependence of the cell optical transmissivity revealed a broad maximum between 20° and 30°.

Relation (27) implies that the effective clearing threshold for a 100 μm sample at 1 MHz is 1 W/m^2 and 0.1 W/m^2 for A_1 equal to 1 and 100, respectively. The latter case corresponds to one of the acoustic transmittance maxima ($\beta_1 \cong 17°$). The relationship between J_s and d depends on β_1: for the first maximum of optical transmissivity $J_s^{\text{th}} \sim d^{-1.25}$ and for the second maximum, $J_s^{\text{th}} \sim d^{-0.7}$. This correlates with the results of Hareng *et al.*[42] who showed that for ZLI-518 and PCB samples with thickness 30–500 μm $J_s^{\text{th}} \sim d^{-1}$ in the frequency range 0.9–3.6 MHz.[43] However, the experimental value of J_s^{th} exceeds the theoretical one. For instance, experiments performed at MHz with a 100 μm PCB sample give the value 30–40 W/m^2 at the centre of the irradiated region. This discrepancy may be due to the fact that calculation has been made for an acoustic wave, while Hareng experimented with a bounded acoustic beam. In this case the boundary forces in the irradiated region give rise to flows closed up outside the beam.

Consider the optical effect caused by these flows in the outer region of the layer, i.e. for $(r - R) > d$ (Figure 18).

The jump of the pressure radial derivative at the boundary of the insonified region can be written as

$$\left.\frac{\partial P_s^{(2)}}{\partial r}\right|_{r=R+0} - \left.\frac{\partial P_s^{(2)}}{\partial r}\right|_{r=R-0} = -\rho \left(\frac{\partial}{\partial x}\langle V_{s_x}^2 \rangle + \frac{\partial}{\partial z}\langle V_{s_x} V_{s_z} \rangle \right)\Bigg|_{r=R} \cos\chi, \tag{28}$$

where χ is the angle between the radius r and the Ox axis, V_s $(V_{s_x}, 0, V_{s_z})$ is the particle velocity in the irradiated region. Averaging this expression over time and taking into account sound absorption in the crystal, we obtain the following relationship between the outer and inner pressure gradients

$$\left.\frac{\partial P_s^{(2)}}{\partial r}\right|_{r=R+0} - \left.\frac{\partial P_s^{(2)}}{\partial r}\right|_{r=R-0} = (F_1 + F_2)\cos\chi, \tag{29}$$

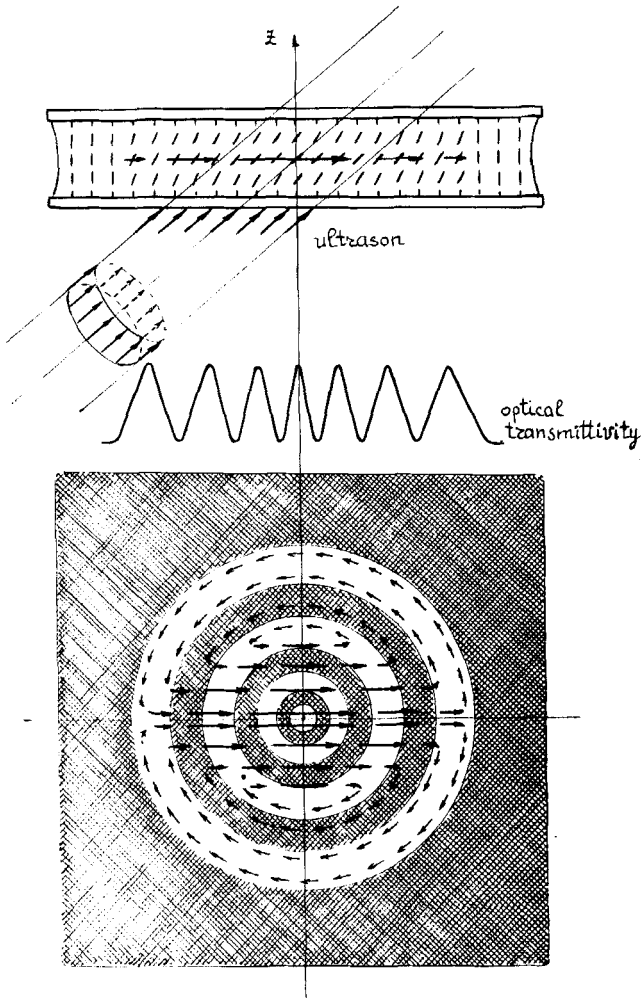

FIGURE 18 The Kozhevnikov model for the mechanism of director reorientation in an acoustic field (oblique incidence of a bounded acoustic beam of radius R).

where F_1 is the x-component of the effective acoustic force due to sound absorption, $F_1 = \rho V_s^2 \alpha \mathscr{D}_1 \sin \beta_1$, and F_2 is the term due to the boundary forces. The velocity components of the flow in the outer zone caused by these forces are of the form

$$V_{s_x}^{(2)} = \frac{(F_1 + F_2)R^2}{\eta_2} \cdot \frac{\cos 2\chi}{4r^2} z(d - z)$$

and

$$V_{s_y}^{(2)} = \frac{(F_1 + F_2)R^2}{\eta_2} \frac{\sin 2\chi}{4r^2} z(d - z). \tag{30}$$

Equating the elastic and destabilizing moments, we easily find the director tilt in the flow[41]

$$\varphi_2(z) = \frac{(F_1 + F_2)R^2\alpha_2(3z^2 - 2z^3 - z)}{24\eta_2 K_3 r^2}, \tag{31}$$

and then, by virtue of (1), we find the layer optical transmissivity

$$\frac{I}{I_0} \simeq \frac{\Delta n k_0 \alpha_2^2}{2.4 \cdot 10^5 \eta_2^2 K_3^2} \cdot \frac{(F_1 + F_2)^2 d^7 R^4}{r^4}. \tag{32}$$

This expression shows that outside the irradiated region the clearing pattern represents a system of alternating bright and dark rings of radii $r_\gamma = \pi/2\gamma$ ($\gamma = 1, 2, 3$) with a dark cross (in crossed polarizers). As was already noted, precisely this pattern was observed by Candau *et al.*[40] in a cell irradiated with a focused acoustic beam and by Hareng *et al.*[3,42,43] for a flat bounded beam of higher intensity.

To compare theoretical predictions with experimental results, we estimate the ratio of the radius of the first dark ring r_1 to the irradiated region radius R. From expression (32) we have

$$\frac{r_1}{R} = \left\{ \frac{\Delta n k_0 d^7 \alpha_2^2 (F_1 + F_2)^2}{2.4 \cdot 10^5 \pi \eta_1^2 K_3^2} \right\}^{1/4}. \tag{33}$$

For a 200 μm PCB layer at frequency 2.8 MHz and acoustic intensity $J_s = 40$ mW/cm^2 the ratio $r_1/R = 3$–5 for β_1 corresponding to maximal acoustic transmittance of the cell ($D_1 \simeq 1$); calculation by Eq. (33) gives the value 4.5.

Let us now assess which factor is more significant: the boundary force (F_2) or the effective acoustic force (F_1). For a maximal acoustic transmittance of the cell, the boundary force can be estimated as $|F_2| \simeq \rho V_0^2/2d$. For $\beta_1 \simeq 25°$ and $J_s = 40$ mW/cm^2 we obtain $F_2 = 128$ g cm^{-2} sec^{-2}. Setting $\alpha_2 = \eta_2$ and $\alpha = 0.1$ cm^{-1} we find $F_1 = 0.13$ g cm^{-2} sec^{-2}. Thus, the optical effect is determined by boundary forces in the irradiated region. Although the effective acoustic force F_1 considered by Candau *et al.*[40] leads

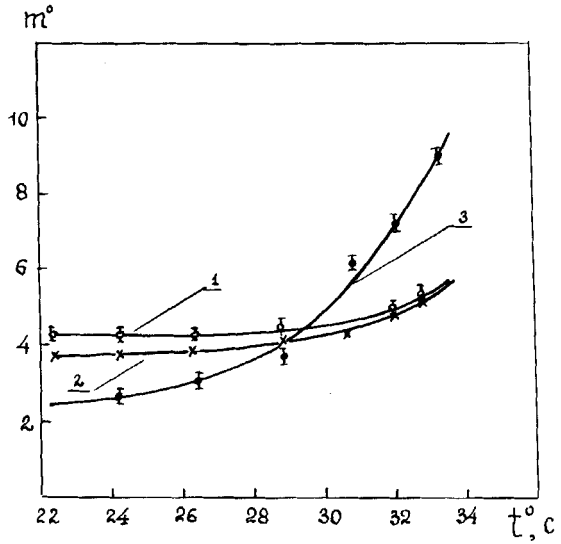

FIGURE 19 Temperature dependence of the acoustic intensity exponent m^0: 1) outer ring; 2) central region; 3) averaged over the whole cell; $d = 100$ μm; $f = 2.4$ MHz; PCB.

to the pattern which qualitatively agrees with experiment, it cannot explain the effect quantitatively. Indeed, for the acoustic force estimated above the ratio $r_1/R = 0.14 < 1$ is devoid of physical meaning.

The above models for the physical mechanisms responsible for the destabilizing torque under compression of a nematic show that the theoretical optical transmissivity is, as a rule, proportional to J_s^4. It should be noted however that the true relationship between these quantities is more complicated: it depends on the acoustic field spatial inhomogeneity, temperature, layer thickness, and type of nematic crystal. For instance, when a cell is immersed in water and measurements are performed within the Fraunhofer zone, the exponent m^0 in J_s may depend on the experimental procedure.[45] Figure 19 shows the temperature dependence of this exponent in the nematic range for a 100 μm PCB at 2.4 MHz (curves 1–3). These curves refer to the optical transmissivity measured within the outer ring, in the central region, and for the entire cell area.† In the first two cases $m^0 \simeq 4$ and varies little with increasing temperature. For the averaged optical signal (curve 3) the exponent $m^0 \simeq 2$ for low temperatures, but grows rapidly as

†We have already pointed out that in the Fraunhofer zone ($z > \mathscr{D}^2/4\lambda$) the optical pattern of "perturbation" in a cell immersed in water consists of a central spot and the outer ring whose median diameter increases linearly with the distance from the transducer.

the temperature approaches the phase transition point. Quadratic dependence of the averaged optical signal on the acoustic intensity was often observed on MBBA and PCB sample for layer thicknesses 70 μm and 100 μm in the frequency range 0.9–6 MHz.[19,46]

The clearing pattern of nematics considered above may sometimes be modified as a result of secondary effects. For example, if the thickness of the bounding plates is much smaller than the acoustic wavelength, the clearing pattern represents a system of bright and dark fringes. The effect is caused by the transformation of longitudinal waves into surface and waveguide modes whose interaction gives rise to Rayleigh flows and periodic director distribution in the layer.[2]

The joint action of several mechanisms responsible for steady-state distortion of the layer structure as well as the "long-range" character of some of these mechanisms reduce the cell resolving power. To correct distortions caused by acoustic flows penetrating into the non-irradiated area of the layer, the cell may be divided into separate regions by thin strips or a grid deposited onto the glass substrate by photoetching techniques[19,43,44,46]; the period of such a matrix must not exceed the acoustic wavelength.[47]

Low frequencies. Thus far, we have considered optical effects caused by a steady-state distortion of the structure of a homeotropic nematic crystal. For audible frequency range, where $\lambda_{vis} \ll d$, periodic compression does not only produce quasi-stationary director tilt typical of high frequencies, but also periodic director oscillation, which gives rise to an alternating component of the light flux passing through the layer and analyser.

In early experiments modulation of the light passing through a cell was observed in the frequency range from several kHz to several tens kHz.[6,10,48–50] More recent investigations have shown that in a cell with free edges and with pulsed operation of the acoustic transducer the effect can be observed at frequencies up to 10^5 Hz.[51] It was found however that the effective threshold decreases by approximately an order of magnitude as the repetition rate rises from 10 Hz to 2 kHz and then remains practically constant up to 200 kHz (Figure 20). This can be attributed to the fact that as long as the pulse repetition period T exceeds the characteristic relaxation time τ of a nematic under deformation, the molecular ensemble in the layer has enough time to relax, so that the initial orientation of the molecules sets in before the next pulse. This is not the case however if T is of the order of or less than τ. The data were obtained on a 50 μm CBOOA sample with square pulses whose duration varied from 10 ms to 20 ms as the repetition rate grew. It can be seen from Figure 20 that $\tau \simeq 10^{-3}$ s.

We now discuss in greater detail, the optical effects in a nematic at audible frequencies for a cell with *fixed edges* (acoustically rigid boundary). We shall assume that the cell is axisymmetric and the layer dimensions

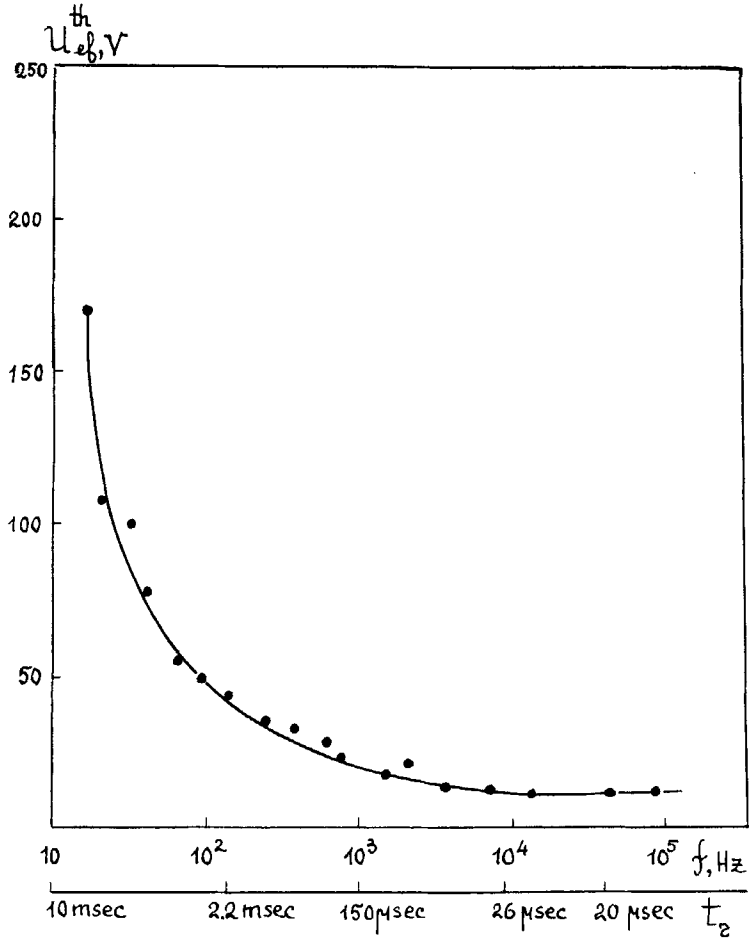

FIGURE 20 Effective clearing threshold for a 50 μm CBOOA sample (the nematic phase) in a free-edge cell (pulsed operation).

satisfy the following conditions:

$$\lambda \gg R, \qquad d/2 \ll \lambda_{vis} \ll R. \tag{34}$$

Suppose the layer is placed between a thick non-deformable plate H_1 and a thin flexible plate H_2. Pressure in the acoustic wave $P_s = P_{s_0} e^{-i\omega t}$ makes the thin plate buckle in the central region, thereby compressing the liquid in this region. The pressure gradient results in periodic displacement of the liquid (along the layer plane) to the edges and in the reverse direction. Inhomoge-

neous distribution of the radial velocity over the layer thickness causes the director to tilt through the angle

$$\varphi_2 = \frac{\partial U_r}{\partial z}, \tag{35}$$

where U_r is the radial particle displacement. If the radial and normal displacement components vanish at the layer edges and on non-deformable surface, but on the flexible surface the normal component does not vanish and coincides with the plate flexure, we can demonstrate, following Ref. 52, that

$$U_r = \frac{36P_{s_0}R}{\rho c^2\left(1 + \dfrac{36dA}{\rho c^2 R^4}\right)} \cdot \frac{z(d-z)}{d^2} F(r,t), \tag{36}$$

where

$$F(r,t) = \sum_{m=1}^{\infty} a_m \left[1 + \left(\frac{12\omega\eta}{P_m^6 A d^3}\right)^2\right]^{-1/2} J_1(p_m r)\cos(\omega t - \gamma_m),$$

$$a_m = \frac{2J_3(P_m R) - J_5(P_m R)}{(P_m R)^2 J_0^2(P_m R)};$$

$J_n(x)$ is the Bessel function of the first kind of order n; P_m are the roots of the equation $J_1(P_m R) = 0$; $\gamma_m = \text{tag}^{-1}(12\omega\eta/P_m^6 A d^3)$ is the retardation of the corresponding contributions of the Fourier components to displacement with respect to acoustic pressure; $A = E_p H_2^3/[12(1-\nu_p^2)]$.

For a cell with typical parameters $H_2 = 0.1$ cm, $d = 10^2$ μm, $R = 1$ cm in the frequency range $1\ s^{-1} \ll \omega \ll 2 \cdot 10^4\ s^{-1}$ where conditions (34) are satisfied, the function $F(r,t)$ can be represented in the form

$$F(r,t) = f(r)\cos\omega t, \tag{37}$$

where $f(r) = \sum_{m=1}^{\infty} a_m J_1(p_m r)$. Differentiation of U_r with respect to z yields

$$\varphi_2(r,z) = \frac{36P_{s_0}R}{\rho c^2\left(1 + \dfrac{36Ad}{\rho c^2 R^4}\right)} \cdot \frac{d-2z}{d^2} f(r)\cos\omega t. \tag{38}$$

In the general case of oblique incidence of light we obtain, using (38) and substituting in (1) $k_0/\cos\varphi_0$ for k_0,

$$\frac{I}{I_0} = \sin^2\left\{\frac{\Delta n k_0 d}{2}\cdot\frac{\sin^2\varphi_0}{\cos\varphi_0} + B\frac{\cos 2\varphi_0}{\cos\varphi_0}f(r)\cos^2\omega t\right\}\sin^2 2\theta_0, \quad (39)$$

where

$$B = 216\Delta n k_0\left(\frac{R}{d}\right)^2 k U_0^2\left(1 + \frac{36dA}{\rho c^2 R^4}\right)^{-2}.$$

U_{s_0} is the particle displacement amplitude in a nematic crystal due to acoustic pressure P_{s_0}, φ_0 is the incidence of light onto the layer relative to the normal.

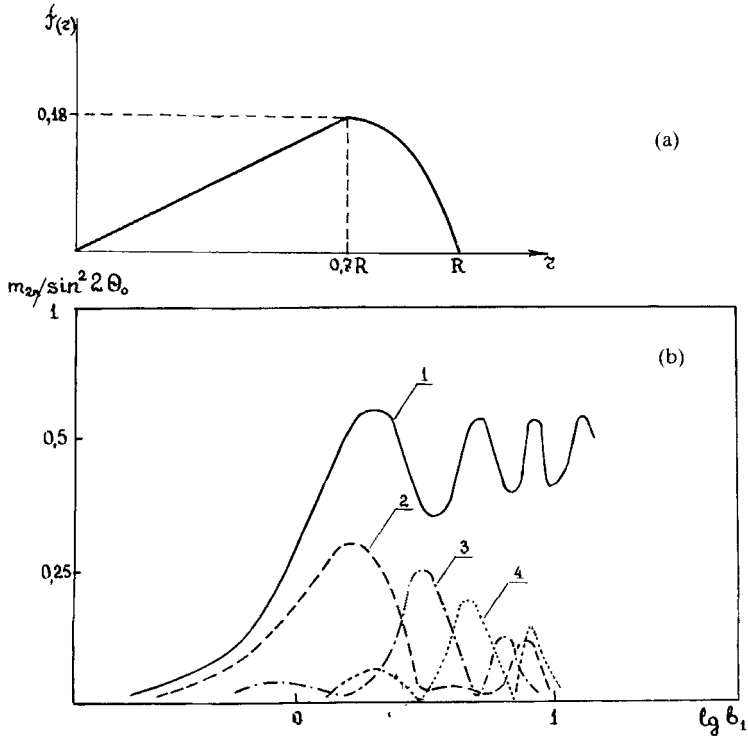

FIGURE 21 Displacement radial component distribution under nematic spreading in a fixed-edge cell (acoustically hard boundary) (a). The dc component and the moduli of the 2nd, 4th, and 6th harmonics for a fixed-edge cell at audible frequencies as a function of $b_1(V)$ (curves 1–4, respectively) (b).

Expression (39) implies that:

1) the optical effect depends on coordinate r. The form of this dependence is determined by the function $f(r)$ shown in Figure 21a: the ratio I/I_0 is maximal at $r = 0.7R$;

2) the intensity of the light passing through the layer and analyser has a direct component m_0 and an oscillating component m_{2n}—the sum of harmonics with frequencies multiple to the double acoustic frequency:

$$m_0 = \frac{1}{2}\left\{1 - \cos\left[\frac{\Delta n k_0 d \sin^2\varphi_0}{2\cos\varphi_0} + Bf^2(r)\frac{\cos 2\varphi_0}{\cos\varphi_0}\right] \times J_0\left[Bf^2(r)\frac{\cos 2\varphi_0}{\cos\varphi_0}\right]\right\}\sin^2 2\theta_0 \tag{40}$$

$$m_{2n} = -\frac{1}{2\pi}\int_0^{2\pi}\cos\left[\frac{\Delta n k_0 d}{2}\frac{\sin^2\varphi_0}{\cos\varphi_0} + Bf^2(r)\frac{\cos^2\varphi_0}{\cos\varphi_0} + Bf^2(r)\frac{\cos 2\varphi_0}{\cos\varphi_0}\cos x\right]\cos nx\,dx \cdot \sin^2 2\theta. \tag{41}$$

It follows from relations (40) and (41) that for low P_{s_0} values, which corresponds to $B \ll 1$, the dc component variation and the oscillating component are proportional to $P_{s_0}^2$, provided the phase difference between the ordinary and extraordinary rays in the absence of sound $(\Delta n k_0 d/2)(\sin^2\varphi_0/\cos\varphi_0)$ is not equal to πn, where n is an integer.

Using (40) and (41) and setting $\varphi_0 = 0$, we can easily describe the optical effect for normal incidence of light. In this case for $B \ll 1$ the dc and oscillating components are both proportional to $P_{s_0}^4$.

The dc component and the moduli of the second, fourth, and sixth harmonics as a function of the parameter $b_1 = Bf(r)$ are shown in Figure 21b (curves 1–4) (these curves are calculated by (40) and (41) for $\varphi_0 = 0$). It can be seen that the dc component reaches the first maximum at $b_1 = 2$ and oscillates about the value $m_0 = 0.5$ as b_1 increases. For low b_1 values ($b_1 \lesssim 2$) the second harmonic contributes mainly to the oscillating component. For $b_1 \simeq 4$ and $b_1 \simeq 6$, the fourth and sixth harmonics should be mainly observed. As b_1 increases further, the harmonics are superimposed.

We now estimate the effective clearing threshold for a cell with the aforementioned parameters at frequency 160 Hz for normal incidence and for $r = 0.7$ cm (the maximal effect). Estimates show that in this case the vibration amplitude is $U_{s_0}^{\text{th}} = 130$ μm and the displacement at the centre of

the plate is $\xi_0^{th} = 0.026$ μm.† The curve m_0 versus U_{s_0} exhibits the first maximum at $U_{s_0}^{max} = 580$ μm, the corresponding value of ξ_0^{max} being 0.12 μm.

Thus, these estimates clearly demonstrate that a cell with fixed edges and one flexible plate has a rather low sensitivity. If the non-deformable plate is replaced by a flexible membrane, the sensitivity can be enhanced approximately twice.

Other boundary conditions at the layer edges and the use of acoustically soft boundary (a cell with free edges) lead to no qualitative features in the optical behaviour of a nematic. This is confirmed by experiments.[53,54] Figure 22a shows the spectral composition of optical signal under such conditions as obtained for a 50 μm mixture of MBBA and EBBA at 86 Hz.[54]

In these experiments the nematic crystal layer was placed between two plates, one being stationary and the other vibrating at a given amplitude ξ_0 and frequency. The demodulated optical signals from the photomultiplier output were recorded by a tape recorder and then spectral-analysed by a digital processor. The analysis was performed in a constant band 2 Hz. The results of this analysis are shown by curves 1–5 in Figure 22a which correspond to components with frequencies f, $2f$, $4f$, $6f$, and $8f$; all the curves are normalized to the optical signal in the first maximum of the second harmonic.‡ It can be seen that the spectrum primarily contains even harmonics; first odd harmonics are observed only for large ξ_0 values and their contribution is rather small. For example, the maximum of the first harmonic occurs at $\xi_0 = 0.19$ μm and is ~ 7.5% of the maximal value of the second harmonic. Curves of Figure 22a have another interesting feature: the first maximum of each harmonic coincides with the first minimum of the preceding one. For instance, at $\xi_0 = 0.115$ μm the fourth harmonic is

†The flexure of a thin elastic plate (bounding a layer) in an acoustic field is given by the expression

$$\xi_{(z)} = \frac{3k\, dU_{S_0}}{1 + 36Ad/\rho c^2 R^4} \frac{(r^2 - R^2)^2}{R^4},$$

whence the maximal plate displacement in the central region is

$$\xi_0 = 3k\, dU_{S_0}\left(1 + \frac{36dA}{\rho c^2 R^4}\right)^{-1}.$$

‡At the initial moment the frequency of oscillating optical signal is twice the excitation frequency f.

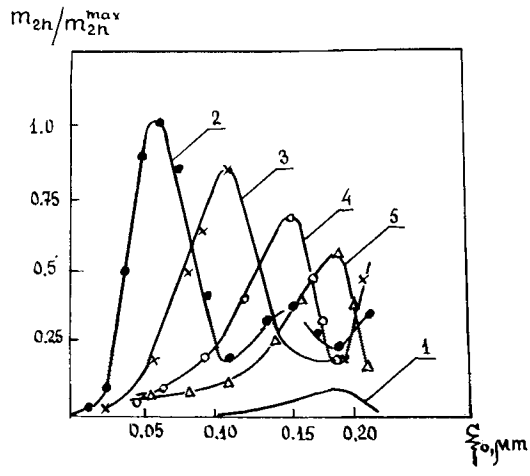

(a)

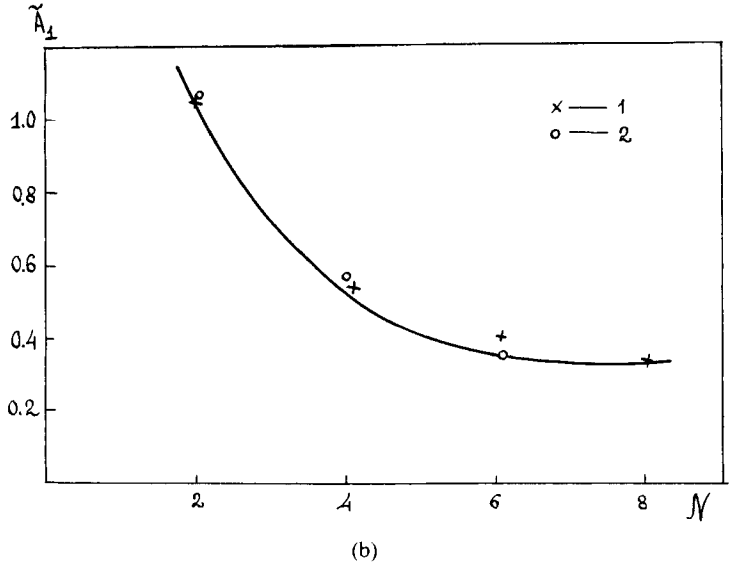

(b)

FIGURE 22 (a) Spectral composition of the optical signal in a free-edge cell; MBBA-EBBA mixture; $d = 50\ \mu m$; $f = 86$ Hz; curves 1 to 5 correspond to frequencies f, $2f$, $4f$, $6f$ and $8f$. (b) The ratio A_1 of displacements corresponding to the first maxima of the 2nd and Nth harmonics for different N. 1: from the experimental curves of Figure 21b; 2: calculated from the theoretical curves of Figure 21b.

maximal and the second one is minimal, etc., that is as the vibration amplitude increases, the energy is transferred from one harmonic to another to result in higher even harmonics in the optical signal spectrum. Reference 14 reports harmonics at frequency as high as $16f$.

These data on the behaviour of the oscillating component of optical signal in a cell with free edges agree qualitatively with theoretical results for a cell with fixed edges. As the theory predicts, for small ξ_0 the oscillating component is mainly represented by the second harmonic (see Figure 21b). At frequency 86 Hz for a 50 μm sample in a free-edge cell the first maximum of the second harmonic is observed at $\xi_0 \sim 0.06$ μm, which agrees within an order of magnitude with a theoretical estimate. Figure 22b shows the ratio $\tilde{A}_1$ of displacements corresponding to the first maxima of the second and Nth harmonics as a function of harmonic number N calculated by theoretical curves 2–4 of Figure 21b (2nd, 4th, and 6th harmonics) for a fixed-edge cell. Crosses are the values of $\tilde{A}_1$ determined from experimental curves of Figure 21b for a free-edge cell.

The experimental dependence of the optical signal on deformation in a free-edge cell also agrees with theoretical results for a fixed-edge cell. Figure 23a shows the data of Bertolotti *et al.* for a 50 μm CBOOA sample in the case of oblique incidence.† [51] Curves 1–4 correspond to the following pulse repetition periods T: 10^{-3}, $1.4 \cdot 10^{-3}$, $1.4 \cdot 10^{-2}$, and $5 \cdot 10^{-2}$ s with pulse duration t equal to 150 μs, 70 μs, 2.2 ms, and 10 ms, respectively. As can be seen from the figure, $J \sim U^2 t/T$, which also follows from relation (41). The case of normal incidence is shown in Figure 23b by the data of G. Yakovenko. Curves 1–3 correspond to a 50 μm MBBA sample at frequencies 885, 430 and 43 Hz. Under these conditions $J \sim \xi_0^n$ with $n \simeq 4.2$, which is close to $n = 4$ predicted by the theory for a fixed-edge cell.

Medium frequencies. By this term we mean the frequency range where the viscous wavelength is commensurate with the layer thickness. This intermediate case is of little interest for studying the optical behavior of nematics under deformation, because it is very difficult to carry out "unambiguous" experiments in the frequency range where the mechanisms characteristic of both low and high frequencies are present simultaneously. Reference 55 should be noted nevertheless, where the intracavity measurement technique[56] made it possible to reduce the effective clearing threshold by about an order of magnitude. At frequencies 480 Hz, 15 kHz, and 60 kHz the values of ξ_0^{th} were 0.9, $5 \cdot 10^{-3}$, and $5 \cdot 10^{-4}$ μm, respectively. These data confirm once more the validity of the ideas[16–18] that the clearing threshold observed in

†In these experiments performed with configuration of Figure 1a the layer is periodically compressed due to longitudinal vibrations of an acoustic transducer driven by square pulses.

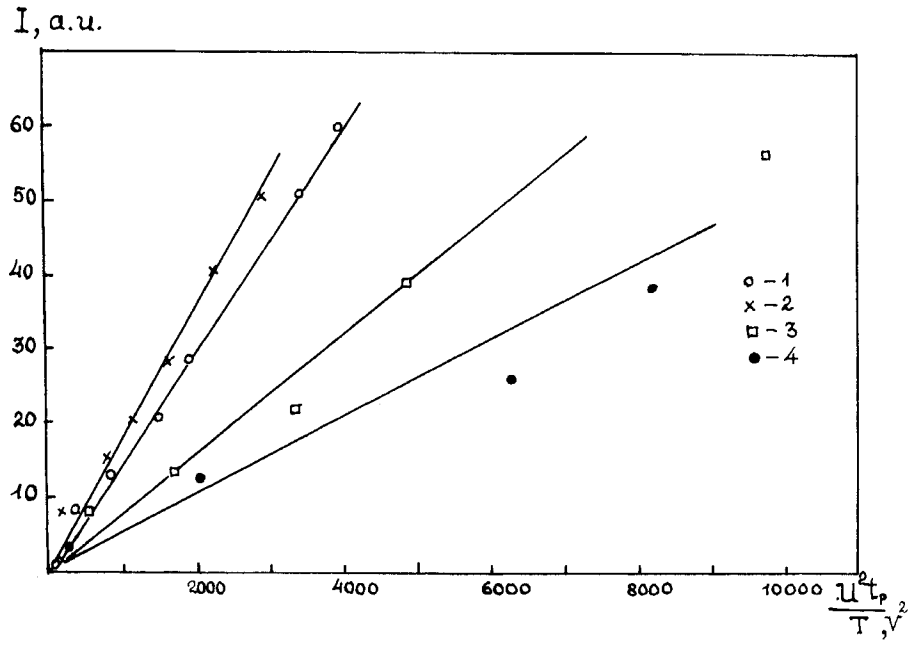

(a)

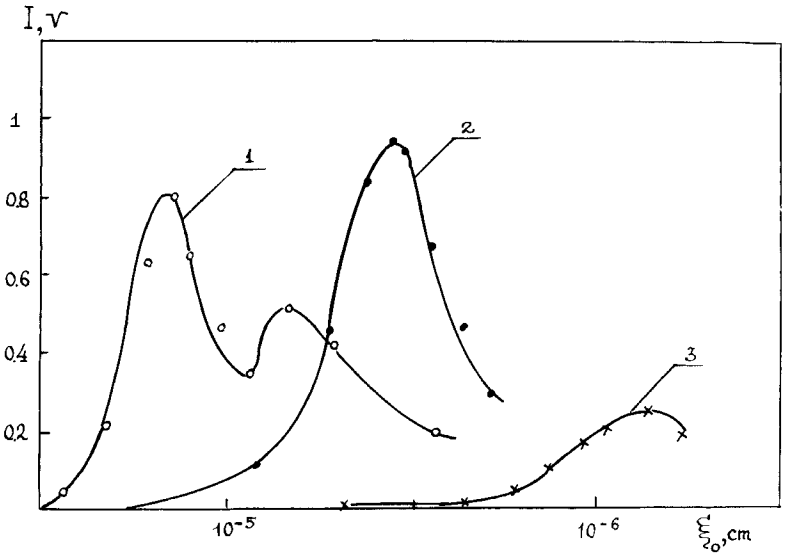

(b)

FIGURE 23 (a) The ac component of the optical signal vs. U^2t/T; pulsed operation; CBOOA (nematic phase); $d = 50$ μm; oblique incidence of light. curves 1 to 4 correspond to pulse repetition periods, T, of 10^{-3}, 1.4×10^{-3}, 1.4×10^{-2} and 5×10^{-2} s. (b) The ac component of the optical signal vs. the displacement amplitude at 885, 430 and 43 Hz (curves 1–3); $d = 50$ μm; normal incidence of light.

experiments with homogeneous layer deformation is determined by the sensitivity of the measuring instruments.

B. Shear deformation

An analysis of experimental data on the behaviour of nematics under shear deformation clearly shows that the presence of "parasitic" normal displacement components was completely ignored. At the same time, as is shown below, there are cases where even low ellipticity ($\sim 10^{-3}$) results in qualitative changes in the clearing pattern. Therefore, first we shall slightly complicate the problem and consider such a motion of the bounding plates when a fixed point of a bounding plate describes an ellipse in the vertical plane (elliptic deformation†). As before, we consider three frequency regions, depending on the relationship between the layer thickness and viscous wavelength.

Low frequencies. It is convenient to start precisely with this frequency range where the effect of ellipticity is especially pronounced. Suppose the motion of one of the bounding plates (as a result of external action) is described by

$$V_x|_{z=d} = V_0 \cos \omega t, \qquad V_z|_{z=d} = \beta V_0 \sin \omega t \tag{42}$$

and the amplitude of the longitudinal velocity component V_0 exceeds the amplitude of the transverse component βV_0.

Consider a cell with free edges and assume that the following conditions are satisfied: $K_3 d^2/\eta \ll \omega \ll \eta/\rho d^2$ and $\omega \ll c/L$. Compression of the layer due to transverse vibrations of the bounding plate makes the liquid flow towards the free edges with the following velocity profile:

$$V_x = \text{const}\, x(z^2 - zd)\sin \omega t. \tag{43}$$

The velocity V_z can be expressed in terms of V_x by virtue of the incompressibility condition, and the const can be found from (42). Taking into account $V_x = (V_0 z/d)\cos \omega t$ caused by the displacement of the upper plate in the horizontal plane, we can, following Refs. 4, 57, determine the velocity distribution in the layer. The equation for the small tilt of layer molecules φ is of the form

$$\gamma_1 \frac{\partial \varphi}{\partial t} - K_3 \Delta \varphi = -\alpha_2 \frac{\partial V_x}{\partial z} - \alpha_3 \frac{\partial V_z}{\partial x} - \gamma_1 (\mathbf{V} \nabla) \varphi - \gamma_2 \varphi \left(\frac{\partial V_x}{\partial x} - \frac{\partial V_z}{\partial z} \right). \tag{44}$$

†The papers by Guyon, Pieranski, and Dubois-Violette discuss such a type of elliptic deformation when the displacement ellipse lies in the layer plane. This case is analysed in Section I.2.

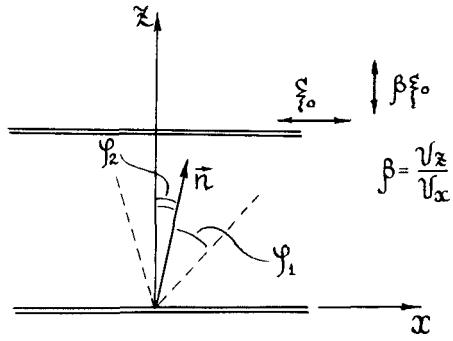

FIGURE 24 A model of director behaviour under elliptic deformation.

In the first approximation, its solution describes the director oscillations

$$\varphi_1 = -\frac{\alpha_2}{\gamma_1}\frac{\xi_0}{d}\sin\omega t + \frac{6\beta\alpha_2\xi_0}{\gamma_1\alpha}\cdot\frac{z(2z-d)}{d^2}\cos\omega t, \tag{45}$$

where $\xi_0 = V_0/\omega$. The second approximation gives the expression for the steady-state tilt of the molecules

$$\varphi_2 = \frac{\alpha_2(2\gamma_2-\gamma_1)}{4\gamma_1 K_3}\cdot\frac{\beta\omega\xi_0^2}{d^4}(z^4 - 2z^3d + zd^3). \tag{46}$$

This analysis leads to the director behaviour which is schematically shown in Figure 24. The ellipse is the trajectory of a fixed point of the vibrating plate; ξ_0 and $\beta\xi_0$ are the longitudinal and transverse components of this motion. Substitution of the total tilt angle $\varphi = \varphi_1 + \varphi_2$ into expression (1) yields†

$$m = \frac{I}{I_0} = \sin^2\left\{\frac{1}{2}[P_0 + P_1\sin\omega t - P_2\cos 2\omega t]\right\}\sin^2 2\theta_0, \tag{47}$$

†Elliptic deformation of a nematic produces flows described by the convective terms and antisymmetric part of the stress tensor. These flows lead to an additional tilt of molecules through the angle $\varphi_2' \simeq 10^{-2}\beta\rho\omega\, dL\,\varphi_2/\eta$. At audible frequencies, however, this effect is small as compared to those considered here.

where

$$P_0 = 0.21\Delta nk_0 d\left[\frac{\alpha^2(2\gamma_2 - \gamma_1)}{4\gamma_1 K_3}\beta\omega\xi_0^2\right]^2 + \Delta nk_0\left(\frac{\alpha_2}{\gamma_1}\right)^2\frac{\xi_0^2}{2d}\left[1 + 12\beta^2\left(\frac{x}{d}\right)^2\right];$$

$$P_1 = -\Delta nk_0\left(\frac{\alpha_2}{\gamma_1}\right)^2\frac{2\gamma_2 - \gamma_1}{10K_3}\beta\omega\xi_0^3;$$

$$P_2 = -\Delta nk_0\left(\frac{\alpha_2}{\gamma_1}\right)^2\frac{\xi_0^2}{2d}\left[1 - 12\beta^2\left(\frac{x}{d}\right)^2\right]. \tag{48}$$

It follows from (47) and (48) that optical transmissivity is generally determined both by linear and non-linear hydrodynamic effects.

For further analysis it is convenient to introduce the parameter $l = |2\gamma_2 - \gamma_1|/(6K_3)\beta\omega\xi_0 d$. For $l \ll 1$ the non-linear effects are weak, and the optical transmissivity can be written as

$$m = \sin^2\left[\tfrac{1}{2}P_2(1 + \cos 2\omega t)\right]\sin^2 2\theta_0. \tag{49}$$

The light passed through the layer and analyser has the dc component

$$m_0 = \tfrac{1}{2}\left[1 - \cos P_2 J_0(P_2)\right]\sin^2 2\theta_0 \tag{50}$$

and the oscillating component, which is the sum of even harmonics with frequencies multiple of 2ω:

$$m_{2n} = -\tfrac{1}{2}\cos P_2 J_{2n}(P_2)\sin^2 2\theta_0. \tag{51}$$

The transmissivity components m_0 and m_{2n} are determined by parameter P_2 only and do not depend on frequency. If we consider the effect in the central region of a layer, for small β values, then

$$P_2 = \Delta nk_0\left(\frac{\alpha_2}{\gamma_1}\right)^2\frac{\xi_0^2}{2d}. \tag{52}$$

In this case it follows from (50) that for $P_2 \ll 1$ the dc component is proportional to $(\xi_0^2/d)^2$; as P_2 grows, m_0 increases, reaching the first maximum $m_0^{\max} = 0.55$ at $P_2 = 1.97$; as P_2 grows further, m_0 oscillates about the value 0.5.

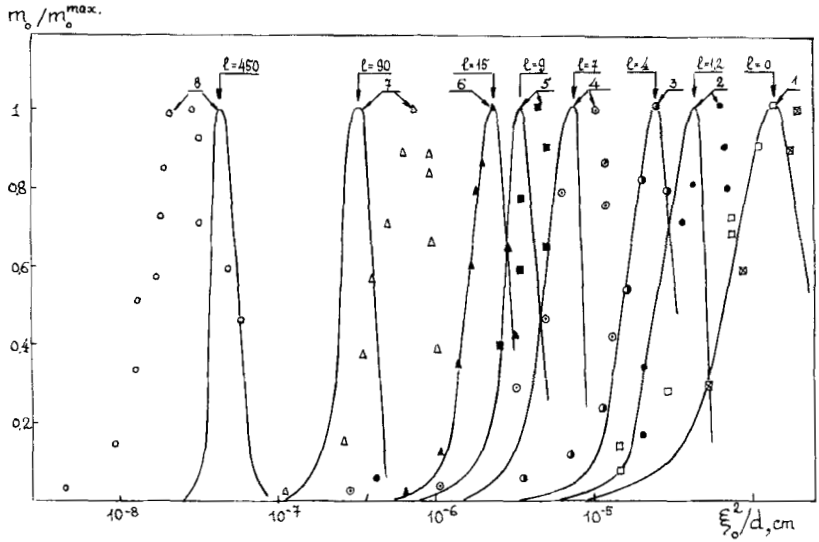

FIGURE 25 The behaviour of the dc component of the optical signal under elliptic deformation at audible frequencies. Parameters discussed in the text.

If $l \gg 1$, the non-linear effects become significant, and expression (47) takes the form

$$m = \sin^2\left[\tfrac{1}{2}P_0 + \tfrac{1}{2}P_1 \sin \omega t\right] \sin^2 2\theta_0. \tag{53}$$

The dc component and harmonics are given in this case by

$$m_0 = \tfrac{1}{2}\left[1 - \cos P_0 J_0(P_1)\right] \sin^2 2\theta_0, \tag{54}$$

$$m_n = -\tfrac{1}{2}\cos P_0 J_n(P_1) \sin^2 2\theta_0, \qquad n = 1, 2, 3, \ldots. \tag{55}$$

The above consideration clearly shows physical peculiarities of the behaviour of nematics under elliptic deformation; theoretical estimates agree with experiment. Figure 25 presents the data for the dc component. All the values of m_0 are normalized to m_0^{max} corresponding to the first maximum of clearing, and ξ_0 appears as ξ_0^2/d.† Curves 2–8 are calculated by relation (54) for the following values of the parameters: $d = 15$ μm, $\beta = 0.018$, $f = 90$ Hz; $d = 15$ μm, $\beta = 0.1$, $f = 32$ Hz; $d = 50$ μm, $\beta = 0.01$, $f = 170$ Hz; $d = 50$ μm, $\beta = 0.02$, $f = 150$ Hz; $d = 50$ μm, $\beta = 0.015$, $f = 416$ Hz;

†Such a combination for ξ_0 is chosen because, as follows from (50) and (51), in the linear region ($l \ll 1$) the optical effect is only determined by ξ_0^2/d and does not depend on the vibration frequency.

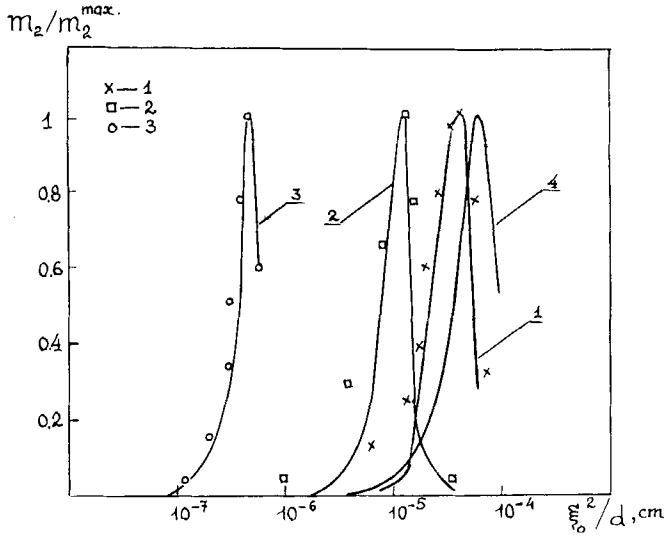

FIGURE 26 The behaviour of the ac component of the optical signal (second harmonic) under elliptic deformation at audible frequencies. Parameters discussed in the text.

$d = 100$ μm, $\beta = 0.04$, $f = 416$ Hz; $d = 50$ μm, $\beta = 0.9$, $f = 1468$ Hz. Experimental values of m_0/m_0^{max} for these conditions are also shown in Figure 25 (notation 2–8).†[57,58] It should be noted that the data of Figure 25 reveal a distinct correlation: the larger the parameter l, the greater is the discrepancy between polarization modulation curves 2–7 and curve 1 calculated by relation (50) with an allowance for (52) (the linear effect range).‡ The same correlation is observed in the behaviour of the oscillating component. Figure 26 shows experimental and theoretical values of m_2/m_2^{max} (the second harmonic) for the following l values: 3 ($d = 15$ μm, $\beta = 0.02$, $f = 90$ Hz); 50 ($d = 50$ μm, $\beta = 0.05$, $f = 170$ Hz); 60 ($d = 100$ μm, $\beta = 0.04$, $f = 414$ Hz) (curves 1–3). The behaviour of the oscillating component in the linear region is shown by theoretical curve 4.

The data of Figures 25 and 26 indicate that for $l > 1$ the effect of polarization modulation under elliptic deformation can be described adequately if only non-linear interactions are taken into account.

†While comparing theoretical and experimental data, one should bear in mind that the calculations have been performed for the geometric centre of the layer which is, at the same time, the centre of the nematic "spill over." However, this is not often the case in experiment, which, probably, is the reason for the small shift of the experimental ratios m_0/m_0^{max} to higher ξ_0 values as compared to the calculational results (see curves 2, 4, 5, and 7).

‡Hereinafter the parameter l is calculated for $\xi_0 = \xi_0^{max}$ and corresponds to the first maximum on the polarization modulation curves.

Such a method of analysing the optical effect under elliptic deformation can easily be extended to shear deformation. In this case equation (44) takes the form

$$\gamma_1 \frac{\partial \varphi}{\partial t} - K_3 \Delta \varphi = -\alpha_2 \frac{\partial V}{\partial z}. \tag{56}$$

The velocity gradient $\partial V/\partial z = \omega(\xi_0/d)e^{-i\omega t}$ makes the director tilt through the angle

$$\varphi_1 = -\frac{\alpha_2}{\gamma_1}\frac{\xi_0}{d}\operatorname{Re} e^{-i\omega t}\left\{1 - \frac{\operatorname{sh}[\sigma_n z(1+i)] + \operatorname{sh}[\sigma_n(d-z)(1+i)]}{\operatorname{sh}[\sigma_n d(1+i)]}\right\}. \tag{57}$$

In this expression the second term in square brackets allows for the orienting effect of bounding plates; $1/\sigma_n = (2K_3/\gamma_1\omega)^{1/2}$ is the thickness of the surface layer within which this effect can be ignored.

Taking into account the above restrictions on the vibration frequency, which leads to $\sigma_n d \gg 1$, we can simplify expression (57) as follows

$$\varphi_1 = -\frac{\alpha_2}{\gamma_1}\frac{\xi_0}{d}\sin \omega t. \tag{58}$$

The optical transmissivity is given by[59]

$$m = \sin^2\left[\left(\frac{\alpha 2}{\gamma_1}\right)^2 \frac{\Delta n}{2}\frac{\xi_0^2}{d}\sin^2\omega t\right]\sin^2 2\theta_0, \tag{59}$$

which is equivalent to expression (49) for the optical effect under elliptic deformation of nematics in the linear region. This means that optical transmissivity due to periodic shear deformation is frequency-independent and related to the layer thickness and vibration amplitude only through the parameter ξ_0^2/d.

To summarize what has been said above, we consider Figure 27 which presents theoretical and experimental data concerning the frequency dependence of the polarization modulation of light (the dc component m_0) under shear and elliptic deformation. Here $\xi_0^{\max}$ is the displacement corresponding to the first maximum of the function $m_0 = f(\xi_0)$. Dashed lines 1–4 correspond to sample thickness 15 μm and β values of 0.001, 0.004, 0.018, and 0.1; solid lines 5–10 refer to a 50 μm sample and β values of 0.001, 0.1, 0.02, 0.05, 0.08, and 0.9. The solid lines are calculated by relation (54) and

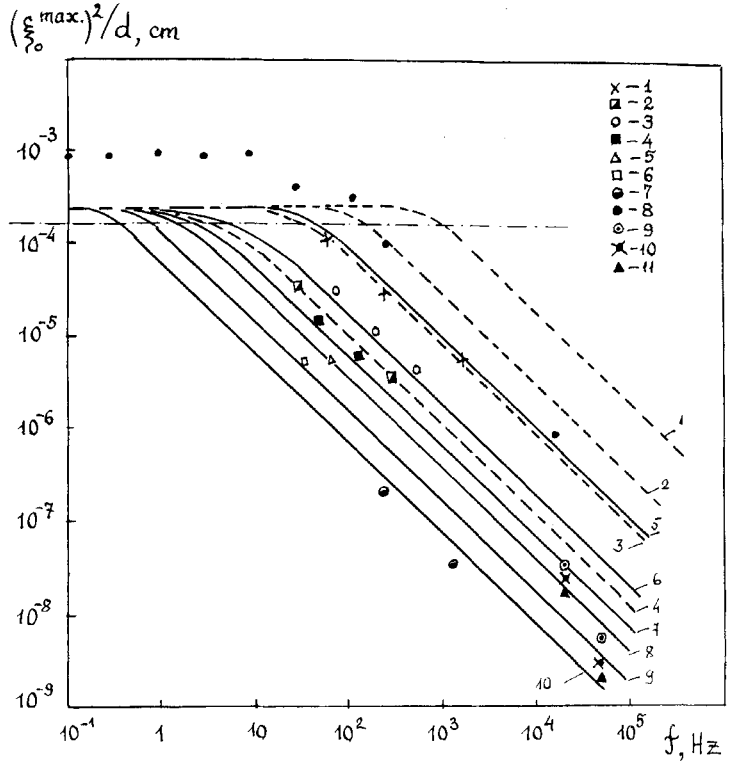

FIGURE 27 Theoretical and experimental frequency dependences of the polarization modulation of light under shear and elliptic deformation. Parameters discussed in the text.

show the frequency dependence of $(\xi_0^{max})^2/d$ under elliptic deformation. The dot-dashed line, calculated by (59), shows the behaviour of $(\xi_0^{max})^2/d$ under shear deformation. Comparison of the data shows that with elliptic deformation at low frequencies for small β and d, when $0 < l \ll 1$, the effect does not depend on the frequency; in this case $(\xi_0^{max})^2/d = 1.95 \cdot 10^{-4}$ cm, which is close to the value $1.2 \cdot 10^{-4}$ cm for shear deformation. For higher frequencies and $l \gg 1$ the parameter $(\xi_0^{max})^2/d$ decreases, which means that the extrema of the polarization modulation curves shift to lower ξ_0. For a constant ellipticity value this shift is larger for thick samples than for thin ones, and for a constant layer thickness the higher the value of β, the larger the shift.

Experimental results for elliptic deformation of a nematic (a mixture of MBBA and EBBA) for $l > 1$ are shown in Figure 27 and denoted by 1, 2 ($d = 15$ μm, $\beta = 0.02$; 0.1) and by 3–7 ($d = 50$ μm, $\beta = 0.01$, 0.02, 0.05, 0.08, and 0.9).[60] These results agree with theoretical predictions. As for

Bruchmüller data on shear deformation (notation 8),†[18] only at frequencies below 10 Hz is the parameter $(\xi_0^{max})^2/d$ frequency-independent, as it follows from the theory. Decreased values of this parameter at higher frequencies correlate with the behaviour of curves describing elliptic deformation of a nematic. We can assume therefore that in Bruchmüller's experiments the movable plate experienced "parasitic" transverse vibrations. If these vibrations are antiphase with the main vibrations in the layer plane, the ellipticity in Bruchmüller's experiments, as inferred from curves 5–7, amounts to ~ 0.005.

Expression (59) implies that as in the case of elliptic deformation, the light passing through the layer and analyser has a dc component and an oscillating component which is the sum of even harmonics. This theoretical prediction is confirmed by experimental results for mixtures of MBBA and EBBA at frequencies of about several hundred Hz.[4,57]

As is shown,[6,7] the optical transmissivity of a layer under shear deformation depends on the mutual positions of the vibration plane and the principal planes of the polarizers: it is maximal if the vibration plane coincides with one of the principal planes. The data were obtained in experiments with a 30 μm sample of ethyl *p*-ethoxybenzalamino-α-methylcinnamate. The plate was driven by hitting against its end-face with a pendulum. The maximal repetition rate of the impulses was 2.5 kHz. The experiments also revealed the effect of temperature on optical transmissivity. In a more recent work[10] these data were confirmed for a wider frequency range (20 Hz–20 kHz).

High frequencies. In this subsection we consider only the effect of surface acoustic waves on a nematic. As is known, a surface wave has two displacement components: one along the propagation direction (the Ox axis) ξ_x, and the other perpendicular to the plane where the wave is propagated, ξ_z. The amplitudes of these displacements are related by $\xi_{0_z}/\xi_{0_x} = -(2 - \varphi^2)/2(1 - \varphi^2)^{1/2}$.[20] For quartz, which is often used as an acoustic medium for surface waves, $\varphi = 0.87$, so that the longitudinal and transverse components are approximately the same ($\beta \simeq 1.3$). However, in theoretical analysis of the orienting effect of surface waves only the longitudinal displacement component is usually taken into account.

O. Kapustina and Yu. Statnikov[61] suggested a physical model of the phenomenon based on viscous-elastic effects. The component of the particle velocity along the propagation direction produces a viscous wave in the

†These experiments were performed with a 55 μm MBBA sample in the frequency range 0.1 Hz–21 kHz at room temperature.

liquid crystal layer. The velocity gradient

$$\frac{dV_x}{dz} = -V_{0_x} q_{\text{vis}} \cos(\omega t + \pi/4) e^{-q_{\text{vis}} z} \tag{60}$$

exceeds the other gradients†) and makes the director tilt through the angle φ_2.[61] This leads to a modification of the dielectric tensor

$$\epsilon_{ik} = \epsilon_{\parallel} l_{i1} l_{k1} + \epsilon_{\parallel} l_{i2} l_{k2} + \epsilon_{\perp} l_{i3} l_{k3} + \Lambda_0 \left(\frac{\partial V_i}{\partial x_k} + \frac{\partial V_k}{\partial x_i} \right), \tag{61}$$

where Λ_0 is Maxwell's constant. Introducing a coordinate system rotated through the angle φ_2 relative to the initial one and diagonalizing tensor (61),[62] we obtain

$$\varphi_2(x, z) = \frac{\Lambda_0}{\epsilon_{11}} \cdot \frac{\partial V_x}{\partial z}. \tag{62}$$

Since Maxwell's constant in nematics is known only for the isotropic phase,‡ this mechanism is more convenient to analyse by treating the problem rigorously.[64] Solution of Eq. (56) with substitution $\partial V/\partial_z \to \partial V_x/\partial z$ yields the following expression for the director tilt:

$$\varphi_2(x, z) = \frac{\alpha_2 \xi_{0_x} q_{\text{vis}}}{\gamma_1 (1 - q_{\text{vis}}^2/\sigma^2)} \times \left\{ e^{-q_{\text{vis}} z} \left[\cos(q_{\text{vis}} z + k'x - \omega t) + \sin(q_{\text{vis}} z + k'x - \omega t) \right] - e^{-\sigma z} \left[\cos(\sigma z + k'x - \omega t) + \sin(\sigma z + k'x - \omega t) \right] \right\}, \tag{63}$$

where k' is the surface wave number. Taking into account that the molecular tilt varies over the layer thickness and neglecting the first and higher powers of the ratio q_{vis}/σ as compared with unity, we obtain

$$m_0 = 5 L_0 k_0^2 (\Delta n)^2 \left(\frac{\alpha_2}{\gamma_1} \right)^4 \frac{\omega \rho}{\eta} \xi_0^4 \cos^4 k'x \sin^2 2\theta_0, \tag{64}$$

† $\dfrac{\partial V_z}{\partial x} = k' V_{0_z}$; $\dfrac{\partial V_z}{\partial z} \simeq \alpha V_{0_z}$; $\dfrac{\partial V_x}{\partial x} = k' V_{0_x}$

‡According to Ref. 63, for PAA in the temperature range 133–157°C corresponding to the isotropic state Maxwell's constant ranges from $7.5 \cdot 10^{-8}$ to $1.2 \cdot 10^{-8}$. For ordinary aromatic liquids, say benzene, $\Lambda_0 = 6.1 \cdot 10^{-14}$.

where L_0 is a dimensionless parameter dependent on the layer thickness and the wave numbers of the light in the liquid crystal and the bounding plates.[64] Since $\cos^4 k'x = \frac{3}{8} + \frac{1}{2}\cos 2k'x + \frac{1}{8}\cos 4k'x$, the clearing pattern of the layer should be in the form of alternating bright and dark fringes spaced at $\lambda'/2$ and less intensive fringes spaced at $\lambda'/4$ (λ' is the surface wavelength).

Such a pattern was observed in nematic samples of thickness 9–250 μm in the frequency range 2–35 MHz.[65–71] As can be seen from Figure 28, the pattern period Λ virtually does not depend on the layer thickness, and variation of Λ with frequency correlates with the change in the surface wavelength λ'. Dashed lines 1–6 show the values of $\lambda'/2$ at frequencies 2.6, 6, 12, 17.5, 18, 30, and 35 MHz. The values of Λ at these frequencies are labelled by 1–6. In most cases $\Lambda \sim \lambda'/2$, in agreement with the theory. Slight discrepancy with this prediction† may be caused by the interference‡ of several modes with different wave numbers excited in the layer when a surface wave propagates in one of the bounding plates. For example, in a layer of thickness less than 100 μm at frequency 12.3 MHz there exist the following three modes: symmetric (A) and antisymmetric (B) waveguide modes, and symmetric (C) surface-type mode.[66] The phase velocities C_{ph} of these modes as a function of the layer thickness are shown in Figure 29. Solid lines 1–3 represent the solution of the linearized wave equation corresponding to modes A, B, and C; dots are experimental values of C_{ph} obtained by Raman-Nath diffraction. It is not surprising, therefore, that some experimenters observed the variation of fringe periodicity and sometimes the dependence of $\Lambda(d)$ on the distance from the transducer. This is illustrated in Figure 28 where the data refer to the fringe pattern near the transducer and far from it (notation 3–3′; $f = 12.3$ MHz).

It should be noted that the maximal pattern contrast is observed when one of the polarizers makes the angle 45° with the fringe direction. This becomes clear from the diagram of Figure 30 which shows that the transmissivity angular distribution depends on the mutual orientation of the wave vector k' and the principal planes of polarizer P and analyser A. Precisely these conditions were realized in our experiments with a 40 μm MBBA sample at frequency 6 MHz (the displacement amplitude $\xi_{0_x} = 15$ Å). The sample was rotated about the optical axis through a step of 5°, while polarizers P and A remained crossed. As can be seen, $m_0 \sim \sin^2 2\theta_0$ and

†According to Ref. 65, in a 15 μm MBBA sample at frequencies 18 and 30 MHz the values of Λ slightly exceed $\lambda'/2$.

‡With homeotropically oriented molecules, a nematic layer only visualizes a complicated acoustic interference pattern; a spatially periodic director distribution, which arises in the layer along the surface wave propagation direction, is sometimes erroneously interpreted as the orientation instability of nematics.

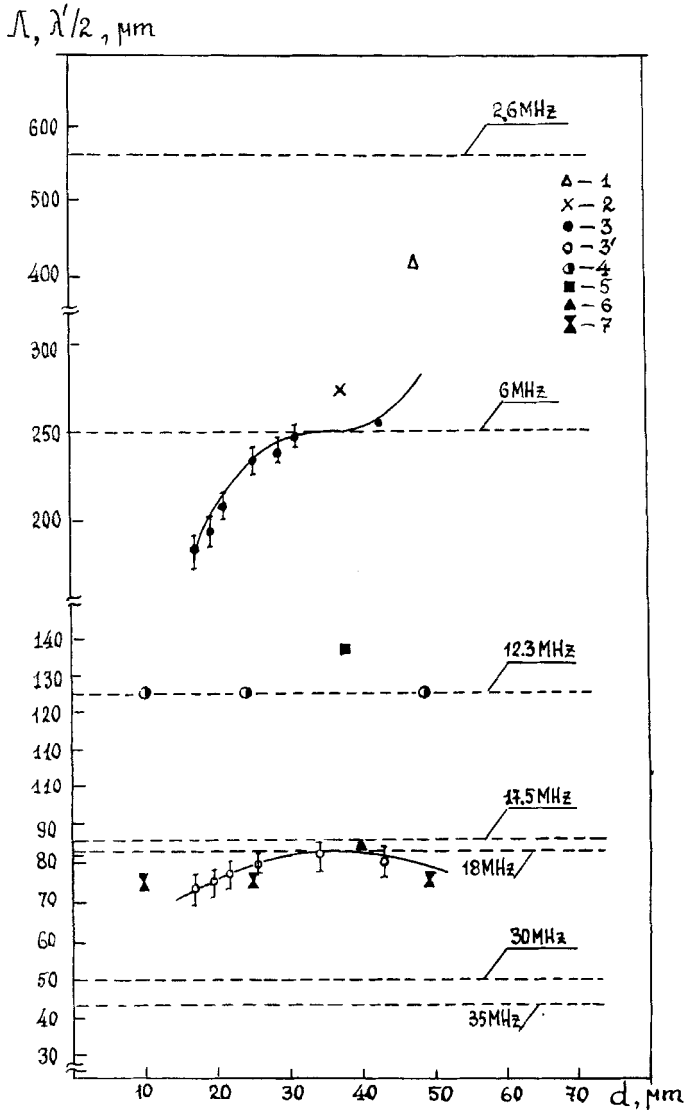

FIGURE 28 The spatial period Λ of the homogeneous deformation pattern in homeotropic nematic samples vs. the layer thickness in the 2–35 MHz frequency range (details in the text).

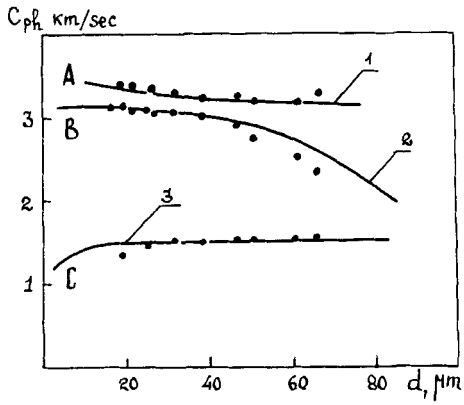

FIGURE 29 Phase velocities of three vibrational modes in an MBBA sample vs. the layer thickness; $f = 12.3$ MHz. Solid circles: experiments; solid lines: solutions of the linearized wave equation.

takes maximal and minimal values at $\theta_0 \simeq \pi/4 \cdot (2p + 1)$ and $\theta_0 \simeq \pi/4 \cdot p$, respectively ($p = 0, 1, 2, \ldots$), which agrees with the theory.

Let us estimate the effect numerically. For a 15 μm MBBA sample ($L_0 \sim 10^{-2}$) at frequency 6 MHz and displacement 10^{-6} cm the optical transmissivity, as calculated by relation (64), amounts to 10^{-8}, which is much lower than the value obtained in our experiments (see Figure 31a). At the same time, with displacement amplitudes less than 12–15 Å, i.e. for small director tilt, $m_0 \sim \xi_0^4$, as is predicted by the theory (Figure 31b).

Such considerable discrepancy between the theoretical and experimental results, though qualitatively they behave in the same way, shows that the effect cannot be attributed only to the horizontal component of the particle

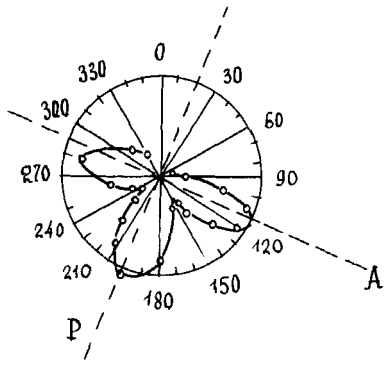

FIGURE 30 Angular distribution of the optical transmittance: $f = 6$ MHz; $\xi_0 = 15$ Å; $d = 40$ μm.

velocity and its gradient $\partial V_x/\partial z$. As was already noted, the vertical and horizontal displacements in a surface wave are approximately the same, and the ellipticity factor β is more than 1. Thus far, we have not touched upon the mechanism due to non-linear interaction of these components, though an allowance for this effect has led us to an adequate description of polarization modulation under elliptic deformation at audible frequencies.

We now consider the mechanism caused by acoustic flows. At audible frequencies, the director tilt due to convection is small, but it may be significant at high frequencies. Suppose that a surface wave propagating in the substrate gives rise to all three modes in the layer: A, B, and C (Figure 2). The flow velocities corresponding to these modes can be written in the form

$$V_A = \left(-xik'_A \cos n_A z + zn_A \sin n_A z\right)\phi_A e^{[(ik'_A - \alpha'_A)x - i\omega t]},$$

$$V_B = \left(xik'_B \sin n_B z + zn_B \cos n_B z\right)\phi_B e^{[(ik'_B - \alpha'_B)x - i\omega t]},$$

$$V_C = \left(xik'_C \operatorname{sh} n_C z + zn_C \operatorname{sh} n_C z\right)\phi_C e^{[(ik'_C - \alpha'_C)x - i\omega t]} \tag{65}$$

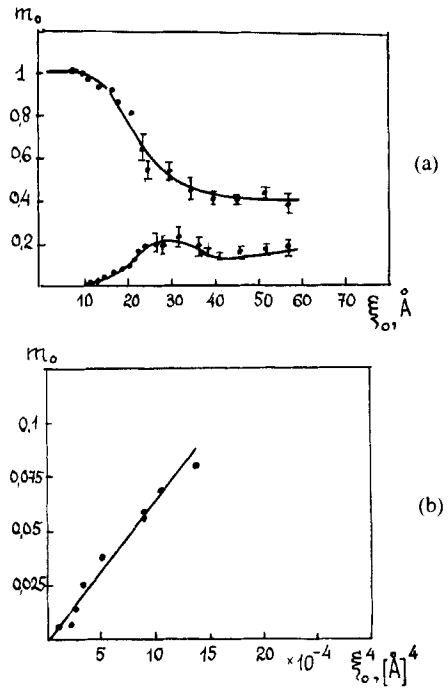

FIGURE 31 (a) Optical transmittance of monochromatic light as a function of surface wave displacement amplitude; MBBA; $d = 40$ μm; $f = 6.47$ MHz. (b) Optical transmittance of monochromatic light as a function of ξ_0^4; surface waves; MBBA; $d = 40$ μm; $f = 6.47$ MHz.

where ϕ_i is the amplitude factor, k_i is the wave number,† α_i' is the attenuation constant,‡ $n_A = (\omega^2/c^2 - k_A')^{1/2}$, $n_B = (\omega^2/c^2 - k_B')^{1/2}$, $n_C = (k_C' - \omega^2/c^2)^{1/2}$, c is the acoustic velocity in the liquid crystal. Using a conventional technique,[68] one can calculate the flow pattern and flow velocity in the acoustic field which arises as a result of the mixing of these modes. By equating the torque $(\alpha_2 \partial V_x^{(2)}/\partial z)$ and elastic moment, it is not difficult to estimate the director tilt and optical transmissivity due to a steady-state layer distortion. We do not present here the bulky expressions, but only consider some examples which illustrate the main results.

The profile of the director field distortion and the streamline pattern, as calculated for a 44 μm MBBA sample at frequency 12.3 MHz and acoustic intensity 5 mW/cm, are shown in Figure 32a.§ It was found that the formulae derived describe rather accurately the distribution of optical transmissivity over the layer plane (Figure 32b).‖ For example, the theory predicts that in thin samples (19–40 μm) the pattern period decreases (on moving away from the transducer) from $\Lambda = 2\pi/(k_C' - k_B')$ to $\Lambda = 2\pi/(k_B' + k_C')$, that is from 190–270 μm to 76–83 μm at frequency 12.3 MHz. This correlates with the experimental data of Figure 28 (notation 3, 8). However, this model based on the second-order effect cannot describe adequately the clearing pattern observed in experiment. For instance, the theory predicts that for small director tilt the transmissivity $m_0 \sim \xi_0^8$, whereas the experimental data fit the dependence of the form $m_0 \sim \xi_0^4$ (Figure 31b).

Medium frequencies. One of the first theoretical models developed to describe the optical behaviour of a nematic under shear deformation in the frequency range where the viscous wavelength is commensurate with the layer thickness considered a liquid crystal as an elastic medium obeying Hooke's law.[72,73] This erroneous suggestion has led to the conclusion, not confirmed by experiment, that the product $\xi_0^{th} f$ remains constant when the layer thickness and vibration frequency vary. For example, Kagawa,

†Raman-Nath diffraction experiments have revealed that for samples with thicknesses ranging from 19 to 65 μm the wave numbers vary within the following limits: 232–245 cm^{-1} for k_A'; 250–335 cm^{-1} for k_B'; 585–502 cm^{-1} for k_C'.

‡In a bounding glass plate (substrate) mode C decays more rapidly than modes A and B.

§Sandhu, Britten, and Stephens[68] have measured the velocity of these flows. At frequency 20 MHz in samples with thickness 12–254 μm it varies from 20 to 200 μm/s. According to Miyano and Shen,[66] the vortex scale in the direction normal to the layer plane is 10–20 μm at frequency 12.3 MHz and layer thickness 30 μm.

‖Calculation has been performed for a 44 μm MBBA sample at frequency 12.3 MHz with the values of the amplitude, phase velocity, and attenuation coefficient of the modes determined from light diffraction experiments: $k_A' = 239$ cm^{-1}, $k_B' = 266$ cm^{-1}, $k_C' = 515$ cm^{-1}, $\phi_A/\phi_B = 0.48$, $\phi_C/\phi_B = 0.33$.

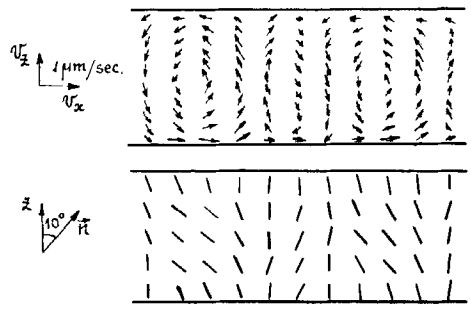

(a)

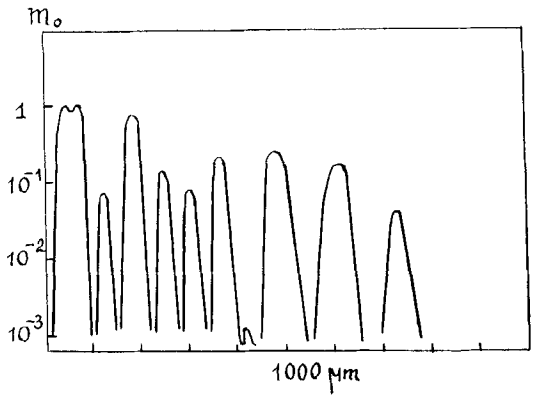

(b)

FIGURE 32 The Miyano-Shen model for the mechanism of director reorientation in a surface wave: (a) Theoretical director field distortion profile and streamline pattern; MBBA; $d = 44$ μm; $f = 12.3$ MHz; acoustic energy density = 5 mW/cm. (b) Optical transmittance distribution along the layer.

Hatakeyama, and Tanaka reported that for 66, 105 and 153 μm samples at frequencies 23.3 and 45.2 kHz the values of ξ_0^{th} amounted to 0.15 and 0.04 μm, which gives different values for $\xi_0^{\text{th}} f$: namely, 3.5 and 1.6 mm/s.

In this case too, we believe that the approach based on viscous wave field is more promising. The displacement of one of the bounding plates produces in the layer a viscous wave with the velocity gradient

$$\frac{\partial V_x}{\partial z} = -i\omega\xi_0(-1+i)q_{\text{vis}}e^{(-1+i)q_{\text{vis}}z}e^{-i\omega t}. \tag{66}$$

Substituting (66) into Eq. (56) and solving it, we obtain the following

expression for the director tilt

$$\varphi_2(x, z) = \frac{\alpha_2}{\gamma_1} \cdot \frac{\xi_{0x} q_{\text{vis}}}{\left(1 - q_{\text{vis}}^2/\sigma^2\right)} \left\{ e^{-q_{\text{vis}} z} \left[\cos(q_{\text{vis}} z - \omega t) + \sin(q_{\text{vis}} z - \omega t)\right] - e^{-\sigma z} \left[\cos(\sigma z - \omega t) + \sin(\sigma z - \omega t)\right] \right\}. \quad (67)$$

In this case the optical transmissivity is given by

$$m_0 = 20 L_0 k_0^2 \Delta n^2 \left(\frac{\alpha_2}{\gamma_1}\right)^4 \frac{\omega \rho}{\eta} \xi_0^4. \quad (68)$$

As in (64), L_0 is a dimensionless function.

We make some numerical estimates. For a 15 μm MBBA sample ($L_0 \simeq 10^{-2}$) at frequency 10 kHz and displacement amplitude 1.5 μm we obtain $m_0 \simeq 10^{-3}$, which does not agree with experiment. This can be seen from Figure 33a (curves 1, 2) which shows the dependence of m_0 on the vibration

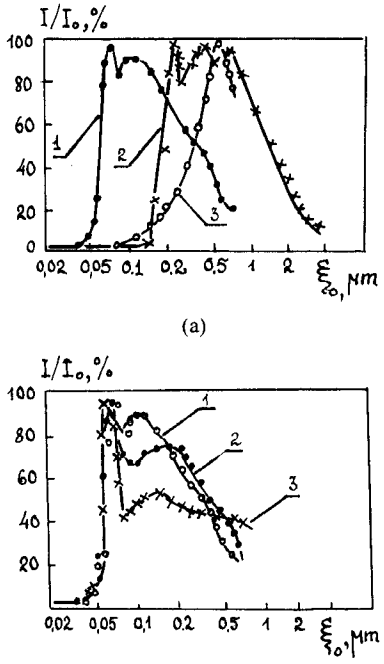

FIGURE 33 Optical transmittance of monochromatic light vs. the vibration amplitude: (a) MBBA; $d = 66$ μm; $f = 45.2$ and 23.3 kHz (curves 1 and 2); $d = 55$ μm; $f = 21$ kHz (curve 3). (b) MBBA; $f = 45.2$ kHz; $d = 66$, 105, and 153 μm (curves 1–3).

amplitudes for 45.2 and 23.3 kHz; here $d = 60$ μm, $t = 32°C$. These data lead to the following relation: $f(\xi_0^{th})^{1/2} = \text{const}$. Using this relation and taking into account that within the displacement interval $\xi_0^{th} \div \xi_0^{max}$ the behaviour of the polarization curves does not depend on the layer thickness (Figure 33b), we can estimate the value of ξ_0^{th} at 10 kHz. It turns out to be as low as 0.8 μm. It may seem that these experimental results cannot be explained within the framework of the theory considered above. In this connection, we should recall, first of all, the possible error in measuring ξ_0^{th}. For example, Bruchmüller's experiments performed under similar conditions ($d = 55$ μm, $f = 21$ kHz) gave the value[18] $\xi_0^{th} \leq 0.03$ μm (Figure 33a, curve 3). One should also bear in mind the effect of a "parasitic" vertical component of plate vibration, which was not monitored in any of the experiments mentioned above. We have already estimated the ellipticity value in Bruchmüller's experiments to be 0.005, but we failed to estimate this value for experiments of the Japanese authors because their data are rather scanty.

In conclusion of this section dealing with the optical behaviour of nematics under shear deformation we should point out that all the theoretical models used above are based on the common classical Leslie-Ericksen-Parodi approach.[74] Interpretation of the effect from the standpoint of linear mechanics gives no significant modifications of the general picture of the phenomenon. In Ref.[75] such calculations were performed for the following perturbations:

$$V|_{z=d/2} = V_0\delta(t), \qquad \text{pulsed disturbance;}$$

$$V|_{z=d/2} = V_0\cos\omega t, \qquad \text{shear deformation } (\lambda \gg L);$$

$$V|_{z=d/2} = V_0\cos k'x\cos\omega t, \qquad \text{shear deformation } (\lambda \ll d).$$

Solution of the equations of motion for the continuum of long molecular axes and their centres by the Laplace transformation method gives the following estimates for the optical transmissivity, respectively:

$$m_0 \sim V_0^2,$$

$$m_0 \sim V_0^2\cos 2\omega t,$$

$$m_0 \sim V_0^2\cos k'x. \tag{69}$$

These expressions do not contradict the results obtained by the classical approach, but we shall not go into details, for these results contain no new information.

I.1.2. Planar orientation

A. Compression deformation

Low frequencies. If the external perturbation of a layer is determined by the motion of one of its boundaries according to the law $V_z|_{z=d} = V_0 \sin \omega t$, the change in the layer thickness under such vibrations gives rise to a periodic variation of the phase difference of interfering ordinary and extraordinary rays, which in turn results in an oscillating intensity of light passing through the layer and analyser. Furthermore, such a deformation may cause the director to tilt in the plane normal to the layer, which also leads to the change in the phase difference as a result of refractive index variation.

This effect was studied in detail by G. Yakovenko on MBBA samples and mixtures of MBBA and EBBA in cells with free and fixed edges in the frequency range 70–2000 Hz. As in the case of homeotropic orientation the experiments revealed two types of modulation with frequencies f, $3f$, $5f$ (odd harmonics) and $2f$, $4f$, $6f$ (even harmonics). Figure 34 (curves 1 and 2) shows successive stages of the variation of modulation frequency with increasing vibration amplitude for a 50 μm sample in a free-edge cell

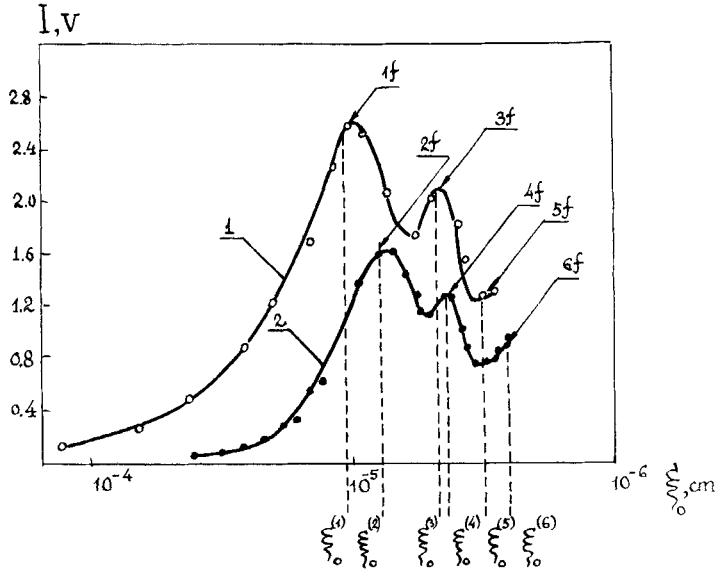

FIGURE 34 Two types of polarization modulation of light: at the initial moment the modulation frequency is equal either to the acoustic signal frequency (curve 1) or to the double acoustic frequency (curve 2). Free-edge MBBA layer; planar orientation; $d = 50$ μm; $f = 120$ Hz.

($f = 120$ Hz). Here $\xi_0^{(N)}$ is the displacement amplitude at which the harmonic Nf ($N = 1 \div 6$) appears. Curves 1 and 2 were obtained under the same conditions with the only difference that in the latter case the polarizer was rotated through 45°. The ratios $\tilde{A}_1$ of displacement amplitudes corresponding to the 2nd and Nth harmonic agree with predictions of the theory which describes optical effects in a homeotropic cell under compression deformation (see Figure 22b, notation 2). The displacement ξ_0^{th} corresponding to the first maximum increases with frequency as $\xi_0^{max} \sim f^2$.

For the cell with fixed edges the most peculiar point is a rather low effective clearing threshold as compared to the homeotropic cell. For a 50 μm layer at frequency 700 Hz this threshold is $P_S^{th} \sim 0.002$ atm, while in the homeotropic cell (under the same conditions) this value is about 2 atm.

High frequencies. In this frequency range there are few data on the optical properties of a planar cell under compression deformation; virtually all the data are shown in Figure 35.[19] The curves presented in the figure show the

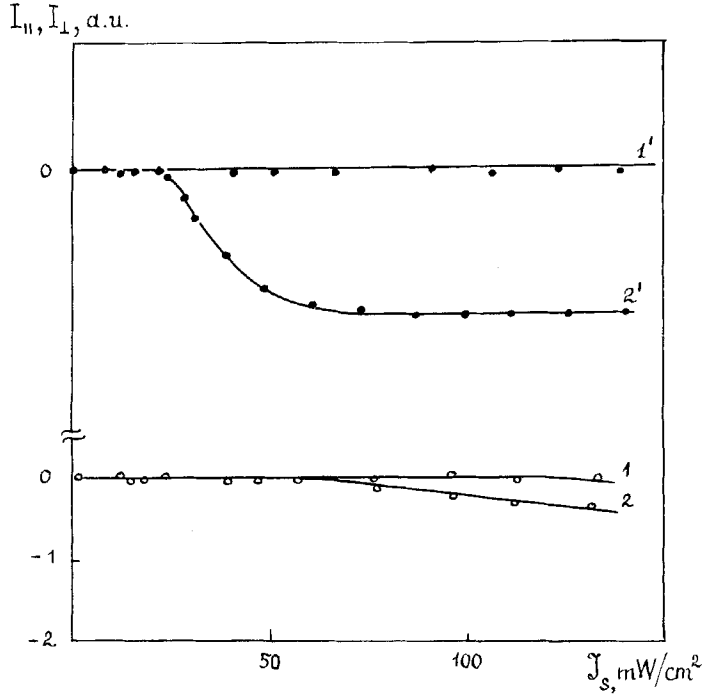

FIGURE 35 Optical transmittance of monochromatic light vs. acoustic intensity in planar MBBA samples of thickness 100 and 200 μm for crossed (curves 1, 2) and parallel (curves 1′, 2′) polarizers.

optical transmissivity of 100 and 200 μm MBBA samples as a function of acoustic intensity at 1.9 MHz. Curves 1 and 2 are obtained with crossed polarizers and curves 1′, 2′, with parallel ones. The experiments were performed in the configuration of Figure 1 with the acoustic beam incident on the layer at 30°. As can be seen, the optical effect is remarkably weak.

B. Shear deformation

It is clear from basic considerations that in a planar nematic sample subjected to shear deformation the distortion pattern does not depend only on the shear stress, but also on the director orientation relative to the shear. Indeed, one may imagine two extreme cases: 1) the director is parallel to the shear direction; 2) the director is perpendicular to the shear plane, i.e. the plane which includes the vectors of velocity and velocity gradient.

In the first case under static shearing the torque $\alpha_3(dV/dz)$ makes the director tilt about the horizontal axis through the angle φ given by $\tan^2\varphi = \alpha_3/\alpha_2$. For nematics, whose molecules are rod-shaped, the principle of entropy increase implies that $\alpha_2 < 0$, that is why this orientation of molecules is observed only for nematics with $\alpha_3 < 0$. Quantitative experimental data on the value of φ are rather scanty. For MBBA the following φ values are reported: 7°,[76] 8.2°,[77] and 15°.[78] It should also be noted that φ does not depend on the velocity gradient.

Of greater interest is the second case where the structure of a nematic crystal remains unperturbed up to a threshold velocity gradient

$$S^{\text{th}} = \pi^2 \left(\frac{K_1 K_2}{\alpha_2 \alpha_3} \right)^{1/2} \Big/ d^2. \tag{70}$$

In such experiments the director orientation is often fixed by an external, say magnetic, field.[79,80] In the absence of a destabilizing factor and for not too high magnetic field intensity the layer structure reveals a homogeneous distortion due to fluctuations of n_z and n_y (see Figure 36). As was shown,[80-82] two modes of homogeneous distortion are possible, depending on whether n_z and n_y are even or odd functions of z.† For $S \gg S^{\text{th}}$ homogeneous distortion turns into a characteristic pattern of roll-instability: a regular set of bright and dark fringes aligned along the shear direction with a period of about the layer thickness.[80,82] The same type of distortion

†The theory[81] predicts the existence of the transverse velocity component $V_x(z)$ caused by viscosity tensor anisotropy. For the first distortion mode V_x is an odd function of z: a wide roll aligned along the y-axis is formed in the layer. This case was analysed independently by Leslie.[83] For the second mode the theory predicts net flow in the same direction ($\int_{-d/2}^{d/2} V_x(z)\, dz \neq 0$).

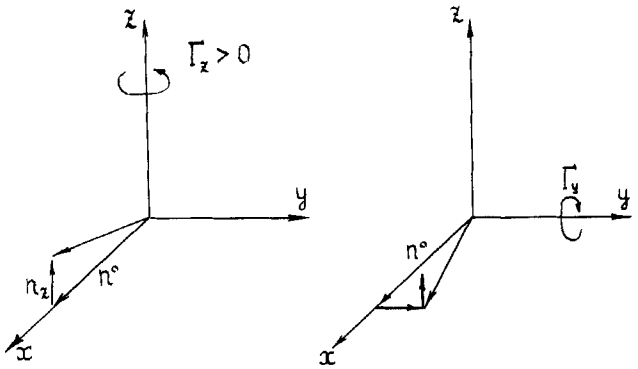

FIGURE 36 Mechanism of planar structure homogeneous distortion due to fluctuations of n_z and n_y.

can be observed just beyond the threshold, provided the magnetic field intensity is rather high.

Low frequencies. As for static deformation, in this frequency range of most interest is the case where the director is perpendicular to the shear plane. Experiments have shown that except for very low frequencies spatially periodic structure distortion (roll-instability) is a possible type of nematic distortion even without stabilizing magnetic field. This becomes clear from the following simple consideration. In the balance equation for the torques the viscous moment $\gamma \partial n_{y,z}/\partial t$ plays the same part as the magnetic moment $\chi_a H^2 n_{y,z}$, where χ_a is the magnetic anisotropy. Experiments have shown that in MBBA samples of thickness ~ 200 μm the stabilizing magnetic field, corresponding to the transition from homogeneous distortion to the roll-pattern, amounts to ~ 10^{+3} Gauss.[82] Once the distortion relaxation time in a magnetic field $\tau_0(H) = \gamma/\chi_a H^2$ is known, one can easily estimate the frequency ω_r corresponding to this transition: $\omega_r = 1/\tau_0 \simeq 3$ Hz.

High frequencies. Consider the case where shear occurs along the director orientation **n**. Such a case was studied by surface acoustic waves. According to the data[66] obtained on 20–60 μm MBBA samples at frequency 12.3 MHz, the director distortion pattern does not differ from that observed under the same conditions in homeotropic samples: it is a system of bright and dark fringes orthogonal to the wave propagation direction, which is clearly seen in parallel polarizers.† However, this distortion arises at somewhat higher acoustic intensities than in a homeotropic layer. In all probability, this is

†The light is polarized along the surface wave propagation direction.

due to the fact that the particle velocity gradient $\partial V_z/\partial x$, which causes reorientation of a planar sample, is small comparison with the gradient $\partial V_x/\partial z$ controlling the director tilt in a homeotropic sample.[66] It should be noted that the period of this pattern is distinct for sample edges spaced differently from the transducer, as in the case of a homeotropic sample. It can be seen from Figure 28 (notation 8) that in the latter case the pattern period for the edge next to the transducer depends on the layer thickness. As is shown in Ref. 71, the situation is the same for a planar sample. The data of Figure 37a refer to samples of MBBA and EBBA and their mixtures of thickness 9–20 μm; f = 17.5 and 35 MHz (curves 1 and 2, respectively).

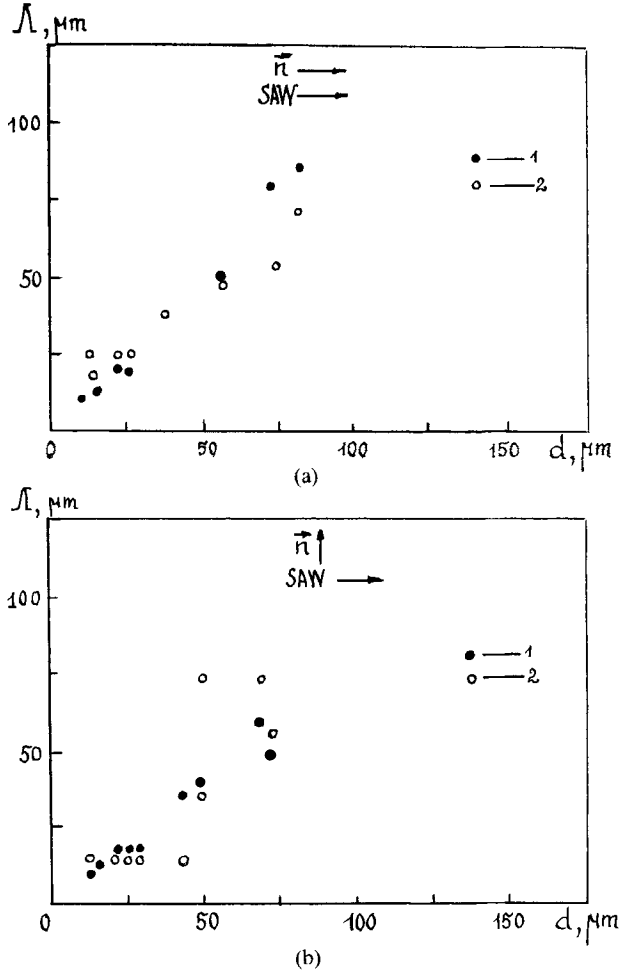

FIGURE 37 Spatial distortion period in 9–20 μm samples of MBBA, EBBA, and their mixtures at 17.5 and 35 MHz (1 and 2): $\mathbf{n} \| \mathbf{k}$ (a); $\mathbf{n} \perp \mathbf{k}$ (b).

Unlike the case of a homeotropic sample, in a planar sample the clearing pattern period does not depend on the vibration frequency.

If the director is perpendicular to the surface wave propagation direction, the clearing pattern coincides with that described above, but the fringes are parallel to this direction.[71] Figure 37b shows that the pattern period does not depend on the vibration frequency, but only on the layer thickness (curves 1 and 2 correspond to frequencies 17.5 and 35 MHz).

Interestingly, according to Refs. 66, 71, the distortion of a planar layer structure occurs only at a certain acoustic intensity, irrespective of the director orientation relative to the surface wave propagation direction. This effect was not observed in a homeotropic sample. This circumstance and also the fact that the fringes rotate through 90° when the director orientation varies relative to the surface wave propagation direction, while the fringe period does not depend on the wavelength, clearly show that here we again deal with orientation roll-instability of a nematic. This effect is considered in the next section.

I.2. Spatial-periodic distortion

This type of distortion in nematics subjected to mechanical compression produced by acoustic waves was first observed in non-oriented azoxyphenetole at ultrasonic frequencies (720 kHz and 1.8 MHz).[84,85] Acoustic fields of a certain intensity give rise to a cellular structure, so that the layer split into stationary zones flown round by moving liquid; the motion in these flows was both clockwise and counter-clockwise. Even these qualitative observations have shown that there exists a correlation between macroscopic flows and structural order distortion.

It is known that flow régimes in nematics are more complicated than those in an ordinary isotropic liquid because in the former case translational motion is associated with the internal orientational motion of the molecules. The flow, as a rule, distorts ordering and, vice versa, any change in molecular orientation (for example, due to an external field) in many cases leads to nematic flow. This correlation between the director and the flow velocity via viscous stress is the main factor which governs specific hydrodynamic properties of nematics and gives rise to various spatial-modulated structures.[21] Theoretical and experimental investigations carried out in recent years have yielded some quantitative relations which describe this type of distortion in steady-state and oscillating flows. It was found, for instance, that the Couette and Poiseuille flows may become unstable even for low Reynolds numbers.[86-88] The threshold of this orientation instability is determined by the Ericksen number $\mathrm{Er} = (\alpha_2\alpha_3/K_1K_2)^{1/2}S^{\mathrm{th}}d$ ($S^{\mathrm{th}} = (dv/dz)^{\mathrm{th}}$ is the threshold velocity gradient).[89] However, this conclusion is not always a common one and, as we shall see below, in the case of

oscillating flows some other dimensionless criteria (allowing for the oscillation frequency) are introduced to describe the behaviour of nematics. Important qualitative and quantitative distinctions are also observed in the properties of nematics with $\alpha_3 < 0$ and $\alpha_3 > 0$†: the former are oriented in a steady-state flow so that the director makes a certain angle with the flow direction; the latter do not exhibit such a behaviour. Below we shall consider the most significant peculiarities of the spatial-periodic distortion of nematics for different types of structure and deformation.

I.2.1. Homeotropic orientation

A. Shear deformation

Qualitative peculiarities of ordering perturbation and spatial-modulated structures in nematics in an oscillating flow become most apparent in the case of shear deformation. Here in homeotropic samples the director is always parallel to the velocity gradient, and the change in the oscillation frequency influences the velocity profile.

Low frequencies. In this frequency range the velocity profile is a linear function of the coordinate z, for the viscous penetration depth is much larger than the sample thickness. Clark *et al.*[90] have recently studied and interpreted the behaviour of thin nematic samples ($d = 10$ μm) with positive and negative α_3 under linear oscillating shearing (20–100 Hz). They found that if the displacement amplitude exceeds the threshold value ξ_0^{th} a new type of instability arises, namely, fringes with $W/d \sim 10^3$ where W is the fringe width. These fringes usually make the angle 35–40° with the substrate vibration direction, but in some areas they are parallel to this direction.‡

Let us analyse the conditions for instability onset, assuming that small perturbations are produced in the plane ZOX due to shear deformation. We use spherical coordinates and write the director components in the form (Figure 38):

$$n_x = \sin\varphi, \qquad n_y = \cos\varphi \sin\phi, \qquad n_z = \cos\varphi\cos\phi, \tag{71}$$

where φ is the azimuthal angle reckoned from the plane YOZ. Approximate

†The flow properties of nematics are described by six Leslie viscous coefficients α_i, two of which (α_2 and α_3) characterize the correlation between the flow and the molecular orientation.[21]

‡The authors of Ref. 90 believe that the inclination of the fringes relative to the substrate vibration direction can be attributed to a small vertical component of the substrate displacement.

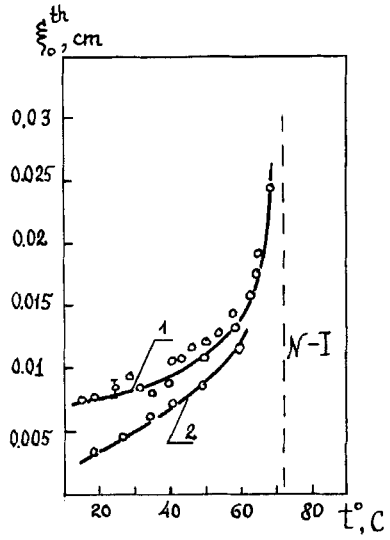

FIGURE 38 Temperature dependence of the threshold displacement amplitude for a 10 μm ZLI-518 sample: homeotropic orientation (curve 1); planar orientation (curve 2). Dashed line denotes the temperature at which $\alpha_3 = 0$.

calculation of the motions that give rise to perturbation build-up and instability development yields the following expression for the director tilt:

$$\tan\varphi = \beta_0^{-1/2}\tan\left[\frac{\xi_0}{d}\left(\beta_0^{-1/2} + \beta_0^{1/2}\right)^{-1}\sin\omega t\right] \qquad \text{for } \beta_0 > 0 \qquad (72a)$$

$$\tan\varphi = |\beta_0|^{-1/2}\tanh\left[\frac{\xi_0}{d}\left(|\beta_0|^{-1/2} - |\beta_0|^{1/2}\right)^{-1}\sin\omega t\right] \qquad \text{for } \beta_0 < 0. \qquad (72b)$$

$$\beta_0 = -\alpha_3/\alpha_2.$$

This expression implies different behaviour of nematics with opposite sign of α_3. For $\alpha_3 > 0$, the growth of the displacement ξ_0 leads to a sharp increase in the tilt oscillation amplitude which becomes infinite at the threshold displacement

$$\xi_0^{th} = \tfrac{1}{2}\pi d\left(\beta_0^{-1/2} + \beta_0^{1/2}\right), \qquad (73)$$

If $\alpha_3 < 0$, the angle φ oscillates with a finite amplitude not exceeding $\pm\tan^{-1}(|\beta_0|^{1/2})$, which corresponds to the interval between $\pi/2$ and direc-

tor orientation under static shearing (see Section 1.1.2). The factor $|\beta_0|^{-1/2}$ in expression (72b) (in front of tanh sign) shows that large deviations of φ are possible for small $|\beta_0|$, though this expression does not reveal explicit singularities. Determination of the critical amplitude in this case is beyond the scope of the calculation discussed.[90]

Oscillating shearing can induce orientation fluctuations in the layer plane. As is shown in Ref. 90, for β_0 values satisfying the condition $0 < \beta_0 \ll 1$ ($\alpha_3 > 0$) instability is developed at the threshold displacement given by (73). Of most interest is the case of negative α_3. According to Ref. 90, perturbation build-up means that the inequality $D_0 = n_y^2|_{\varphi=\pi/2}/n_y^2|_{\varphi=0} \ll 1$ is satisfied. Since D_0 can be expressed approximately as $D_0 \sim (1 - |\beta_0|\tan^2\varphi)^{1/\lambda''}$, it is obvious that this parameter may have a rather low value, provided $\tan^2\varphi \to 1/\beta_0$ (here $\lambda'' = \eta_3/(\eta_1 - \alpha_2^2/\eta_1)$). Hence, the theory predicts orientation instability of homeotropic nematics with $\alpha_3 < 0$ subjected to oscillating shearing.

Let us discuss some experimental data. Figure 38 shows the temperature dependence of the threshold amplitude for a 10 μm ZLI-518 sample (curve 1). This dependence is remarkable in that it illustrates how ξ_0^{th} varies with β_0 decreasing in the range $0 < \beta_0 < 1$.† The data of Figure 38 imply that $1/(\xi_0^{\text{th}})^2$ is a linear function of temperature; this confirms the theoretical prediction about correlation between ξ_0^{th} and β_0 (see (73)) because near the inversion point β_0 is also a linear function of temperature. Relation (73) shows that ξ_0^{th} does not depend on the vibration frequency, which also agrees with experimental data.

These features of the threshold characteristics of instability observed by Clark *et al.*[90] indicate that it is not similar to the roll-instability observed by Scudieri at frequencies ~ several kHz on 200 μm MBBA samples.[91] In the latter case the spatial-modulated structures are aligned at 90° to the vibration direction and their period is about the layer thickness. At frequency 7.46 kHz the threshold displacement, at which the roll pattern is stable, is 0.057 μm, and distortion of a regular fringe pattern occurs at 0.3 μm.[91] According to Scudieri, the fringe pattern arises as a result of periodic director distribution in the layer plane due to an ordered eddy motion‡ which gives rise to a periodic change in the extraordinary ray refractive index, since at the vortex centre, where the velocity gradient is maximal, the orienting action of such a motion is especially pronounced. These cylindri-

†In this nematic at room temperature β_0 satisfies the condition $0 < \beta_0 \ll 1$ and tends to zero with the decreasing temperature. The inversion temperature of ZLI-518, at which $\beta_0 = 0$, is 73° C.

‡Scudieri observed this eddy motion by introducing foreign particles into the layer.

cal vortices (rolls) act as lenses focusing light into bright domain lines. In adjacent vortices the particles move in opposite direction, and within each vortex the motion takes place in the vertical plane parallel to the periodicity direction.

It should be noted that roll-instability admits another orientation of spatial-modulated structures. This type of orientation was observed in Scudieri's experiments with a cell (filled with MBBA) whose walls were slightly non-parallel (the inclination angle $\sim 1.2 \cdot 10^{-3}$).[91] He observed two roll patterns: one was aligned perpendicular to the maximal director tilt (at displacement 0.814 μm) and the other, perpendicular to the shear direction (at displacement 0.817 μm). These data refer to the cell area of thickness 50 μm. Roll interference leads to a complicated spatial-periodic director distribution which is correlated only in the transverse direction, but not along the sample length. As the displacement increases to 0.82–0.83 μm, the pattern becomes more distinct.

High and medium frequencies. In this section we shall consider the spatial-periodic distortion of nematics and its specific features in the frequency range where the following condition is valid: $\lambda_{vis} \ll d \ll \lambda$, that is from several MHz (for $d \simeq 10^{-3}$–10^{-2} cm) to tens of kHz (for $d \simeq 10^{-2}$ cm).

Analysing the hydrodynamic equations of nematics with an allowance for the non-linear terms, I. Chaban has demonstrated the possibility of parametric instability.[92] In this case the viscous wave generated by one of the bounding plates vibrating in the plane acts as a pumping field (the wave propagates along the OZ axis). The threshold displacement corresponding to a periodic variation of the director tilt along the OX axis is given by

$$\xi_0^{th} = ad\left\{\frac{K_1\rho\left[4q^4 - (\pi/d)^4\right]}{4\gamma_1(-\alpha_2 - 0.5\alpha_5)q^4}\right\}^{1/2}, \tag{74}$$

and the wave vector of this distortion exceeds several times π/d. It follows from this relation that for a 100 μm MBBA sample $\xi_0^{th} = 0.248$ μm at 23.3 kHz, which agrees, according to the author of the model of Ref. 92, with the threshold of the onset of domains observed by Japanese researchers.[72,73] But the experimental dependences do not fit the model considered. This is clearly seen from Figure 39 where curves 1–3 (the layer thickness 66, 105 and 200 μm respectively) are calculated by relation (74); items 1 and 2 correspond to the experimental values of ξ_0^{th} for 66 and 105 μm MBBA samples.[72,73] Figure 39 also presents the experimental threshold of domain

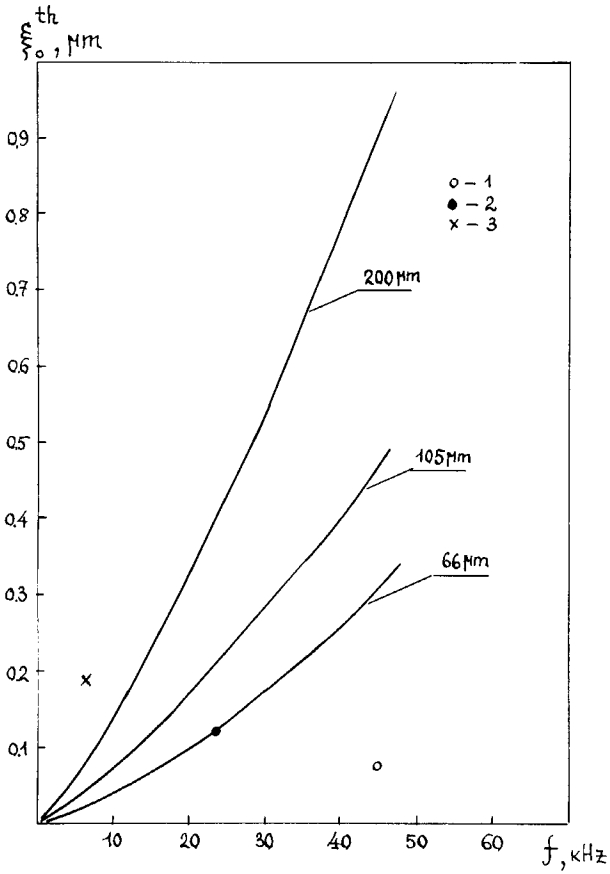

FIGURE 39 Effect of layer thickness on the threshold displacement amplitude corresponding to spatial-periodic distortion. Experiments on MBBA at ×—7.46 kHz; ●—23.3 kHz; ○—45.2 kHz.

formation reported by Scudieri[91] for the 200 μm MBBA sample at 7.46 kHz (item 3). This threshold correlates with the data of the Japanese researchers.

Experiments show that above the deformation threshold the spatial distortion period Λ decreases with the increasing displacement.[72,73,93] For example, according to Refs. 72, 73, in a 105 μm MBBA sample the distortion period is 150 and 70 μm for displacements 0.4 and 0.6 μm, respectively (f = 23.3 kHz).

It should be noted that, as in the case of low frequencies, the domain lines observed in these works were always aligned perpendicular to the displacement direction.

B. Elliptic deformation

We have already said that elliptic deformation is realized in the following two cases:

(1) the boundary plates both vibrate in the plane in mutually orthogonal directions (elliptic shearing);

(2) the bounding plates (both or one of them) vibrate in such a manner that elliptic motion is formed by the vertical and horizontal displacement components of the plates.

Elliptic shearing has been studied in detail, both theoretically and experimentally, by the Orsay team.[89,94-101] We now discuss the results of these works.

The behaviour of nematics at low elliptic shearing amplitudes and above the linear instability threshold (in the frequency range where $\lambda_{vis} \gg d$) was first experimentally studied and interpreted by Guyon and Pieranski with 20–100 μm MBBA samples.[89] A comprehensive theoretical analysis of the situation was made by Dubois-Violette and Rothen.[94] Later, Guyon and Dreyfus[95] conducted systematic instability studies in a wider dynamic range (up to displacements causing the destruction of convective structures†) and found new specific features in the behaviour of nematics. Furthermore, Guyon, Dreyfus, and Pieranski[96] established that only in thick samples ($d > 30$ μm) does the experimental instability threshold agree with theoretical predictions.[94] Bestgen, Dubois-Violette, Rothen, and Sadik[97] developed a more rigorous model allowing for time dependence of fluctuations which describes well the behaviour of thin nematic samples and gives the exact form of the threshold curve that could not be determined earlier.

Below we have attempted to summarize the data of these experiments and outline the general picture of nematic behaviour under elliptic shearing.

If the bounding plates perform $\pi/2$-shifted vibrations in the OXY plane along the mutually orthogonal directions (axes X and Y), the resultant velocity field can be written in the form‡

$$v_x^0 = \left(z + \frac{d}{2}\right)\frac{\xi_{0_x}}{d}\omega\cos\omega t,$$

$$v_y^0 = \left(z - \frac{d}{2}\right)\frac{\xi_{0_y}}{d}\omega\sin\omega t,$$

$$v_z^0 = 0. \qquad (75)$$

†A systematic study of this transition regime and convective structure evolution was carried out by Guazzelli.[99-101]

‡The coordinate system XY is so chosen that its origin coincides with the layer centre.

Using the nematodynamic equations,[74] we can easily find the director oscillations that produce, via the viscous torque $\alpha_2(\partial v_x/\partial z)$, a velocity gradient. For low displacement amplitudes ξ_{0_x} and $\xi_{0_y} \ll d$ orientation distortions can be written as

$$n_x^0 = -\left(\frac{\alpha_2}{\gamma_1}\right) \cdot \frac{\xi_{0_x}}{d} \sin \omega t,$$

$$n_y^0 = \frac{\alpha_2}{\gamma_1} \cdot \frac{\xi_{0_y}}{d} \cos \omega t,$$

$$n_z^0 = 1. \tag{76}$$

This means that for small shear gradients the director follows the plate displacement and describes the elliptic cone whose axis coincides with the elliptic shearing axis (stability region). In experiments this motion is usually observed as a slow shift of the conoscopic pattern formed when the sample is illuminated with light of frequency $\omega/2\pi$; the centre of the pattern moves along the ellipse whose principal axis coincides with the shearing direction.[89,95]

To determine the instability threshold for such a director motion, we write

$$\mathbf{n} = \mathbf{n}^0 + \delta\mathbf{n}(x, y, z),$$
$$\mathbf{v} = \mathbf{v}^0 + \delta\mathbf{v}(x, y, z), \tag{77}$$

and then analyse, using the nematodynamic equations, stability of solutions of system (75), (76) with respect to small perturbations $\delta\mathbf{n}$ and $\delta\mathbf{v}$. The analysis shows that above a critical value of the dimensionless parameter

$$N = \xi_{0_x}\xi_{0_y}\omega/D_0, \tag{78}$$

which characterizes the instability threshold under elliptic shearing,[89,95] the solution becomes unstable. The mechanism of this instability may be interpreted as follows: the perturbation $\delta\mathbf{n}$ produces viscous stresses which, in turn, give rise to a velocity change $\delta\mathbf{v}$ via correlation between $\mathbf{n}$ and $\mathbf{v}$. Such a flow can enhance the initial orientation distortion, provided diffusion relaxation to the initial states proceeds rather slowly.

Experiment has shown that this first instability represents a system of equidistant parallel rolls located in the XY plane and making the angle ψ_0 (with the X axis) determined by the shearing ellipticity (Figure 40). The width $\Lambda/2$ of the rolls depends linearly on the layer thickness (Figure 41).

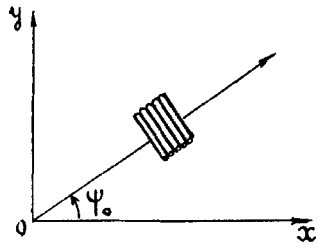

FIGURE 40 Position of rolls and the displacement ellipse; ψ is the angle between the normal to rolls and the Ox axis.

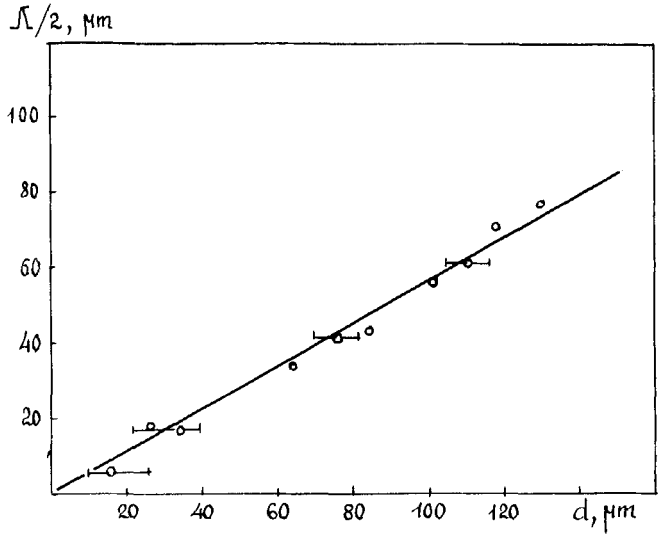

FIGURE 41 Effect of layer thickness on roll width.

Figure 42a and b shows roll-instability threshold diagrams as a relationship between two amplitudes ξ_{0_x} and ξ_{0_y} in 105 and 30 μm samples; these diagrams illustrate specific features of the behaviour of these amplitudes in thin samples. Items 1–3 correspond to frequencies 500, 280, and 200 Hz. For the 105 μm sample the curves approximating the experimental data obey the rule†

$$\xi_{0_x}\xi_{0_y}\omega = (1.4 \pm 0.3) \cdot 10^{-3}\ \text{cm}^2\ \text{s}^{-1}. \tag{79}$$

In thin samples the threshold variation curve deviates from this law near the

†If we use the value $N_1 \sim 500$ reported[95] for MBBA and put $D_0 \sim 10^{-5}$ cgs, we obtain the value of the same order of magnitude: $\xi_{0_x}\xi_{0_y}\omega \sim 0.5 \cdot 10^{-3}\ \text{cm}^2\ \text{s}^{-1}$.

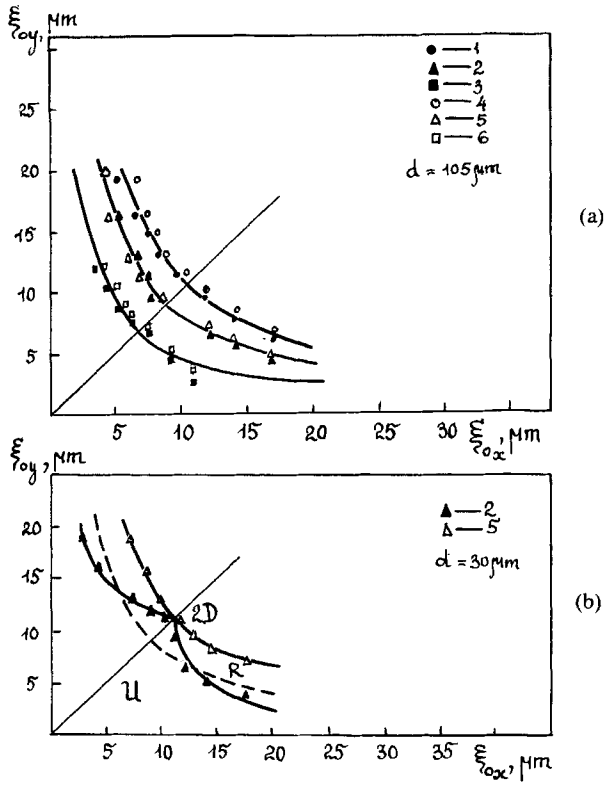

FIGURE 42 Threshold diagram for roll-instability (1–3) and two-dimensional distortion (4–6) at frequencies 200, 250, and 500 Hz, respectively in 105 μm (a) and 30 μm (b) samples.

"cusp point," corresponding to $\xi_{0_x} = \xi_{0_y}$, where it splits into two branches making the angle $2\theta_0$ (Figure 42b). (For comparison, this figure also presents the dashed threshold curve of Figure 42a for the 105 μm sample at 280 Hz.) A detailed experimental study of the "cusp point" was performed by Guazzelli.[98–100] According to her data, $\theta_0 \sim 1/d^2\omega$, as is predicted by the rigorous theoretical model.[97]

Let us turn to higher displacements ξ_{0_x} and ξ_{0_y}. Experiments have shown that at the second critical value N_2 linear domains are distorted, and a two-dimensional structure of rhomboid and square elements is formed in the sample.[95,100] The threshold diagrams for this transition are shown in Figure 42a and b (items 4, 5, and 6 for frequencies 500, 280, and 200 Hz, respectively).[95] In this case the condition $\xi_{0_x}\xi_{0_y} = \text{const}$ also holds for a thin sample. Observations have demonstrated that the layer exhibits such a pattern up to $N \simeq 2N_1$ when square domains co-exist with hexagonal ones, the latter as if "matching" squares with different orientation.

Elliptic deformation. In Section I.1 we discussed the homogeneous distortion of a homeotropic nematic when vibrations of the substrate in the plane are accompanied with its transverse vibrations at the same frequency, which leads to periodic layer compression. Precisely this "mixed" action, which we have called, for definiteness, elliptic deformation, produced spatial-periodic distortion of the layer structure observed in Refs. 101–103. For example, in experiments with a 50 μm MBBA sample at 57.1 kHz a stable roll-pattern of a period about the layer thickness was observed only for large horizontal displacements of the substrate (at the frequency of the acoustic transducer radial resonance).[101] Similar results were obtained[103] where samples with thickness up to 400 μm were investigated in the frequency range 23.7–100 kHz. As in the case of elliptic shearing, the roll period was found to grow linearly with layer thickness in the range $d = 50$–250 μm. Deviation from this law observed for samples thicker than 250 μm can be attributed to an additional system of linear domains. In samples thinner than 40 μm rolls were not formed. As can be seen from Figure 43a, the spatial period of distortion decreases with increasing vibration frequency; curves 1–2 correspond to 50 and 250 μm samples.[103] The change in the instability threshold is clearly seen from Figure 43b ($f = 23.7$ kHz) where the dashed section of the curve shows thresholds for the "double" system of domains.

C. *Compression deformation*

While analysing the behaviour of a nematic layer under compression resulting in substance "spreading" (a cell with free edges), I. Chaban considered the case of spatial-periodic distortion of a homeotropic structure due to parametric instability in the frequency range where $kd \ll 1$. As a periodic parameter driving the system, she used the solution of the linearized system of equations with periodic boundary conditions which appears in the system of equations for the next approximation through the quadratic terms. The threshold displacement at which the domain structure appears as dark and bright fringes perpendicular to the spreading direction is expressed as[15]

$$\xi_0^{\text{th}} = \pi^2 d \left[\frac{2K_3 \rho \frac{\tau_1}{L} (\eta - \alpha_2)(1 + k^2 \tilde{b}^2 L^2 / 4\pi q^2 d^2)}{k\gamma_1(-\alpha_2 - \alpha_5) b^2 (\mu_2 - \eta) b} \right]. \tag{80}$$

The wave vector of the distortion is $\mathbf{q} = 2\mathbf{k}$. The author of the model believes that a similar domain structure was observed in a free-edge cell by Sripaipan *et al.*[23] The similarity is, however, only accidental and, as was

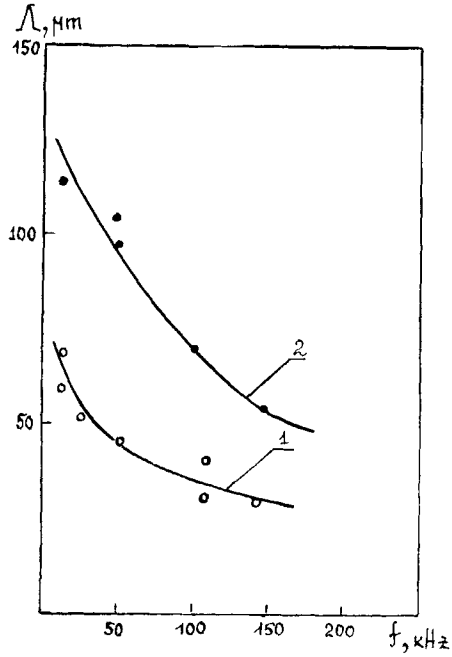

(a)

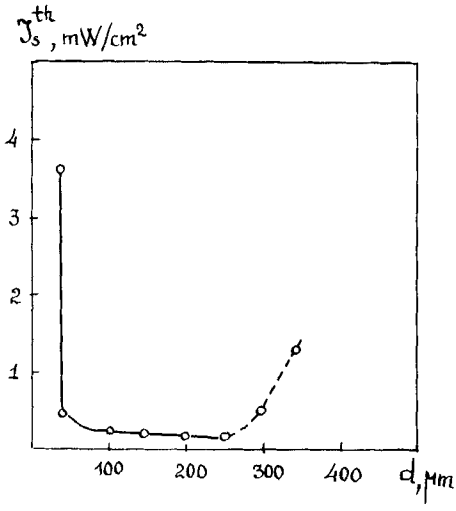

(b)

FIGURE 43 (a) Frequency dependence of spatial distortion period in 50 and 250 μm MBBA samples (1 and 2). (b) Effect of layer thickness on the instability threshold; MBBA; f = 23.7 kHz.

noted in Section I.1, periodic distribution of the director orientation was caused in these experiments by acoustic flows. Let us estimate the threshold of domain structure onset by relation (80). For a 70 μm MBBA sample at 1 MHz we obtain $\xi_0^{\text{th}} = 9 \cdot 10^{-7}$ cm, which corresponds to $b = \tilde{b} = 100$. The threshold decreases with the increasing b.

I.2.2. Planar orientation

A. Shear deformation

In this case the formation of spatial-periodic structures in nematics is governed by the director orientation relative to the shearing direction. We now discuss, from this point of view, the results of works[79-82,90,106-108] dealing with the effect of low-frequency oscillating shearing with a linear velocity profile on nematics.

The director lies in the shear plane. We have already pointed out that the behaviours of nematics exhibit essential qualitative and quantitative distinctions, depending on the sign of the Leslie viscous coefficient α_3.[104] Theoretical and experimental investigations have shown that in this case instability arises only if $\alpha_3 > 0$.[90] Let us discuss these results at greater length.

If one of the bounding plates vibrates in the OXY plane along the OX axis, the velocity and director components can be written in the form

$$v_x = v_{x_0}(z,t); \qquad v_y = v_{y_0}(z,t); \qquad v_z = 0;$$
$$n_x = \cos\varphi(z,t)\cos\phi(z,t); \qquad n_y = \cos\varphi(z,t)\sin\phi(z,t);$$
$$n_z = \sin\varphi(z,t). \tag{81}$$

If the vectors $\mathbf{n}$ and $\mathbf{v}$ are assumed to lie in the OXZ plane, approximate calculation of the motions that give rise to an instability

$$\dot{\varphi} = -\left(\sin^2\varphi + \beta_0\cos^2\varphi\right) B_0\omega\cos\omega t, \tag{82}$$

where $B_0 = |\alpha_2|\xi_0/\gamma_1 d$, $\beta_0 = -\alpha_3/\alpha_2$, yields the following expression for the director tilt:

$$\tan\varphi = -\beta_0^{-1/2}\tan\left[\left(\frac{\xi_0}{d}\right)\left(\beta_0^{-1/2} + \beta_0^{1/2}\right)^{-1}\sin\omega t\right] \qquad \text{for } \beta_0 > 0 \tag{83a}$$

$$\tan\varphi = |\beta_0|^{1/2}\tanh\left[\left(\frac{\xi_0}{d}\right)\left(|\beta_0|^{1/2} - |\beta_0|^{1/2}\right)^{-1}\sin\omega t\right] \qquad \text{for } \beta_0 < 0. \tag{83b}$$

This expression implies that for $\alpha_3 < 0$ and for all vibration amplitudes

oscillations of the angle φ have a finite amplitude and do not exceed the orientation angle in the flow $\pm\tan^{-1}(|\beta_0|^{1/2})$. If $\alpha_3 > 0$, oscillations of φ are small for low β_0 and ξ_0, but their amplitude grows so rapidly with ξ_0 that φ becomes infinite for the threshold displacement ξ_0^{th} given by (73). As far as the stability of the motion of $\mathbf{n}$ in the layer plane (OXY) is concerned, it is shown[90] that shear-induced small perturbations can grow (by magnitude) if two conditions are satisfied:

(1) The amplitude ξ_0 is sufficiently high, so that the ratio $n_y^2/(n_y^0)^2$ is either large or small (n_y^0 is the director component along the axis y at $\varphi = 0$). The first case corresponds to small transverse perturbations (the director lies in the layer plane) which are enhanced as the director rotates in this plane; in the second case the director does not lie in the layer plane, and transverse perturbations grow as the director returns to this plane. This condition can also be expressed in terms of the relation $D_0 = n_y^2|_{\varphi=\pi/2}/n_y^2|_{\varphi=0}$: instability takes place for $D_0 \gg 1$ or $D_0 \ll 1$, provided $2\gamma > \beta_0$ or $2\gamma < \beta_0$, where $\gamma = [(\gamma_2^2/\gamma_1) + \alpha_1]/[\eta_1 - (\alpha_2^2/\gamma_1)]$.[90]

(2) Such director motions arise for large deviations φ. Since $\beta_0 > -1$, it follows from (83b) that this condition is not fulfilled for $\alpha_3 < 0$; the situation is different for $\alpha_3 > 0$.

The above theoretical model is in a good agreement with experimental data obtained at frequencies 20–100 Hz for materials with different β_0.

Consider the region $0 < \beta_0 \ll 1$. As an example, Figure 38 shows the threshold displacement ξ_0^{th} in a 10 μm ZLI-518 sample as a function of temperature (curve 2). As was already noted, in this material the coefficient α_3 decreases with increasing temperature. The dashed line indicates the temperature of the nematic–isotropic liquid transition, which is equal for this material to the inversion point ($\alpha_3 = 0$). Curve 2 shows that, as in the case of homeotropic orientation, $1/(\xi_0^{th})^2$ is a linear function of temperature, which confirms the theoretical dependence of ξ_0^{th} on $\beta_0^{-1/2}$ (see expression (73)).†

The threshold displacement practically does not depend on the vibration frequency, even in the range corresponding to low Ericksen numbers (see Table I; the 10 μm ZLI-518 planar sample), which also agrees with the theory.

The behaviour of the threshold displacement for large positive β_0 is illustrated in Figure 44 for a 10 μm sample (the ester mixture of Dr. Demus, grade SS M). In this material the inversion point is equal to ~ 80 °C; as the temperature decreases, β_0 grows reaching 1 at 35 °C and then tends to infinity at the nematic–A smectic transition point. The solid line shows

†The values of ξ_0^{th} for planar and homeotropic samples differ significantly only at lower temperatures where the Ericksen number has a smaller value.

TABLE I

Frequency dependence of ξ_0^{th} at different temperatures.

	ξ_0^{th}, cm			
f, Hz	17 °C	34 °C	41 °C	50 °C
10	0.008			
20	0.008	0.008	0.01	0.011
30	0.008	0.008	0.009	0.011
40	0.008	0.008	0.01	0.011
50	0.007	0.007	0.009	0.012
60	0.006	0.008	0.01	0.011
70	0.006	0.007	0.01	0.011

temperature regions where instability was observed. Near the minimum of ξ_0^{th} there exists a stability "gap," which agrees with the theory.

The distortion pattern corresponding to instability does not depend on β_0. It is in the form of fringes parallel to the substrate vibration direction. The fringe width W decreases with the rising vibration frequency and increases with sample temperature (Figure 45, 10 μm layer of ZLI-518). It should be noted that fringes are observed only in crossed polarizers. The fringe width does not depend on the vibration amplitude, but as ξ_0 grows the central region of each fringe exhibits rolls with a period of about the layer thickness oriented perpendicular to the vibration direction.

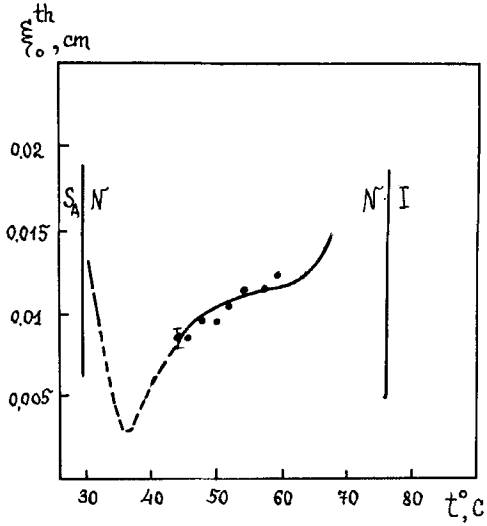

FIGURE 44 Temperature dependence of the threshold displacement amplitude for a planar 10 μm sample of the ester mixture (SSM grade); dashed line shows the "stability gap."

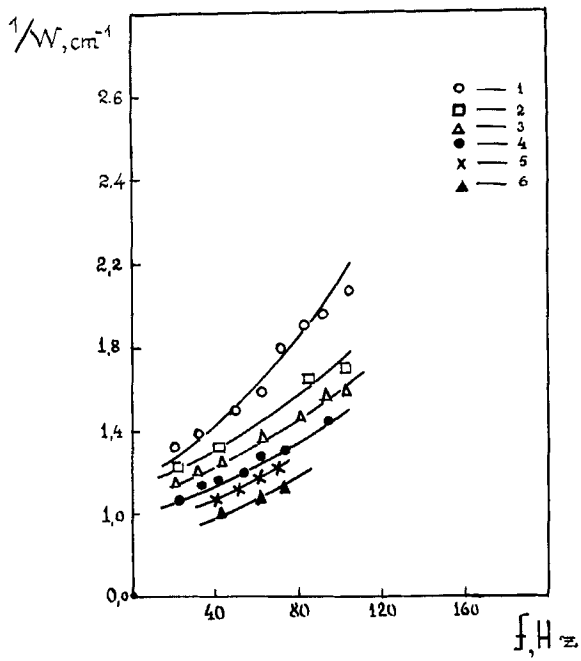

FIGURE 45 Effect of vibration frequency and temperature on the fringe width W of the instability pattern in a 10 μm planar ZLI-518 sample at 19, 32, 40, 52, 60, and 65°C (1–6, respectively).

The director is orthogonal to the shear plane. There is a large number of theoretical and experimental works[79–82] dealing with the behaviour of planar samples subjected to static or oscillating shearing in this geometry. Some of these studies have already been discussed in Section I.1.2 where the homogeneous deformation of the planar structure was considered. We recall that the structure remains stable up to a threshold velocity gradient S^{th} given by relation (70). The quantity S^{th} is the threshold of the so-called homogeneous instability (H-instability). If a sample is placed in a stabilizing magnetic field, the value of S^{th} increases and with fields exceeding a critical value H_c homogeneous distortion is not observed, but rolls arise, their axes being oriented along the shearing direction (roll (R)-instability).

The mechanism of the R-instability was discussed in Refs. 79–82. Rigorous treatment of this instability requires a complicated mathematical apparatus developed in Ref. 81. Here we shall use a simpler approach. Following Ref. 82, we consider the case where the stabilizing magnetic field is parallel to the X axis and the electric field to the Z axis. The fluctuations

can be represented in the form

$$\begin{aligned} n_{y,z}(x, z, t) &= n_{y,z}(t)\cos q_x x \cdot \cos q_z z, \\ v_{y,z}(x, z, t) &= v_{y,z}(t)\sin q_x x \cos q_z z, \\ v_x(x, z, t) &= v_x(t)\cos q_x x \sin q_z z, \\ P(x, z, t) &= P(t)\sin q_x x \sin q_z z. \end{aligned} \tag{84}$$

We can find the instability threshold by equating the elastic, magnetic, electric, and viscous moments:

$$\begin{aligned} \Gamma_y = 0 &= \left(K_1 q_z^2 + K_3 q_x^2 + \chi_a H^2 - \frac{\epsilon_a}{4\pi} E^2\right) n_z + \alpha_2 q_x v_z \\ &\quad + \alpha_3 (q_z v_x + s n_y), \\ -\Gamma_z = 0 &= \left(K_2 q_z^2 + K_3 q_x^2 + \chi_a H^2\right) n_y + \alpha_2 (q_x v_y + s n_z). \end{aligned} \tag{85}$$

This system is reduced to two equations for n_y and n_z

$$\begin{aligned} f_y n_y + A s n_z &= 0, \\ f_z n_z + B s n_y &= 0. \end{aligned} \tag{86}$$

From the condition that these equations are compatible we obtain the threshold of R-instability†

$$S^{\text{th}} = \left(\frac{f_y f_z}{AB}\right)^{1/2}, \tag{87}$$

where $f_y = K_2 q_z^2 + K_3 q_x^2 + \chi_a H^2$; $f_z = K_1 q_z^2 + K_3 q_x^2 + \chi_a H^2 - (\epsilon_a/4\pi)E^2$; A and B are functions of q_x, q_z, α_i, η_i and d.

In a strong magnetic field ($q_x^2 \gg q_z^2$) we can set $E = 0$ and $K_1 = K_2 = K_3 = K$, thereby obtaining from (87)

$$S^{\text{th}} = \frac{\left[K\left(q_x^2 + q_z^2\right) + \chi_a H^2\right]}{\left(\alpha_2' \cdot \alpha_3'\right)^{1/2}} \left[1 + 2\lambda''\left(\frac{q_z}{q_x}\right)^2\right]^{1/2} \tag{88}$$

†In the limiting case $q_x \to 0$, which corresponds to H-instability, (87) changes to (70) if we put $q_z = \pi/d$.

where α_2' and α_3' are combinations of viscous coefficients, $\lambda'' = f(\alpha_i, \eta_i, d)$.† The distortion wavelength Λ is related to the layer thickness and magnetic field by

$$\frac{d}{\Lambda} \sim (Hd)^{1/2}. \tag{89}$$

These results agree well with special experiments on static Couette flow in a cylindrical cell (the stabilizing magnetic field is along the cell axis).[82] Experimental values of the threshold and distortion wavelength Λ in terms of $S^{th}d^2$ and d/Λ, respectively, are shown in Figure 46a and b (points).

We have already pointed out that under static shear deformation, or in a static flow, roll-instability arises only in the presence of a stabilizing magnetic field H_c. Experiments[80,82] have shown, however, that under oscillating shearing this type of instability can also arise without a stabilizing field if the oscillation frequency is appropriately chosen: it must exceed the frequency of the distortion relation in a magnetic field $\omega \sim \chi_a H_c^2/\gamma$,[82] which separates the regions of H- and R-instabilities.

Using an approximate analysis similar to that employed in the above case, we shall consider the main features of R-instability under oscillating shearing. Two types of periodic deformation are considered:

1) sinusoidal $\quad S(t) = S_0\sqrt{2}\cos\omega t;$

2) square $\quad S(t) = +S_0 \quad$ for $0 < t < T/2$

$\qquad\quad S(t) = -S_0 \quad$ for $T/2 < t < T.$ (90)

Equating the torques, we obtain

$$\dot{n}_y + n_y/T_y + A'sn_z = 0 \tag{91a}$$

$$\dot{n}_z + n_z/T_z + B'sn_y = 0 \tag{91b}$$

where $T_y = \gamma_y/f_y$ and $T_z = \gamma_z/f_z$ are the spontaneous relaxation constants for distortions characterized by the components n_y and n_z; γ_y and γ_z are the effective rotational viscosities.

†According to Ref. 104, for MBBA at a temperature 25 °C $(\alpha_2' \cdot \alpha_3')^{1/2} = 0.21P$; $2\lambda'' = 1.47$.

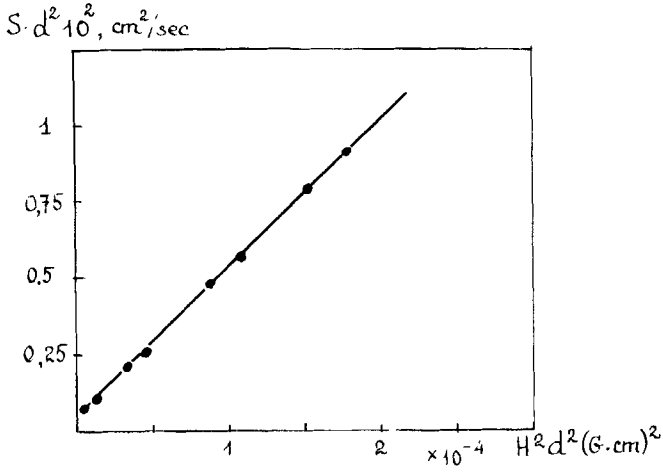

(a)

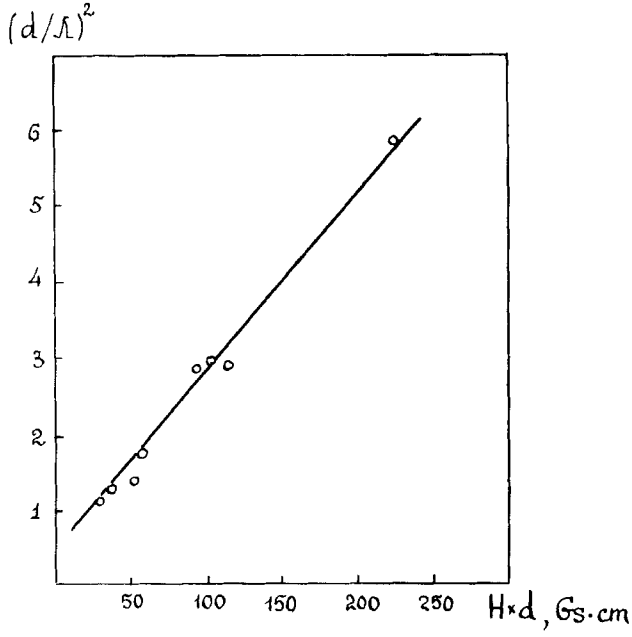

(b)

FIGURE 46 Effect of layer thickness on (a) the roll-instability threshold and (b) the distortion wavelength. The points are experimental values.

Solution of these equations gives two types of R-instability:

$$\begin{aligned} n_y(t + T/2) &= -n_y(t) \\ n_z(t + T/2) &= n_z(t) \end{aligned} \qquad (Y\text{-mode})$$

and

$$\begin{aligned} n_z(t + T/2) &= -n_z(t) \\ n_y(t + T/2) &= n_y(t) \end{aligned} \qquad (Z\text{-mode}) \qquad (92)$$

Figure 47 shows the time behaviour of the director fluctuations n_y and n_z corresponding to the Y-mode in the case of square deformation; it can be seen that only n_y crosses zero for the deformation period. The threshold gradient of this mode of R-instability is given by the following expressions:

$$\frac{(S^{\text{th}})^2 A'B'T_yT_z}{1 + \omega^2 T_y^2} = 1 \qquad (93)$$

$$(S^{\text{th}})^2 A'B'T_yT_z\left[1 - \frac{\tanh(T/4T_y)}{T/4T_y}\right] = 1. \qquad (94)$$

They correspond to sinusoidal and square deformation. The Z-mode differs from the Y-mode only in that n_z crosses zero and in expressions (93) and (94) T_z should be substituted for T_y.

It is shown[80,82] that as the relaxation time T_z decreases in a high-frequency electric field E, or as the relaxation times T_y and T_z decrease in a stabilizing

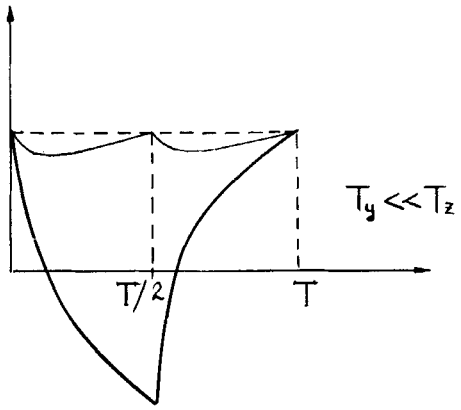

FIGURE 47 The behaviour of fluctuations of n_y and n_z for the Y-mode.

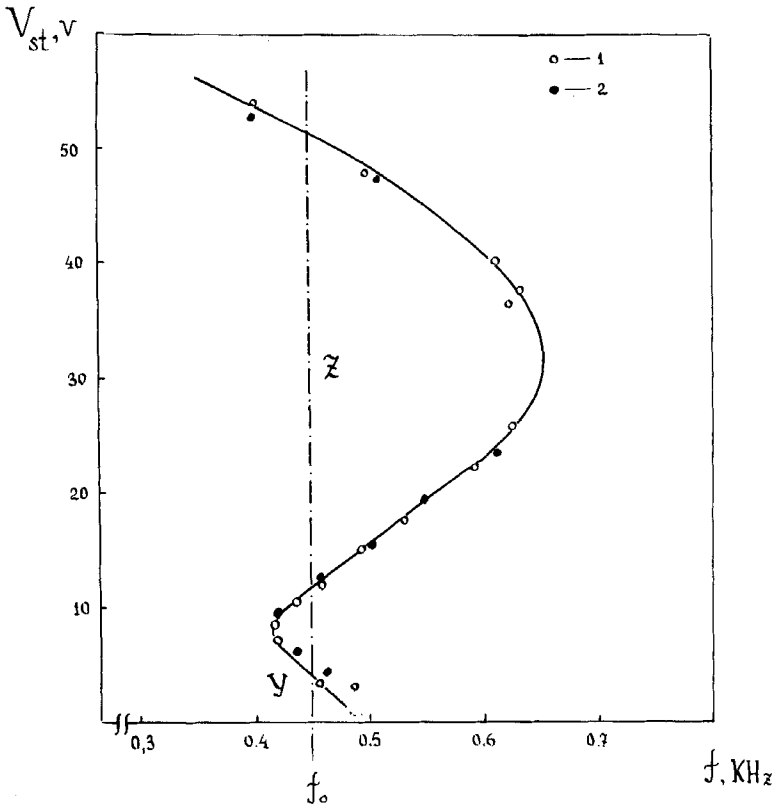

FIGURE 48 Diagram of roll-instability thresholds for sinusoidal and square-pulse excitation (1 and 2, respectively).

magnetic field, the thresholds change and one distortion mode is transformed into the other. This transition is clearly seen in Figure 48 which shows the experimental diagram of the *R*-instability thresholds for sinusoidal and square deformation (1 and 2, respectively). Here V_{st} is the voltage of stabilizing electric field, f is the oscillation frequency; the magnetic field and oscillation amplitude were constant in this experiment. The *R*-instability threshold has been determined with a high accuracy by the onset of a diffraction pattern and change in the intensity of light in one of its maxima.†

Suppose the vibration frequency is equal to f_0. We analyse the behaviour of the system when the stabilizing electric voltage increases. At $V_{st} = 0$ the

†This paper[105] reports a detailed study of spatial-modulated structures of *R*-instability (as optical phase gratings) by diffraction of light for normal and oblique incidence.

sample exhibits Y-type roll-instability when the director component n_z characterizing the distortion in the vertical direction (along the Z-axis) does not change sign, while the sign of the component n_y changes every half period. This type of instability disappears in electric field $E = E_1$. At a higher voltage ($E = E_2$) roll-instability of Z type arises. For R-instability of this type the sign of the director component n_z (but not n_y) and intensity of bright and dark fringes change every half period. This type of instability exists up to $E = E_3$. These features of roll-instability are observed at frequencies exceeding the critical point A. At lower frequencies, say $f = f_2$, and at $V = 0$ we again have instability of the Y type, but at higher voltages the Z-mode is observed which disappears at $E = E_3$. In the intermediate region corresponding to the extrapolation of branches 1 and 2 to lower frequencies the instability modes are transformed into each other and exotic convective structures are observed.

This "switching" of the modes is characterized by the change in the distortion wavelength, as is clearly seen from the theoretical threshold curve of Figure 49. The curve is plotted in terms of the stabilizing electric field E and reduced frequency $\omega_r = (\gamma_1 d^2/4K_1)2Hf$ for the Ericksen number Er = 70. It can be seen that while for the Y-mode the distortion wavelength almost does not change with increasing electric field, it grows for the Z-mode. These theoretical values of Λ_i agree well with experimental data. As an example, we compare the ratios of Λ_2/Λ_1 values at points 1, 2, and 3 for frequency f_0 (Figure 48):[82]

$$\left(\frac{\Lambda_2}{\Lambda_1}\right)^{\text{exp.}} = 1; \qquad \left(\frac{\Lambda_2}{\Lambda_1}\right)^{\text{theor.}} = 1.07;$$

$$\left(\frac{\Lambda_2}{\Lambda_1}\right)^{\text{exp.}} = 1; \qquad \left(\frac{\Lambda_2}{\Lambda_1}\right)^{\text{theor.}} = 0.88.$$

The theoretical and experimental results discussed above correspond to the frequency range where $\omega\tau \ll 1$; $\tau = \gamma^* d^2/K$ is the relaxation time for orientation fluctuations of wavelength d.

Consider threshold characteristics of instability at higher frequencies satisfying the condition $\omega\tau \gg 1$. We first assume that the elastic properties of the sample are isotropic and the stabilizing electric field is zero. We have then

$$f_y = f_z, \qquad \frac{T_y}{T_z} = \frac{\gamma_y}{\gamma_z}. \tag{95}$$

As is shown in Ref. 82,

$$\frac{T_y}{T_z} \simeq 1 + (\lambda_y - \lambda_z)\left(\frac{\tilde{q}_z}{\tilde{q}_x}\right)^2. \tag{96}$$

For MBBA at 25°C $\lambda_y = 1.35$ and $\lambda_z = 4.44$. Since $\lambda_y < \lambda_z$, it follows from (96) that $T_y < T_z$, and we may expect the onset of R-instability of the Y-type.

Expanding the expression (93) in powers of $(q_z/q_x)^2$, we obtain

$$\left(S^{\text{th}}(\omega)\right)^2 = \frac{f_y^2}{AB} - \frac{\omega^2\gamma_y^2}{AB}. \tag{97}$$

This condition can be expressed in terms of the Ericksen number

$$\mathrm{Er}^2(\omega) = \mathrm{Er}^2(0) + \omega^2\tau^2\left[1 + \tilde{\lambda}\left(\frac{\tilde{q}_z}{\tilde{q}_y}\right)^2\right] \tag{98}$$

where $\tilde{\lambda} = 2(\lambda_y + \lambda')$. Minimizing this function by $d\,\mathrm{Er}/dq_x(\omega) = 0$ and setting $q_z = \pi/d$, we find

$$q_x \sim (\omega\tau)^{1/3} \quad \text{and} \quad \mathrm{Er}^2 \sim \omega^2\tau^2. \tag{99}$$

Figure 49 shows that the experimental results (points) fit the theory.

The director makes an angle with the shearing plane. The case of an arbitrary angle between the director **n** and the velocity gradient is of most

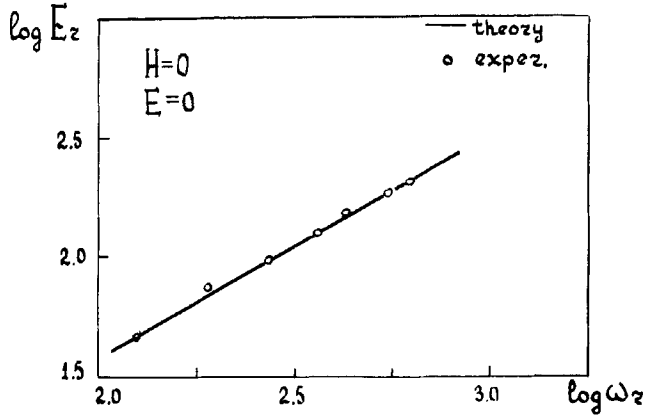

FIGURE 49 Relation between the Eriksen number and the reduced frequency $\omega_r = (\gamma_1 d^2/4K_1)\,\omega$. O—experimental results; —theory.

interest in the study of shear-induced molecular orientation, for precisely this situation is usually realized in practice. V. Reshetov[106–108] has recently considered the orientation instability of a nematic in an oscillating Couette flow for an arbitrary angle between **n** and **v**. Let us discuss the main results of this paper.

Suppose a nematic layer is bounded by planes $z = -d/2$ and $z = d/2$. The director **n** lies in the OXY plane and makes an angle ψ_0 with the flow direction (the OY axis). The flow velocity profile is of the form

$$v_x = 0; \qquad v_y = S(t)z; \qquad v_z = 0, \tag{100}$$

where $S(t)$ is the velocity gradient. Linearizing the Leslie-Ericksen-Parodi equations, we obtain the system of equations for deviations $\theta_1(t)$ and $\psi_1(t)$.[106]

$$\begin{aligned}\dot{\theta}_1(t) &= \left[a_\theta + b_\theta S(t)\right]\theta_1(t) + \left[a_{\theta\psi} + b_{\theta\psi}S(t)\right]\psi_1(t) = \beta_\theta S(t),\\ \dot{\psi}_1(t) &= \left[a_\psi + b_\psi S(t)|\psi_1(t) + \left[a_{\psi\theta} + b_{\psi\theta}S(t)\right]\theta_1(t) = \beta_\psi S(t).\end{aligned} \tag{101}$$

Here $\psi_1(t)$ is the angle between the tilted director position and the OXY plane; $\psi_1(t) = \psi(t) - \psi_0$, where $\psi(t)$ is the angle between $n(t)$ projected onto the OXY plane and the OY axis. The coefficients a_j, b_j, $\beta_{ji}a_{ij}$, and b_{ij} depend on K_i, α_i, ψ_0, and also the wave numbers q_x, q_z of the orientation distortion.

The method of solving this system is based on the fact that its exact analytic solution can be found for $S(t) = \text{const}$. Then for $S(t) = \text{sign}(\sin \omega t)$ the solutions are matched, so that the problem is reduced to finding the roots of the corresponding transcendental equation. Only the homogeneous system is considered, which has exponentially growing solutions for $S > S^{\text{th}}$. From the solvability condition for this system (the determinant is equal to zero) we find the value of S which corresponds to periodic solutions. For higher S, growing solutions appear, that is instability develops. The quantity S is a function of the fitting parameter q_x. Minimizing this function, one finds the value $S_{\min} = S^{\text{th}}$ and wave number $q_{x_{\text{opt}}}$ that correspond to this distortion.

We now analyse the behaviour of these parameters as a function of the oscillation frequency, layer thickness, angle ψ_0, and viscous and elastic coefficients. Curves 1–3 in Figures 50a and b show the dependences $S^{\text{th}}(\omega)$ (for $q_z = 10^3\ \text{cm}^{-1}$, $d = 30\ \mu\text{m}$) and $q_{x_{\text{opt}}}(\omega, q_z)$ for $\psi_0 = 0.1$, $\frac{3}{8}\pi$, and $\pi/2$ for MBBA. Normalization of the curves to q_z permits the comparison of the

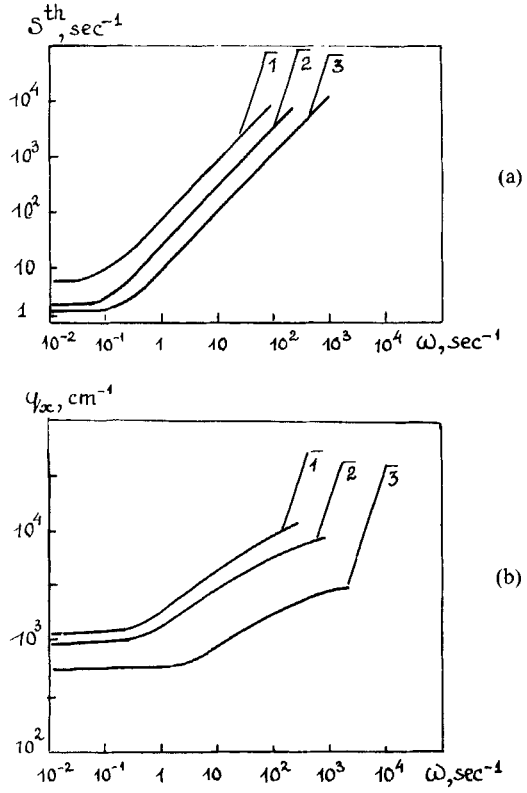

FIGURE 50 Frequency dependence of the threshold velocity gradient (a) and spatial-modulated structure wave number (b) in an MBBA sample for $q_z = 10^3$ cm^{-1}. The parameter ψ_0 takes the values 0.1, $3\pi/8$, and $\pi/2$ (curves 1 to 3).

data for different layer thicknesses. Depending on the angle between the director and flow velocity, we may consider the following cases.

1) If ψ_0 is close to $\pm\pi/2$, R-instability arises; it is similar to the Guyon-Pieranski instability† and has the following threshold characteristics

$$q_{x_{opt}} \sim (\omega q_z)^{1/3}, \qquad S^{th} \sim S_0 + A\omega. \tag{102}$$

2) As ψ_0 falls to a critical value $\psi_{0_{cr}}$, $q_x(\omega)$ slightly decreases and S^{th} increases, though the frequency dependence of these quantities does not change. In the region $\psi_0 > \psi_{0_{cr}}$ the parameter $q_{x_{opt}}(\omega)$ grows infinitely with

†As was already noted Guyon and Pieranski were the first to consider the case $\psi_0 = \pi/2$;[79,80] later, this case was analysed in detail by Dubois-Violette *et al.*[81]

ω, while for $\psi_0 < \psi_{0_{cr}}$ this parameter grows only to a certain limiting value $\tilde{q}_{x_{opt}}$ and then remains unchanged.

3) For ψ_0 close to 0 and π, $q_{x_{opt}} \sim q_z$ and does not depend on the oscillation frequency; in this case we also have $(S^{th})^2 \sim \omega^2/\sin^2\psi_0$.

It is worth noting that the dependence of $\psi_{0_{cr}}$ on the viscous coefficients α_i is rather complicated, the main contribution being due to α_3; as α_3 decreases from $+0.3P$ to $-0.5P$, $\psi_{0_{cr}}$ varies from $\pi/2$ to $\pi/4$ (for MBBA $\psi_{0_{cr}} \approx \pi/3$).

Let us compare the theoretical predictions with the results of model experiments[107] on 20–200 μm planar samples of the MBBA-EBBA mixture. The sample was placed between two plates, one of which was fixed and the other vibrated along the normal to the layer plane. Such a cell has free edges, so that compression makes the nematic spread over; in this case ψ_0 varies in the range $0 \leq \psi_0 < \pi/2$. The vibration frequency changed from 20 to 200 Hz.

Observations have shown that for this experimental geometry spatial-modulated structures arise in a certain range of ψ_0 values and are aligned along streamlines. Photographs in Figures 51a and b illustrate how the period of these structures depends on the angle ψ_0; layer thickness = 100 μm; f = 30 Hz; the values of ψ_0 are in the range 0–0.3 and 0.6–1.1 rad, respectively. As can be seen, the spatial period of these structures increases with decreasing ψ_0.

Experimental data are in good qualitative agreement with theoretical predictions. As an example, Figure 52 compares experimental values of $q_{x_{opt}}(\psi_0)$ (points) with the calculated ones; f = 20 Hz, layer thickness = 150 μm.

Propagation of light through such structures is the topic of Ref. 108, which also analyses the parameters of these structures considered as optical phase gratings. Development of R-instability means that the director tilts out of the layer plane ($\theta_1(t)$) and in the OXY plane ($\psi_1(t) = \psi(t) - \psi_0$). Thus, for a deformed sample we have

$$\begin{aligned} n_x(x, y, z, t) &= -\sin\psi_0 + \cos\psi_0\psi_1(t)\cos q_x x \cdot \cos q_z z, \\ n_y(x, y, z, t) &= \cos\psi_0 - \sin\psi_0\psi_1(t)\cos q_x x \cdot \cos q_z z, \\ \theta(x, y, z, t) &= \theta_1(t)\cos q_x x \cdot \cos q_z z, \\ \psi(x, y, z, t) &= \psi_0 + \psi_1(t)\cos q_x x \cdot \cos q_z z. \end{aligned} \tag{103}$$

The fluctuations of n_x, n_y, and n_z lead to the modulation of the refractive index along the X axis. For normal incidence of light polarized along **n** the refractive index is expressed as[105]

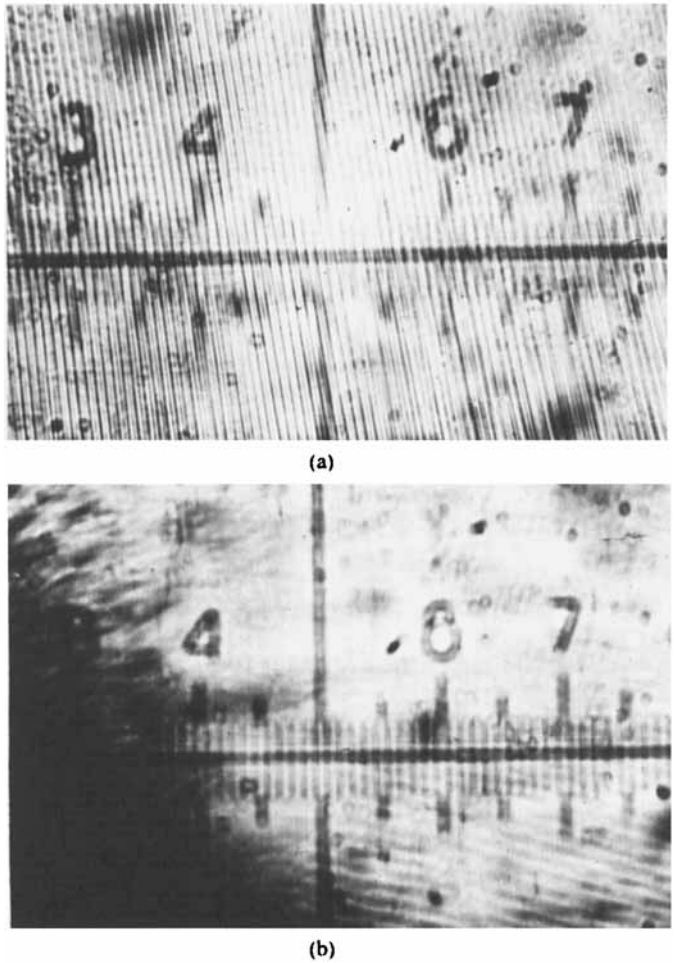

(a)

(b)

FIGURE 51 The spatial-modulated structure period as a function of the angle ψ_0; $d = 100$ μm; $f = 30$ Hz; (a) $\psi_0 = 0$–0.3; (b) $\psi_0 = 0.6$–1.1 rad.

$$n_{\text{ef}} = n_e + \frac{n_e(n_e - n_0)}{2n_0^2}(n_0 - n_e)\theta_1^2(t)\cos^2 q_z z \cos^2 q_x x. \qquad (104)$$

In this case the light wave passing through the layer is phase-modulated

$$A(x,t) = A_0 \exp\left[ik_0 \int_{-d/2}^{d/2} n_{\text{ef}}(x,z,t)\,dz. \right. \qquad (105)$$

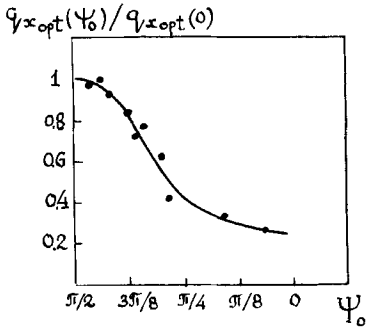

FIGURE 52 The wave number of spatial-modulated structures as a function of the angle ψ_0; MBBA; $d = 150$ μm; $f = 20$ Hz. The points are experimental values.

Taking into account (104), we have

$$A(x,t) = A_0 \exp(ik_0 n_e d) \exp\left[i\tilde{\phi}(t)\cos^2 q_x x\right], \tag{106}$$

where

$$\tilde{\phi}(t) = k_0 n_e \left(n_0^2 - n_e^2\right) d\theta_1^2(t)/4n_0^2.$$

Diffraction angles and intensities are of the form

$$\sin\psi_n = 2q_x/k_0, \qquad I_n = |A_0|^2 J_n(\tilde{\phi}/2). \tag{107}$$

In the case of oblique incidence the diffraction pattern is not only determined by the deviation $\theta_1(t)$, but also by $\psi_1(t)$. In this case there exist diffraction maxima at $\psi_n = q_x/k_0$, and the dependence $I_n(t)$ is modified.

Two types of phase gratings are possible:

$$\begin{aligned} \langle\psi_1(t)\rangle &= 0 \qquad \langle\psi_1(t)\rangle \neq 0 \\ \langle\theta_1(t)\rangle &\neq 0 \qquad \langle\theta_1(t)\rangle = 0. \end{aligned} \tag{108}$$

Depending on the grating type, diffraction pattern is either observed during the whole oscillation period or disappears when the corresponding director component vanishes. If the deformation exceeds the critical value, diffraction maxima disappear many times during one period, but brighter higher-order maxima appear.

The focal length of cylindrical lenses thus formed in the layer is given by the following expression[105]:

$$F = \left[\frac{n_e\left(n_0^2 - n_e^2\right) q_x^2\, d\theta_1^2(t)}{2n_0^2}\right]^{-1}. \tag{109}$$

Hence, varying the vibration frequency and the angle between the flow velocity and the director, one may control the period of an optical phase grating; the grating diffraction efficiency is determined by $S - S^{th}$; finally, varying the Leslie viscous coefficient and Frank elastic constants, and choosing the proper angle ψ_0, one may obtain different types of phase gratings.

B. Compression deformation

While analysing the behaviour of nematics in an oscillating Couette flow, we have discussed the model experiment at audible frequencies where compression of nematic in a cell with free edges resulted in periodic spreading of the layer.† This experiment is of special interest, for it reliably demonstrated the existence of two types of *R*-instabilities with different frequency dependence determined by the angle between the flow velocity and the director. We recall that $q_x \sim \pi/d(1 + \sqrt{\omega\tau})$ for $\psi_0 < \psi_{0_{cr}}$ and $q_x \sim \pi/d$ for $\psi_0 > \psi_{0_{cr}}$, where $\psi_{0_{cr}}$ depends on viscous-elastic characteristics of the material and may change from 0 to 90°. In both cases spatial-modulated structures are oriented along the streamlines.

In the high-frequency range, were $\lambda_{vis} \ll d$, an analysis of the director-flow interaction becomes much more complicated because of an irregular pattern of static acoustic flows caused by an inhomogeneous acoustic field in the layer. There are cases where the angle between the flow velocity and **n** varies in a wide range in different regions of the layer. Furthermore, the flow velocity profile may not be linear.

At present, experimental data on spatial-periodic distortion of planar structures under such conditions are rather scanty.[110,111] The data mainly refer to 10–90 μm MBBA-EBBA samples, frequencies 300 kHz–3 MHz, and temperatures 20–55 °C. Experiments were performed with configuration of Figure 1a; the wall of the cell facing the transducer was made of a thin lavsan film. The distortion pattern is shown in Figure 3a ($\mathbf{E} \perp \mathbf{n}$). It was found that the distortion spatial period Λ is proportional to d and does not depend on the vibration frequency, acoustic intensity, and temperature. Acoustic conditions in the layer were evaluated from acoustic intensity at the transducer surface. According to these data, the threshold acoustic intensity, at which a spatial-periodic distortion arises, does not depend on the layer thickness. For example, at 3.2 MHz J_s^{th} remained constant (44

†In this experiment the flow profile is somewhat different from the Couette profile; qualitative agreement between experimental data and theoretical results obtained for a flow with a linear velocity profile is explained by the fact that for parabolic velocity profile $v_y(z)$ instability develops in the boundary regions where the flow profile is of the Couette type. An analogy between these situations has been considered in detail by Manneville.[109]

W/cm^2) when the layer thickness varied from 10 to 90 μm.[110] However, because of the inhomogeneous acoustic field in the layer this value does not coincide with the actual threshold acoustic intensity.

I.3. Inhomogeneous distortion

In the previous sections we have compared experimental results with theoretical predictions. Unfortunately, such a comparison is impossible for the material presented in this section and below because it has not so far been interpreted theoretically. Nevertheless, experimental data now available are very useful for understanding the general picture of optical behaviour of nematics under various types of deformation.

This structure distortion in nematics was first observed at ultrasonic frequencies on a non-oriented *n*-azoxyphenetol subjected to compression.[84,85] It was found that disordered flows in the layer give rise to a polycrystalline structure with random director orientation which strongly scatters the incident light. By analogy with a similar phenomenon in an electric field, this effect is called acoustic dynamic scattering of light. Later, Kessler[112] measured the intensity of this scattering on a non-oriented VL 462 N nematic and found that the scattering intensity depended non-linearly on the voltage across the acoustic transducer ($d = 50$ μm, $f = 10$ MHz, compression deformation).

We now consider specific features of inhomogeneous distortion of nematics with different molecular orientation. In this case structure distortion is mainly caused by acoustic flows, so that the type of deformation and vibration frequency do not alter the qualitative picture of the phenomenon, but only determine the type of flow and its geometry. That is why we have decided to abandon in this section the previous scheme of exposition and classify substances only with respect to the initial structure.

I.3.1. Homeotropic orientation

One of the possible mechanisms of the formation of polycrystalline structures in a homeotropic nematic—via roll destruction—has recently been considered by Bertolotti *et al.*[93,102] Visual observations have shown that a regular roll pattern exists in a relatively narrow interval of acoustic intensities,[91,101] and even slightly above the threshold the pattern becomes unstable and is destroyed.[93,102] This transient process can be monitored by measuring the spatial coherence of the scattered light. If the acoustic intensity does not exceed the roll formation threshold, scattering is caused only by orientation fluctuations. Although this scattering is more intense than that in isotropic liquids, its intensity is lower than the values observed

at the roll formation threshold when the motion of anisotropic molecules gives rise to refractive index fluctuations which, in turn, initiate scattering.

Scattering in liquid crystals may be characterized by the correlation length of refractive index fluctuations: within this length an external field does not distort the ordered molecular orientation. The correlation length is related to the coherence length l of scattered light. Figure 53 shows the dependence of l in a 50 μm MBBA sample on the voltage across the acoustic transducer (compression deformation) for the stages of formation, stabilization, and destruction of rolls. Curves 1 and 2 correspond to the components $l_\perp$ and $l_\parallel$ along and perpendicular to the roll axes; the observation angle is 5°, f = 50 kHz, S is the linear dimension of the scattering volume. At the roll formation threshold, when the correlation length is small, the coherence length is also small. As rolls are stabilized and the velocity of particles in a vortex tube increases (at higher voltages across the acoustic transducer) the coherence length grows (increase in the correlation length with the flow velocity makes the behaviour of scattering centres correlated). The process lasts (according to visual observations) unless roll destruction begins. This stage is characterized by descending sections of curves 1 and 2; the correlation length drops to a rather small value, and the sample behaves as a thermal source containing a large number of statistically independent scattering centres. Variation of the sample thickness (100 and 200 μm) and observation angle (10 and 15°) does not modify significantly the picture just described, but makes it possible (via numerous observation data) to

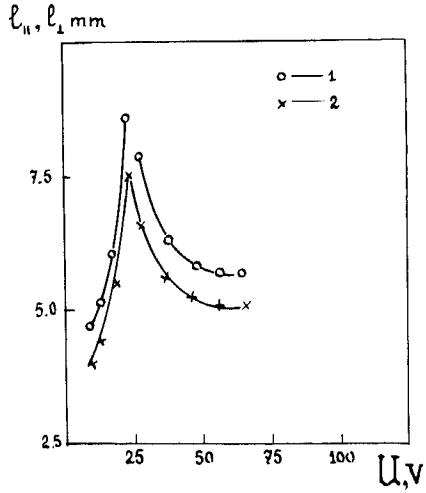

FIGURE 53 Correlation length of refractive index fluctuations along the roll axis ($l_\perp$) (curve 1) and normal to the axis ($l_\parallel$) (curve 2) vs. the transducer voltage; observation angle 5°; f = 50 kHz.

reveal certain general features of the phenomenon:

1) in the region of roll stabilization, with the increasing observation angle or decreasing layer thickness both $l_{\parallel}$ and $l_{\perp}$ grow;

2) for constant layer thickness and observation angle $l_{\parallel}$ always exceeds $l_{\perp}$. A theory, which relates variation of the correlation length of refractive index fluctuations to director field distortions, has not so far been developed. Experimental data show, however, that this parameter falls upon roll destruction.

A thorough qualitative study of the evolution and destruction of convective structures under elliptic shearing has recently been performed by Guazzelli.[100] According to her observations, at large values of the parameter N hexagonal structures are "melted", and in this "melt" square domains move independently with no significant ordering decrease within each domain. Thus, a small number of active centres may produce chaotic motion in the sample. As N increases, the size of the square domains decreases, and so does the whole area occupied by these domains. Finally, as N grows further, all ordered structures disappear, and a "fluctuating" polycrystalline structure arises. In recent years, the question has often been discussed of the possible interdependence between convective structure melting and two-dimensional ordering because the former process may be considered as the break of defect pair bonds at sufficiently high temperatures.[95,100,113]

It should be noted that a polycrystalline structure may be formed in another way: directly at the stage of homogeneous distortion as a result of the formation of disinclinations initiated by the motion of the medium. As the flow velocity increases, the disinclination density grows, so that a layer is eventually covered with a dense defect network.[29,114] The formation and annihilation of disinclinations is a reversible process.

The most complete information on the optical behaviour of nematics under inhomogeneous distortion has been obtained for compression deformation at ultrasonic frequencies. Figure 54a (curves 1–6) shows the relative intensity $I^{\theta_i}/I_0^{\theta_i}$ of light scattered by an MBBA layer along the normal to the layer and at angles 3, 6, 9, 12, and 15°, respectively, as a function of acoustic intensity (f = 3.2 MHz, the layer thickness = 40 μm). Here I^{θ_i} and $I_0^{\theta_i}$ are intensities of light scattered at an angle θ_i with and without sound. The data were obtained in experiments performed in configuration of Figure 1b.† They show that attenuated non-deflected beam ($\theta_i = 0$) and intensive side lobes are observed only at a certain threshold

†The experiments were performed with a source of monochromatic polarized light, but without polarizer in the detection system.

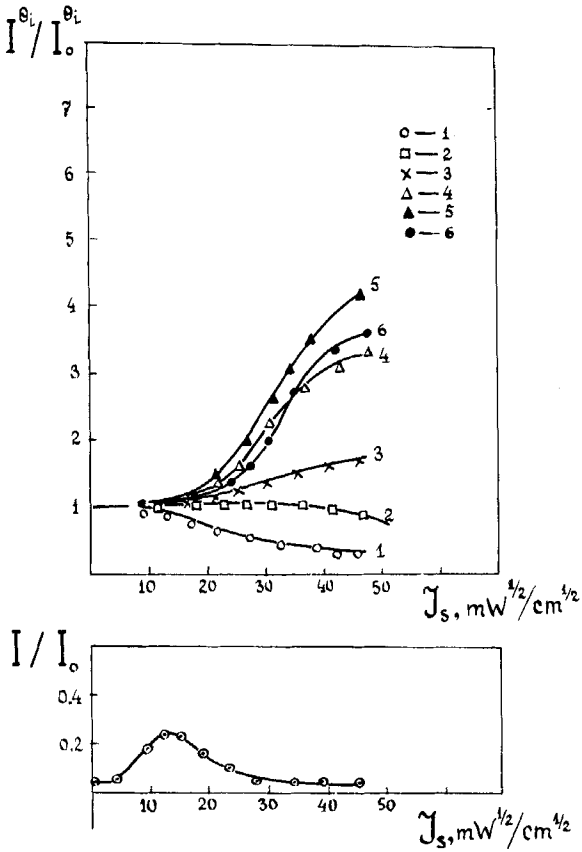

FIGURE 54 Relative intensity I^{θ}/I_0^{θ} of light scattered at 0, 3, 6, 9, 12, and 15° (a) and optical transmittance of monochromatic light at 0° (b) for different acoustic intensities J_s; $f = 3.2$ MHz; MBBA; $d = 40$ μm.

acoustic intensity $J_{s\,\mathrm{DSM}}^{\mathrm{th}}$ and approximately correspond to the beginning of the decay of sample optical transmittance measured in crossed polarizers (Figure 54b). As the acoustic intensity increases, a higher portion of the light is scattered at large angles.

It was found that as the layer thickness grows (10–90 μm), the general behaviour of the scattering curves does not change, but they become steeper and the threshold acoustic intensity drops. This is confirmed by curves 1–3 (Figure 55) which show the relative optical intensity $I^{\theta_i}/I_0^{\theta_i}$ as a function of acoustic intensity for 10, 40, and 80 μm MBBA samples (curves 1–3 and 1′–3′ correspond to the angles θ_i: 0 and 12°). It was obtained that $J_{s\,\mathrm{DSM}}^{\mathrm{th}} \sim 1/d^2$.

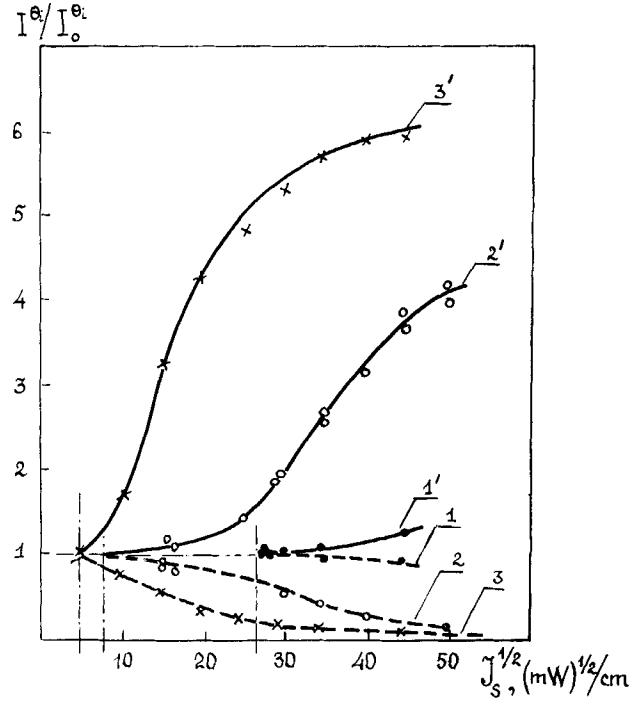

FIGURE 55 Relative intensity of light I^{θ}/I_0^{θ} scattered at 0 (curves 1–3) and 12° (curves 1′–3′) in 10, 40, and 90 μm samples for different acoustic intensities; MBBA; $f = 3.2$ MHz.

The ultimate values of the attenuation of the non-deflected beam due to light scattering, $\tilde{k}_0$† depend on the acoustic intensity. These data are shown in Figure 56 for 10, 40, 60, and 80 μm samples of a MBBA-EBBA mixture (items 1–4). The vibration frequency was 3.2 MHz. The values of J_s are normalized to the threshold acoustic intensity $J_{s_{\text{DSM}}}^{\text{th}}$ for a given sample. It can easily be seen that for the layer thickness indicated in the figure the coefficient $\tilde{k}_0$ is determined by the difference between J_s and the threshold $J_{s_{\text{DSM}}}^{\text{th}}$.

In experiments with a 40 μm sample of the MBBA-EBBA mixture at 331 and 981 kHz (compression deformation) we have found that the threshold falls approximately as $1/f$ with increasing vibration frequency. Our data agree well with data of Bruchmüller on the dynamic behaviour of nematics under shear deformation.[18] Curves 1–9 in Figure 57 show how the phase

†The meaning of this coefficient becomes clear if the transient process is approximated by the expression $\tilde{k} = \tilde{k}_0(1 - e^{-t/\tau_1})$, where $\tilde{k} = 1 - I/I_0$, τ_1 is the response time.

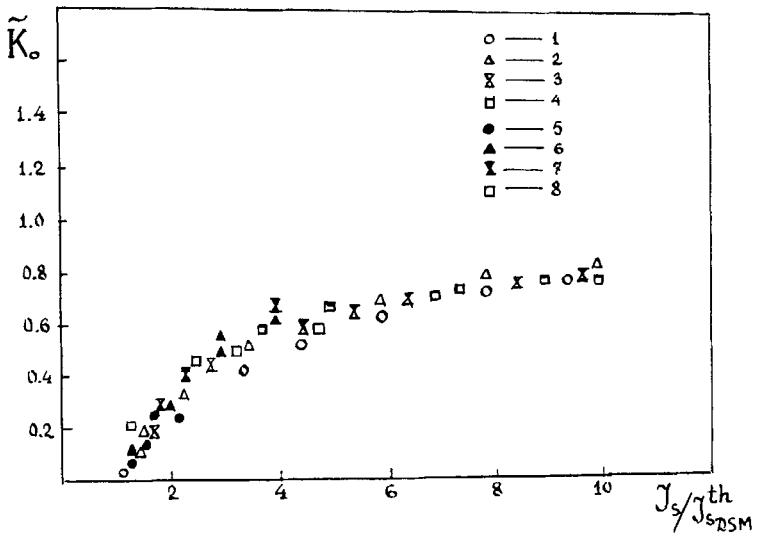

FIGURE 56 Maximal attenuation coefficient of the non-deflected beam in 10, 40, 60, and 80 μm MBBA-EBBA samples (1–4); f = 3.2 MHz.

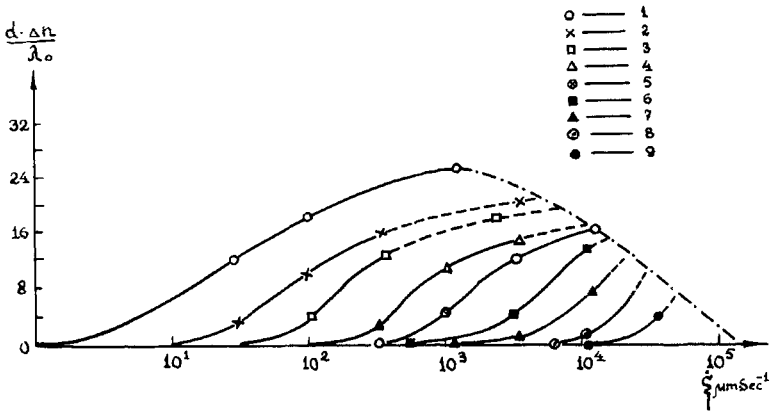

FIGURE 57 Dynamical behaviour of an MBBA sample under shearing; d = 55 μm; shearing frequency is the parameter from 0 to 300 Hz (curves 1 to 9).

delay between the ordinary and extraordinary rays in a 55 μm MBBA sample (reduced to the light wavelength $\lambda_0 = 632.8$ nm) varies with the rising shear rate; the shear frequency is a parameter and takes the values: 0, 0.1, 0.3, 1, 3, 10, 30, 100, and 300 Hz. The dashed curve bounds the region where the effective dynamic scattering can be observed. As the vibration frequency grows, the boundary shifts to higher shear rates, but smaller vibration amplitudes ξ_0. According to these data the threshold amplitude $\xi^{th}_{0_{DSM}} \simeq J^{-0.7}$ and amounts to $1.86 \cdot 10^{-3}$ cm at 300 Hz; at low ultrasonic frequencies $\xi^{th}_{0_{DSM}}$ decreases. For example, according to Bruchmüller data, the threshold amplitude is $7.5 \cdot 10^{-5}$ at 21 kHz,[18] but the above empirical relation between $\xi^{th}_{0_{DSM}}$ and f remains valid.

I.3.2. Planar orientation

The physical reason for dynamic light scattering observed in planar nematic samples is exactly the same as in homeotropic samples: namely, a structure with random director orientation produced by acoustic flows at a certain sound intensity. In this case, however, the angular distribution of the scattered light intensity depends on the observation point. This is clearly seen from Figure 58 referring to a 40 μm sample of the MBBA-EBBA mixture at 3.2 MHz (compression deformation).[110,115] Here families *A* and *B* of the curves of light flux relative intensity along the direction θ_i versus acoustic intensity differ only by the azimuthal angle ψ: $\pi/2$ and 0, respectively.† Curves 1–6 correspond to θ_i values 0, 3, 6, 9, 12, and 15°, respectively. The incident light is polarized normal to the director. It can be seen that at $\psi = \pi/2$ the non-deflected beam ($\theta_i = 0$) is attenuated with increasing acoustic intensity, while the relative intensity of the side lobes grows. On the contrary, at $\psi = 0$ both the non-deflected beam and the side lobes are attenuated.

This distinction is clearly manifested in the behaviour of the scattering indicatrices for $\psi = 0$ and $\psi = \pi/2$ shown in Figure 59 for the case of $\mathbf{n} \perp \mathbf{E}$ (I_0 is the intensity of incident light). Curves 1 and 2 are the scattering indicatrices for zero acoustic intensity and for $J_s = 2.2$ W/cm^2, respectively ($f = 3.2$ MHz). These data show that for $\mathbf{n} \perp \mathbf{E}$ the intensity of side lobes is significant in the plane containing the director and normal to the layer (the *XZ*-plane $\psi = \pi/2$), while for $\mathbf{n} \| \mathbf{E}$ the side lobes are more intensive in the *YZ* plane ($\psi = 0$).

Another qualitative feature of the optical behaviour of planar nematic samples under compression deformation at high frequencies is that the

†The azimuthal angle ψ is the angle between the *X* axis and the projection of the radius-vector **R** connecting the observation point *M* with the origin in the *XY* plane (the layer plane).

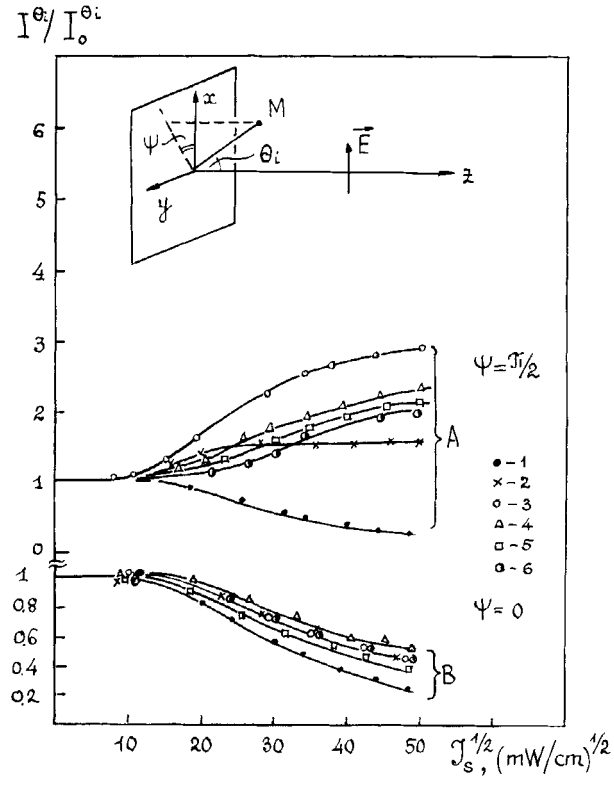

FIGURE 58 Angular distribution of scattered intensity for a 40 μm MBBA-EBBA sample at 3.2 MHz. Families *A* and *B* correspond to azimuthal angles $\psi = \pi/2$ and 0. Curves 1–6 correspond to θ_i values from 0 to 15°.

threshold $J_{s_{\text{PSM}}}^{\text{th}}$ does not depend on the layer thickness. This is confirmed by the data obtained at 3.2 MHz on MBBA-EBBA samples of different thickness (from 10 to 80 μm).[110]

The maximal attenuation coefficient $\tilde{k}_0$ of the non-deflected beam depends on acoustic intensity, and, if the layer thickness varies, it also depends on to what extent J_s exceeds the threshold. These data are shown in Figure 56 (notation 5–8) for the following *d* values: 10, 40, 60, and 80 μm (f = 3.2 MHz).[115]

We note in conclusion that the stage of inhomogeneous distortion has been studied least of all both as regard the mechanism of the phenomenon (the origin and dynamics of flows responsible for orientation turbulization) and as regard the connection between the characteristics of scattered light and the optical properties and parameters of scattering centres (concentration, size distribution). This connection can be found by the methods of the

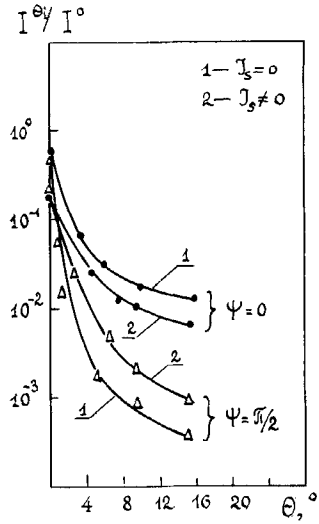

FIGURE 59 Scattering indicatrices with and without sound (curves 2 and 1) at $\psi = \pi/2$ and $\psi = 0$; $\mathbf{n} \perp \mathbf{E}$.

optics of light-scattering media,[116] and informative correlation methods enable one, by analysing statistical properties of the scattered light, to establish some characteristics of the motion of the medium under mechanical deformation. Quite a promising approach is to describe the effect of dynamic light scattering by a model in which scattering is considered as diffraction of light from a large number of particles of different diameter.

I.4. Acoustic "guest-host" effect

We have seen in the previous sections that the influence of periodic compression or shearing on the structure of nematics (and hence on their optical properties) is manifested quite differently. As a result of deformation, a light beam passing through a layer may change the polarization, may be diffracted on domains, or may be scattered from fluctuations of the local director orientation.

We now discuss another interesting phenomenon: spectral-selective absorption of light in nematics containing a pleochroic dye. It has long been known that nematics can orient foreign molecules. If these molecules are of elongated shape, their long axis is oriented along the director.† Orientation of dye molecules gives rise to optical absorption dichroism in the visible

†Here we mean a time-averaged preferred orientation because in a liquid crystal impurity molecules experience rotational motion.

spectral region, which may be either positive ($D_{\parallel} > D_{\perp}$) or negative ($D_{\parallel} \ll D_{\perp}$), depending on the orientation of the dipole transition oscillator relative to the nematic molecular long axis (Figure 60) ($D_{\parallel}$ and $D_{\perp}$ are optical densities of the solution when the polarization vector of the light is parallel or perpendicular to the nematic director).

If the dye concentration in the solution is not very high (not more than 1–2%), most of the physical properties of the crystal (phase transition points, viscous-elastic properties, dielectric constants, refractive indices) remain unchanged. This means that in the presence of a "guest" the "host" retains its unique capabilities of responding quite definitely to an external action, but exhibits an absorption band in the visible spectral region. For most dyes the absorption oscillator is parallel to the long molecular axis, so that light polarized parallel to the preferred molecular orientation is absorbed more intensely.

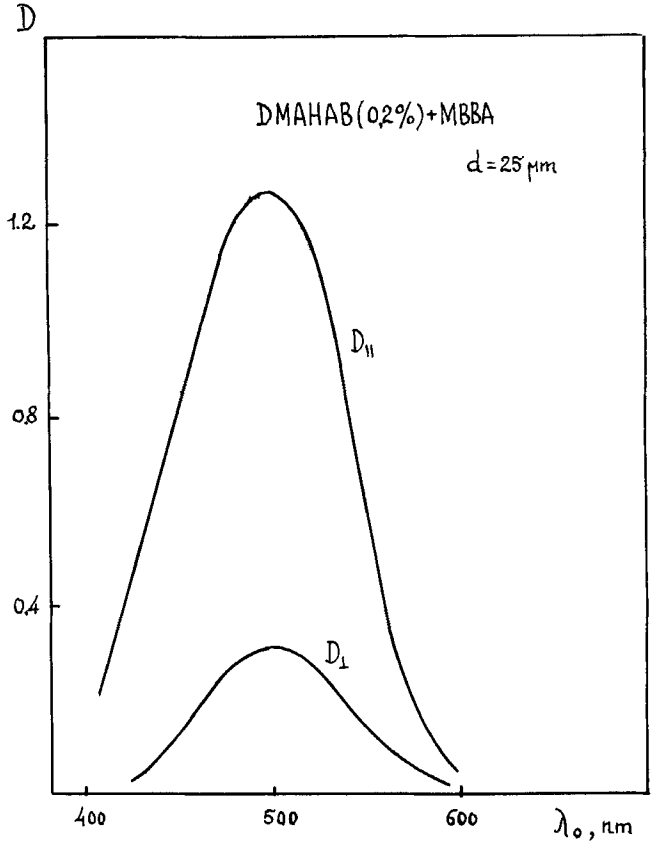

FIGURE 60 Optical absorption dichroism.

Consider a sample of a homeotropically oriented impurity nematic. In the initial state its optical density does not depend on light polarization. When the sample structure is distorted and the director is tilted, thereby entraining dye molecules, the optical density turns out to be different for light polarized along and perpendicular to the director. Thus, the higher the director tilt, the larger is the change in the optical density $D_{\parallel}$.

This is confirmed by experiments on impurity nematics subjected to periodic compression ($f = 331$ and 982 kHz).[117] A fluorescent dye with positive dichroism ($D_{\parallel} = 0.6$; $D_{\perp} = 0.225$; the dichroic ratio $N = D_{\parallel}/D_{\perp} = 2.67$) was introduced into homeotropically oriented nematic samples with $\Delta\epsilon < 0$.[118] This dye has three absorption bands with maxima at 295, 340, and 510 nm, and also a luminescence band at 600 nm. The spectral properties of this dye (dissolved in toluene) for one of the absorption bands and for the luminescence band are shown in Figure 61 (curves 1 and 2). Here $\epsilon' = D/c'd$ is the extinction coefficient, c' is the dye concentration in the solution. Figure 62 illustrates the variation of the optical density in a 40 μm MBBA-EBBA sample with 0.5% of the dye with the increasing wavelength of light (the vibration amplitude range is 2.5 times). The data were obtained in non-polarized light at wavelengths 450, 500 and 650 nm. It can be seen that the extremum of the function $\Delta D_{\text{rel}}(\lambda_0)$ coincides with the absorption maximum in the band considered.

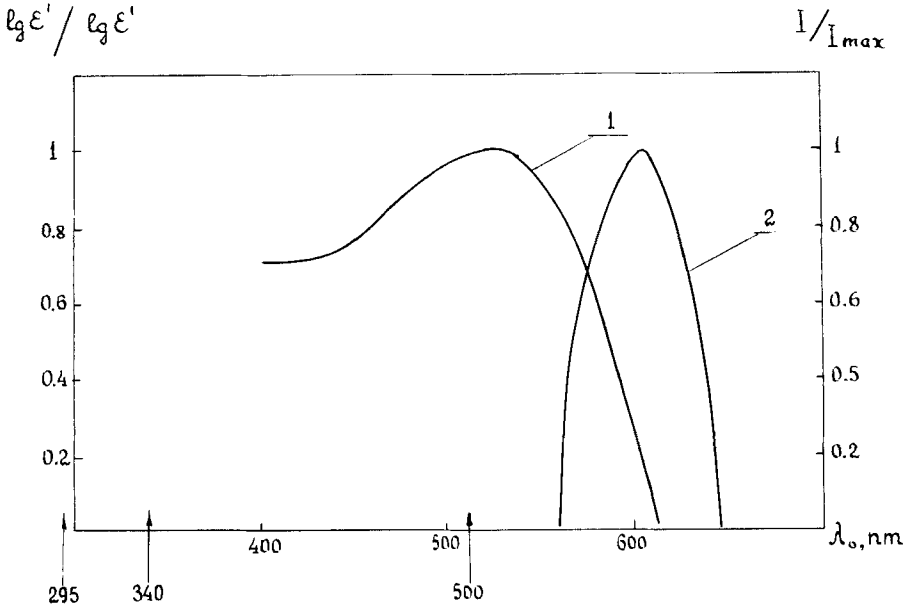

FIGURE 61 Spectral properties of a fluorescent dye dissolved in toluene in one of the absorption bands (curve 1) and in the luminescence band (curve 2).

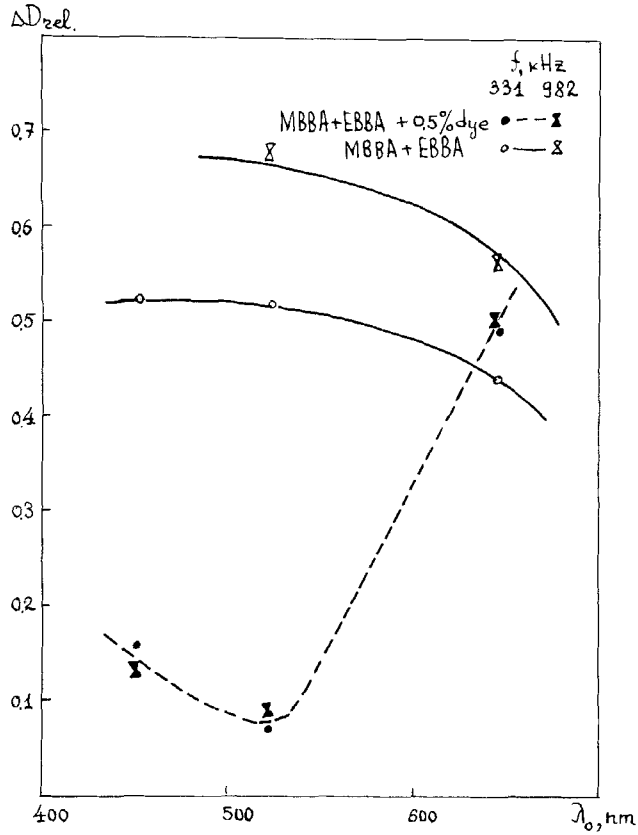

FIGURE 62 Optical density of an MBBA-EBBA mixture with 0.5% of a dye as a function of wavelength of light; $d = 40\ \mu m$.

II. ACOUSTOOPTICAL EFFECTS IN CHOLESTERIC LIQUID CRYSTALS

Deformation may influence the structure and optical properties of cholesteric crystals quite differently, depending both on the direction in which the deformation is applied and on the experimental geometry (cell dimensions, the initial cholesteric texture, etc.). Structural modifications which lead to the most interesting and important (in view of practical application) acoustooptical effects can be divided into two main groups:

1) the effects caused by the change in the helical pitch;

2) the effects caused by texture modification.

The theory which describes how a cholesteric responds to a periodic deformation has not so far been developed, that is why these effects have to be interpreted proceeding from experimental results alone.

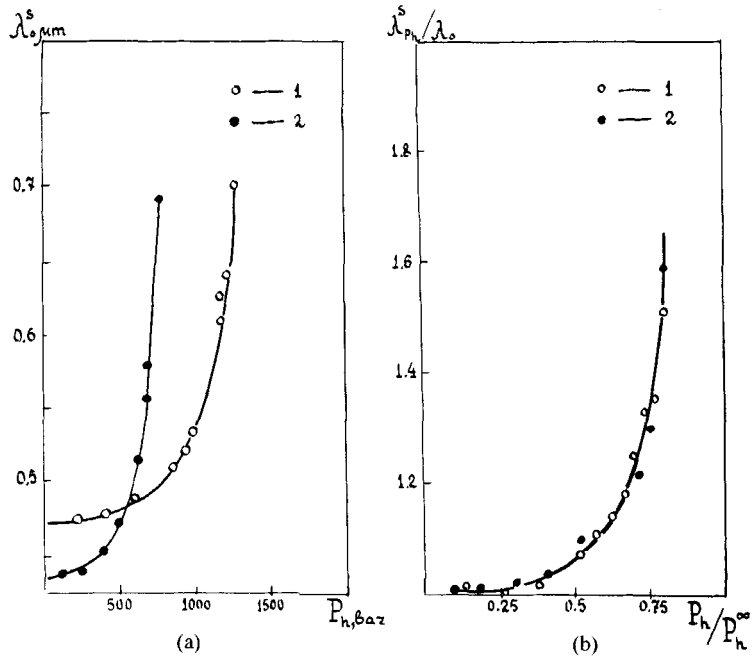

FIGURE 63 Effect of pressure on the selective reflection wavelength (a) and relative change in the selective reflection wavelength (b) for the mixtures: (1) cholesteryl oleyl carbonate (74.8 mol.%) + cholesteryl chloride (22.2 mol.%); (2) cholesteryl oleyl carbonate (80.1 mol.%) + cholesteryl chloride (19.9 mol.%).

II.1. Helix distortion

The effect of mechanical deformation of a cholesteric on the wavelength of selective reflection of light was discovered independently by A. Kapustin (compression experiments; non-oriented samples of cholesteryl caprinate, cholesteryl chloride, and their mixtures)[119] and J. Fergason (shear experiments).[120] Later, this effect was observed for different deformations on planar samples which, as is known, possess greater lability with respect to structure imperfection, temperature, chemical composition, etc.

A. Compression deformation

Pollmann and Stegemeyer[121] studied the behaviour of a planar sample of the mixture of cholesteryl carbonate and cholesteryl chloride (two concentration values) under hydrostatic pressure P_h and found that only high pressures affect noticeably the selective reflection wavelength λ^s_0 (Figure

63a).† As can be seen, λ^s_0 increases with pressure, tending to infinity. This implies that the helical pitch grows, though it might be expected at first sight that the pitch should decrease with increasing pressure because of the approach of molecules. This effect[122] is, however, of no significance in cholesterics. If we assume that the compressibility of typical cholesterics is of the same order as that of nematics ($\sim 6 \cdot 10^{-5}$ bar^{-1}), then at a pressure of 1000 bar the "blue" shift is only 10 nm,[121] while the red shift caused by the structural factors prevails. These factors may be taken into account via the effective viscosity η_{ef} introduced by Böttcher;[123] it is related to hydrostatic pressure by

$$\eta_{P_h} = \tilde{\eta}_{P_h} \exp(A \cdot P_h), \tag{110}$$

where $\tilde{\eta}_{P_h}$ is the viscosity at 1 bar, and A is a parameter. The expression for the relative change in the selective reflection wavelength due to pressure can, therefore, be written in the form

$$\lambda^s_{P_h}/\lambda^s_0 = \left[1 - \left(C\tilde{\eta}_{P_h}\right)^{1 - P_h/P_h^\infty}\right]^{-1}, \tag{111}$$

where $\lambda^s_{P_h}$ is the selective reflection wavelength at pressure P_h, C is a constant dependent only on the molecular parameters, P_h^∞ is "infinite" pressure at which $\lambda^s_{P_h} \to \infty$. Figure 63b presents the theoretical dependence of $\lambda^s_{P_h}/\lambda^s_0$ versus P_h as calculated from this relation for cholesteryl oleyl carbonate/cholesteryl chloride mixtures with composition 74.8–25.2 mol.% (P_h^∞ = 1500 bar) and 80.1–19.9 mol.% (P_h^∞ = 900 bar); $C\tilde{\eta}_{P_h} = 0.00145$. This dependence agrees with the experimental data of Figure 63a.

The change in the selective reflection wavelength with pressure can also be explained by a phase transition of a cholesteric at $P_h = P_h^\infty$ into a high-density mesophase in which all the molecules are aligned parallel.[124] This gradual transition from a twisted conformation to nematic order also leads to a sharp rise in the helical pitch and, therefore, to increased selective reflection wavelengths.

Another approach to explaining the peculiarities of selective reflection in planar samples of cholesteric mixtures under compression and extension of a layer parallel to the helical axis was suggested by Bartolino and Scaramuzza.[125,126] Using the expression for free energy, which allows for the effect of deformation on a system of layers and a single layer (the latter is similar to the case of a nematic), they showed that for $\xi_0/d \ll 1$ and

†For these cholesterics the selective reflection wavelength does not depend on temperature.

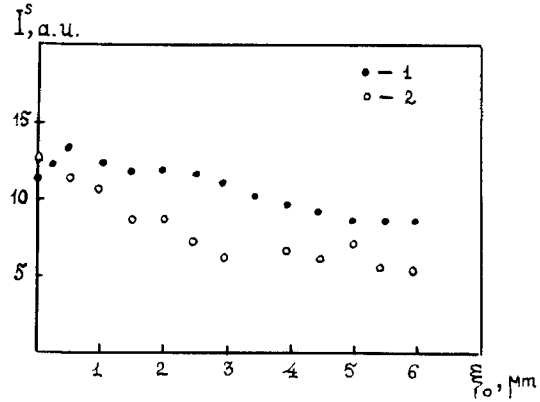

FIGURE 64 The behaviour of reflected light intensity for a 75 μm planar sample of a cholesteric mixture under compression and tension (1 and 2, respectively).

$P_0 \ll 1$ the relative change in the helical pitch $\Delta P_0/P_0 = \xi_0/d$. (Here ξ_0 is the displacement of one of the substrates.) Experiments† have shown, however, that the selective reflection parameters (bandwidth $\Delta\lambda^s$, wavelength λ^s_0, peak intensity) behave differently with respect to the deformation phase and magnitude. For compression of small magnitude ($\xi_0 \sim P_0$) the selective reflection wavelength λ^s_0 shifts to shorter wavelengths, and the change in λ^s_0 is proportional to the deformation. When $\xi_0 > P_0$ and increases further, λ^s_0 shifts to longer wavelengths.

In the extension phase the selective reflection wavelength grows linearly up to $\xi_0 \sim 3P_0$ and then remains virtually unchanged.

Figure 64 shows how the intensity of the reflected light varies with the compression and extension of a 75 μm sample (curves 1 and 2). The reflection bandwidth $\Delta\lambda^s$ almost does not change in the region of linear cholesteric behaviour and decreases, irrespective of the deformation phase, for large ξ_0 values; in the latter case there is a small rise of $\Delta\lambda^s$ for $\xi_0 \simeq 2$ μm.

Deviation from the linear behaviour (predicted by the theory) in the compression phase can be explained if we assume that the helical pitch in the layer has a vertical gradient ∇P_0 which grows with deformation. Mazkedian *et al.*[127] have shown that as the gradient exceeds a critical value, the optical properties of a cholesteric vary (the selective reflection bandwidth grows and shifts to greater wavelengths, and the peak intensity of selective reflection falls). According to Mazkedian's estimates, this effect becomes significant provided $\Delta P_0/P_0 = (\Delta n/n)^2$. Putting $n \sim 1.5$ and

†These experiments were carried out with temperature-insensitive cholesteric mixtures invented in Orsay.

$\Delta n \sim 0.2$, we find $\Delta P_0/P_0 \sim 10^{-2}$, in agreement with experimental data for the compression phase where deviation from the linear behaviour was observed for $\xi_0 \sim P_0$. Essentially, the behaviour of all the parameters of selective reflection agrees qualitatively with the predictions of this model.

One of the possible explanations of the deviation from linearity in the compression phase is as follows: stress relaxation gives rise to "defect climb" and local formation of additional layers,† so that no helical pitch gradient arises in the sample.

Undoubtedly, all these investigations have revealed that the texture state does depend on the static deformation (compression or extension) and seem to have given a clue to understanding the reasons for the change in selective reflection under these conditions. The results obtained in the work of Chuvyrov specially devoted to studying the effect of periodic deformation on the spectrum of a planar sample in the selective reflection range (400–450 nm) also confirm helix deformation. The change of this portion of the spectrum observed in his experiments (a positive peak at 436 nm and a negative peak at 425 nm) can only be attributed to the modulation of the reflected light amplitude. The experiments were performed with 10–15 μm samples in the configuration of Figure 1a at 600 kHz.

B. Shear deformation

As was already pointed out, the effect of shear deformation on selective reflection was discovered by Fergason who, however, did not explain the mechanism of the phenomenon. Subsequent works specially devoted to studying the effect of shearing on selective reflection[129–135] gave contradicting and non-reproducible results. All these workers used a rather simple experimental technique: a thin cholesteric layer was placed between two transparent plates (or plates containing transparent windows),[131–135] one of which was fixed and the other rotated at a constant speed. Since accurate measurement of shear deformation under such conditions encounters considerable difficulties, the change in the wavelength and intensity of selective reflection was compared with the rotational speed.

According to Ref. 130, the selective reflection wavelength shifts to longer wavelengths only for small shear stresses σ_{sh} (0–3 g/cm^2), as σ_{sh} increases, λ^s_0 shifts to shorter wavelengths, and for $\sigma_{sh} > 10$ g/cm^2 λ^s_0 remains unchanged. Since these experiments were performed with a mixture‡ for which the selective reflection wavelength is virtually temperature independent,

†The role of defects for stress relaxation was pointed out by Bartolino and Durand who studied the behaviour of a sample SmA subjected to extension.[128]

‡60% cholesteryl pelargonate, 26.75% cholesteryl chloride, 8.25% cholesteryl benzoate, 5% cholesteryl oleyl carbonate.

these contradicting results cannot be explained by the rise of the sample temperature due to shearing.

The results of more recent work[132] have shown that the selective reflection wavelength practically does not depend on shear deformation. A small shift of λ^s_0 to shorter wavelengths the authors of this work attribute to an increased contribution of deformed layers to scattering. References 133, 134 share the same point of view. As one moves in the sample from the fixed plate to the rotating one, the cholesteric helix experiences greater bending. This leads to the change in the reflection angle and, according to the Wulff-Bragg law, to the shift of the selective reflection wavelength to shorter wavelengths. The main contribution to reflection is due to the lower non-deformed layers; precisely these layers determine the wavelength of the principal reflection peak. The role of the deformed regions is less significant; they broaden the reflection peak and reduce its intensity, as is clearly seen from curves 1 and 2 of Figure 65 which correspond to a non-deformed planar structure and to its state when one of the plates rotates at a speed of 1 cm min^{-1}.[132] These data were obtained with the mixture: 23% cholesteryl pelargonate, 44.5% cholesteryl oleyl carbonate, 32.5% cholesteryl chloride (the layer thickness = 250 μm).

It was also found in these experiments that the reflected intensity is inversely proportional to the angular rotational speed and can be described by the following empirical relation[132]:

$$I^s/I_0 = -0.35 \log \omega - 0.21, \tag{112}$$

where I^s is the intensity of the reflected light for a given rotational speed, I_0 is the reflected intensity in the non-deformed state, ω is the angular rotational speed of the plate (rpm). It should be noted however that another team of experimenters[133,134] found no simple relationship between the reflected intensity and the rotational speed.

As the sample thickness and the plate rotational speed increase, the intensity of the reflected light drops. Curves 1–3 of Figure 66a correspond to 5, 25, and 125 μm thick samples of the mixture 23% cholesteryl pelargonate, 44.5% cholesteryl oleyl carbonate, 32.5% cholesteryl chloride. In this figure reflection is estimated as the ratio of the areas under the selective reflection curves recorded for a given shearing speed and without shearing. As can be seen, for low shearing speeds (not more than 20 cm/min) the reflected intensity changes little; for higher shearing speeds the change becomes noticeable. With respect to the layer thickness, the change in the reflected intensity is little, but quite distinct.

Essentially, the increase of the plate rotational speed leads to spectral variation of the reflected light. For example, according to Ref. 132, the thinner the sample, the wider is the spectral range of reflected light (see

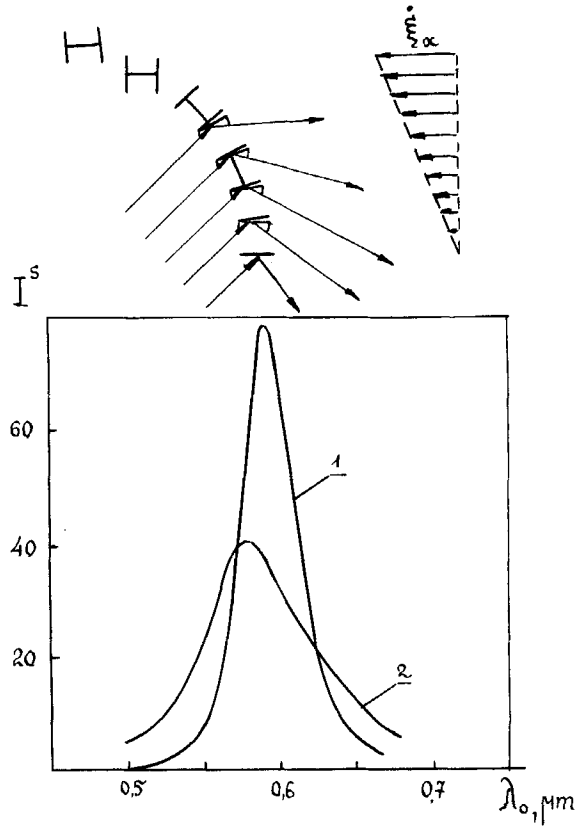

FIGURE 65 Effect of shear deformation on selective reflection: (1) unperturbed planar structure; (2) rotation of the substrate at 1 cm/min; $d = 250$ μm.

Figure 66b; notations I, II, and III correspond to sample thickness 50, 125, and 250 μm). This result agrees with the model that non-deformed layers adjacent to the fixed plate contribute mainly to the reflection. Figure 66b also shows that for all sample thicknesses the shift of the selective reflection wavelength is more pronounced in the short-wavelength region (the so-called "blue shift"), and this "blue shift" depends significantly on the sample thickness.

Shear deformation of samples† with helical pitch comparable with the wavelength of light also leads to a change in the selective reflection intensity, but at much higher shearing speeds (~ 172 rps).[135]

†The mixture of MBBA (nematic) and cholesteryl oleyl carbonate (cholesteric).

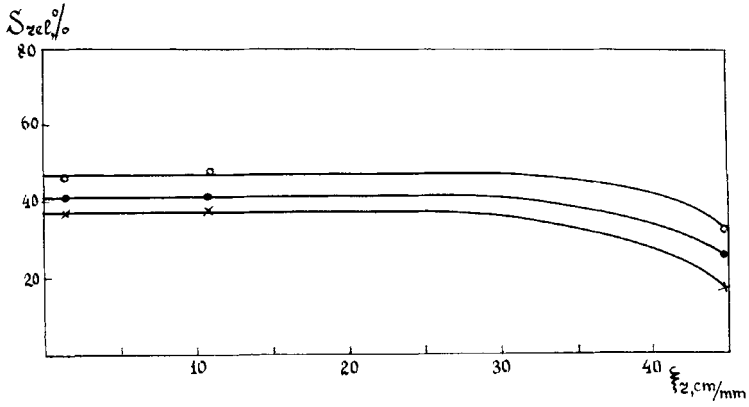

(a)

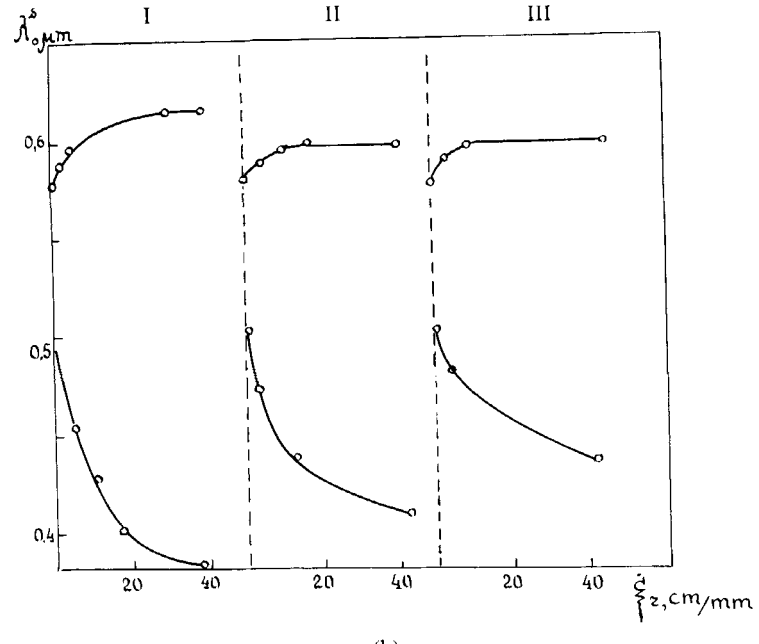

(b)

FIGURE 66 Effect of the rotation speed of the substrate on the relative area under selective reflection curves (a) and on selective reflection spectral limits (b) for 5, 25, and 125 μm cholesteric samples (notations I, II, III).

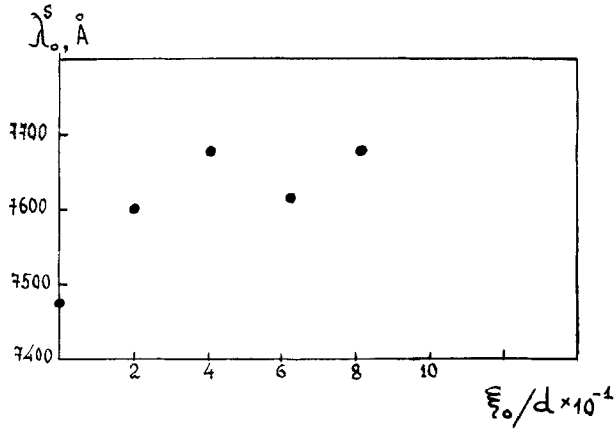

FIGURE 67 Hysteresis in a 75 μm planar cholesteric sample under compression-tension deformation.

These experimental results correlate well with the above model which allows for the change in the reflection angle as one moves from the fixed plate to the rotating one.

In conclusion, we point out that there is a time delay in the restoration of the initial reflected intensity after deformation ceases. With shear deformation, the relative intensity grows linearly with time t, but depends on temperature. For example, at $T = 34°C$ this dependence is described by the empirical relation

$$I^s/I_0 = 0.187 \log t + 0.21. \tag{113}$$

Hysteresis in a planar cholesteric sample under compression-tension deformation is illustrated in Figure 67 which shows selective reflection peaks immediately after perturbation ceasing in a 75 μm sample for different deformation levels.

II.2. Effects caused by texture modification

Thus far, we have concentrated on the effect of mechanical deformation on selective reflection. However, this deformation is also the cause of structural transformations. We now consider the effects caused by these transformations in greater detail and classify them with respect to the type of the initial texture and deformation.

II.2.1. Planar texture

A. Shear deformation

Homogeneous distortion of the cholesteric planar texture under shear deformation, when the director remains unchanged in the planes perpendic-

ular to the non-deformed helical axis and changes only along this axis, has been considered by many authors within the framework of the continuum model. Leslie[136] has derived the fundamental differential equation and obtained an analytic solution for large gradients when the shear is perpendicular to the helical axis. In our opinion, two of the results obtained by Leslie are of major importance: 1) the apparent viscosity η_{ap} depends on sample thickness, helical pitch, and velocity gradient; 2) at large velocity gradients η_{ap} tends to a value independent of the gradient. The effect of velocity gradient on the apparent viscosity (for the same geometry) was analysed in detail by Kini.[137] It was found that for very small gradient η_{ap} depends only on helical pitch and sample thickness. As P_0 increases, the viscosity first oscillates (the oscillation amplitude growing on P_0 approaching d) and then gradually decreases. For constant P_0 and d the viscosity drops with the increasing velocity gradient, the smaller P_0 the larger is the velocity gradient at which this change occurs. As an example, Figure 68 shows the data of Kini on the variation of η_{ap} in a 50 μm sample for the following P_0 values: 70, 10, 41, and ∞. The dashed horizontal line is η_{ap} for $P_0 = 0$ (here $\dot{\xi}$ is the speed of one of the substrates). Interesting results have also been obtained in the work of J. Prost[138] dealing with shear-induced flexoelectric polarization of cholesterics. His experiments have shown that owing to a peculiar structure (for example, the absence of mirror symmetry) cholesterics may not only exhibit a much wider manifestation of the effect

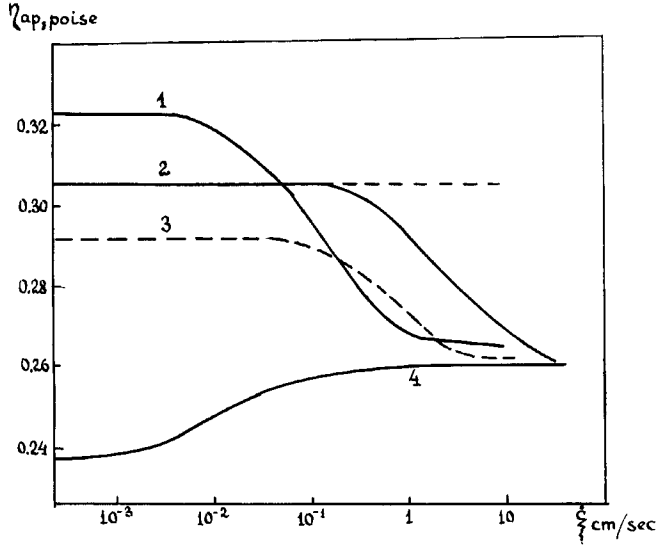

FIGURE 68 The behaviour of apparent viscosity in a 50 μm planar cholesteric sample for the helical pitch values $P_0 = 70$, 10, 41, and ∞.

of deformation on their structure, and therefore on optical properties, but also new phenomena that are not typical of nematics.

L. Bata and I. Janossy have recently observed in cholesterics a specific type of instability, "propagating" domains.[139,140] They have interpreted the effect, using the familiar method of analysing field instabilities developed in Ref. 141. L. Bata and I. Janossy considered a small periodic distortion of cholesteric planes in a sample and studied the effect of shearing on this perturbation. Suppose the perturbation is given in the form

$$\phi = \phi_0(z)\sin kx, \tag{114}$$

where the axis x is perpendicular to the shearing direction. To find the instability threshold we consider, as usual, the balance equation for the torques. Calculation shows, however, that the shear-induced viscous destabilizing moment and elastic moment are phase-shifted by a quarter of the perturbation period.[140] This means that these moments cannot be in static equilibrium, and it remains to assume that the spatial perturbation phase (114) changes with time, i.e. deformation propagates along the axis Ox at the velocity†

$$v_d = \frac{\omega_d}{k} = \frac{SP_0}{4\pi}. \tag{115}$$

An analysis has shown that the relationship between these quantities does not depend on how the spatial-periodic layer distortion is produced, so that relation (115) is also valid in the presence of an external field.

The viscous torque does not only make the perturbation propagate, but also enhances it, provided the velocity gradient S attains the threshold value

$$S^{\text{th}} = \frac{8\pi^2\sqrt{2}}{P_0\sqrt{P_0 d}}\left(\frac{K_2 \cdot K_3}{\alpha_2}\right)^{1/2}. \tag{116}$$

In classical experiments with rotating disks (see Section 2.1) performed on a 50 μm cholesteryl oleyl carbonate sample with the helical pitch 0.3 μm instability was observed at the velocity gradient $1.5 \cdot 10^3$ s^{-1},[142] which agrees within an order of magnitude, with calculations by relation (116).‡ The same method was used to observe propagating domains under shear deformation. In the mixture of MBBA and cholesteryl nonanoate (1%) with a helical pitch of 12 μm the initial planar texture was perturbed by an electric field. On the rotation of one of the bounding disks, the two-dimen-

†Relations (114) and (115) hold true if the inequality $\pi/d \ll k \ll 2\pi/P_0$ is satisfied.

‡For $P_0 = 0.3$ μm, $d = 50$ μm, $\alpha_2 = -1P$, $\sqrt{k_3 \cdot k_2} = 5 \cdot 10^{-7}$ dyn this calculation yields $S^{\text{th}} \simeq 5 \cdot 10^3$ s^{-1}.

sional deformation pattern ("square grid"[74]) became one-dimensional, the wave vector of this distortion being directed along the radius. Determining via a microscope the number of bright fringes that cross the field of view for a certain period, one can find the phase velocity of the propagating domains. The data of Figure 69 are obtained at points spaced 6 and 9 mm from the disk centre (points 1 and 2, respectively); here $\omega_d = v_d \cdot k$, $d = 50$ μm, $2\pi/k = 39$ μm. These data imply that $\omega_d/S = -0.25$, which also agrees (within an order of magnitude) with the calculated value $\omega_d/S = -0.15$.

In addition to the homogeneous and spatial-periodic distortion of the planar texture, shear deformation of cholesterics can lead to texture transitions. For instance, Pochan and Erhardt[129] have demonstrated that for low shear velocities a virgin planar texture passes into a confocal one which at high velocities changes to a homeotropic texture.

B. Compression deformation

The study of the behaviour of planar samples under compression deformation produced by an acoustic wave reveals a variety of transformations inherent in cholesteric crystals. We now consider these transformations in greater detail.

(a) Spatial-periodic distortion

The optical pattern corresponding to this type of distortion in cholesterics depends on the relationship between the sample thickness and characteristic

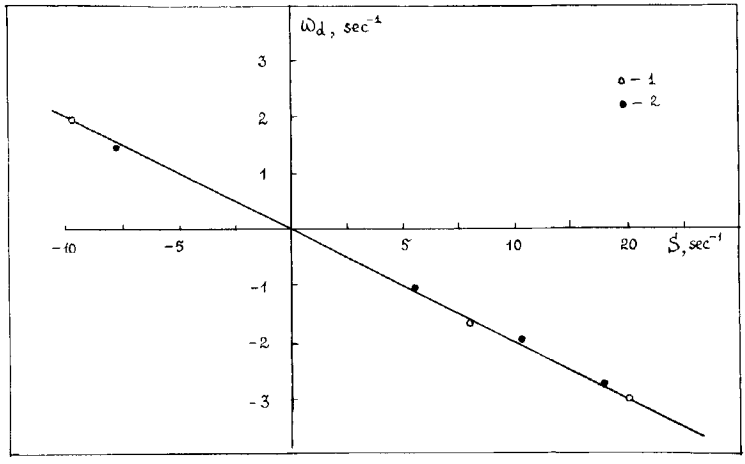

FIGURE 69 Phase velocity of domain propagation measured at points spaced 6 and 9 mm from the disk centre (1 and 2, respectively).

structure scale, helical pitch P_0. Of most interest is the case $d \ll P_0$ where a threshold deformation produces two-dimensional spatial-periodic distortion which in strong fields leads either to finger texture or to confocal texture. This distortion is characterized by an interesting optical pattern, a "square grid", which is formed above a critical field. According to experimental data, in the ultrasonic frequency range the distortion period $\Lambda \sim (P_0 d)^{1/2}$ (see Figure 70a).[143] These data refer to 10, 40, and 80 μm samples of a mixture of nematic crystal LC-404 and cholesteryl caprinate with equilibrium helical pitch 2, 4.2, and 10.5 μm. The experiments were carried out at 1.2 MHz in the configuration of Figure 1c (compression, $\mathbf{k} \| \mathbf{h}$). Let us discuss acoustical conditions in a sample when these "modulated" structures arise. Deformation observed in experiments is characterized by the average (with respect to the layer thickness) threshold gradient of the particle velocity, grad v_s^{th}. Curves 2 and 3 of Figure 70b show how this gradient varies with the increasing layer thickness in samples with a helical pitch of 10.5 and 4 μm. The figure also plots the threshold particle velocity $v_{0_s}^{th}$ in the incident wave for the same samples (curves 2′ and 3′, respectively).† It can be seen that for a constant helical pitch thinner samples exhibit higher threshold gradients; apparently, as d increases (for the same value of v_{0_s}), deformation changes more gradually, so that smaller velocity gradients are needed to overcome orientation-restoring elastic forces. It was found in experiments that grad $v_s^{th} \sim (d/P_0)^{1/2}$, i.e. the closer the helical pitch to the sample thickness and the lesser the number of cholesteric layers that fit this thickness, the higher is the threshold gradient. This relation is clearly illustrated in Figure 71; items 1–6 refer to the following samples: $d = 10$ μm, $P_0 = 10.5$ μm; $d = 10$ μm, $P_0 = 4$ μm; $d = 40$ μm, $P_0 = 10.5$ μm; $d = 40$ μm, $P_0 = 4$ μm; $d = 40$ μm, $P_0 = 2$ μm; $d = 80$ μm, $P_0 = 4$ μm; $f = 3.2$ MHz.

Comparison of these results with the data for a pure nematic (curves 1 and 1′ in Figure 70b) shows that as one passes from finite helical pitches to the limiting value $P_0 = \infty$, the threshold gradient grad v_s^{th} increases.

From the physical point of view, spatial-periodic director orientation can be interpreted as follows. Visual observations show that the onset of modulated structures in a layer is preceded by flows arising at an acoustic intensity lower than the threshold one. Since the acoustic field is inhomogeneous, the flows are not definitely oriented and their velocity (at acoustic intensity near the deformation threshold) ranges from several μm/s to tens of μm/s. The "network" is observed only in some areas of the layer,

†In front of a reflecting plate in the layer the particle velocity distribution along the normal to the plate is sinusoidal: $v = 2v_0 \sin(kz - \varphi')$; φ' is the reflection coefficient phase.

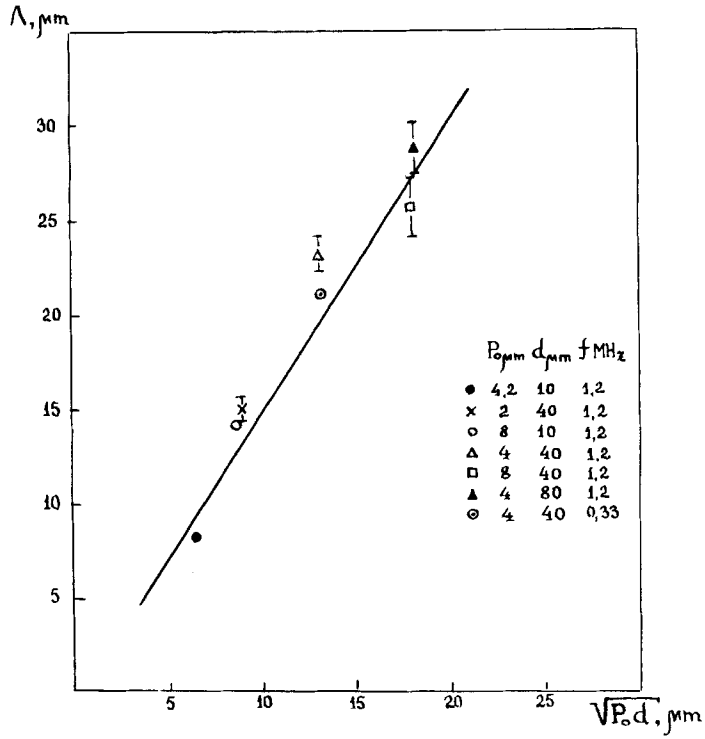

(a)

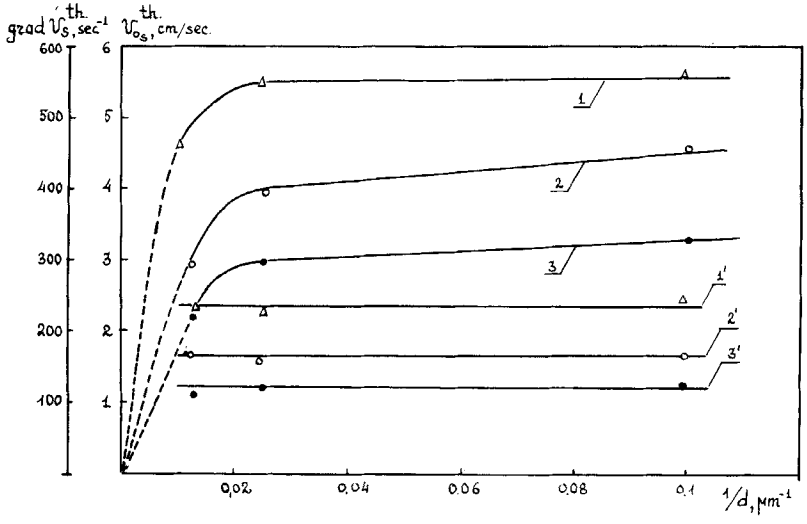

(b)

FIGURE 70 Effect of layer thickness and helical pitch on the spatial distortion period (a) and on the threshold particle velocity and threshold particle velocity gradient (b). Details in the text.

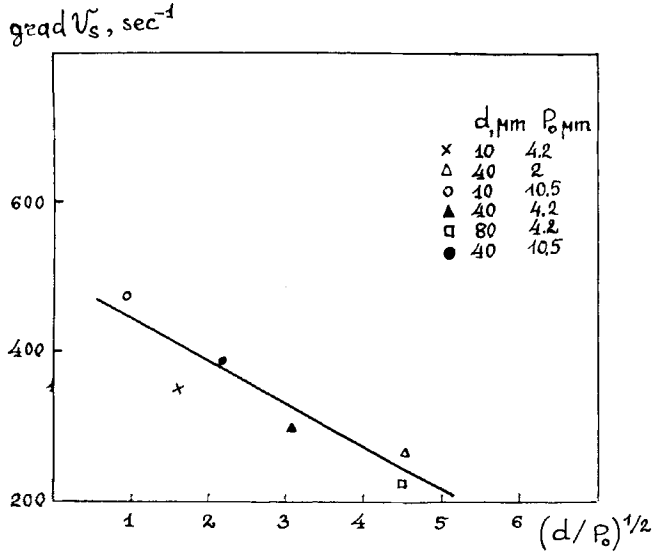

FIGURE 71 Relationship between the threshold particle velocity gradient, layer thickness, and helical pitch.

thereby indicating that spatial-modulated director tilt may arise for a definite mutual orientation between the director and the flow velocity. In all probability, in these areas the hydrodynamic destabilizing torque exceeds the elastic forces trying to preserve planar orientation and gives rise to a periodic distortion of cholesteric planes in mutually orthogonal directions. This leads to a two-dimensional periodicity of the refractive index and phase shift between the ordinary and extraordinary rays and, as a consequence, to optical manifestation of the instability in the form of a "network."

A theory describing the behaviour of a planar sample in a flow for an arbitrary angle ψ_0 between the director and the velocity vector† has not so far been developed. That is why we cannot compare quantitatively experimental data and the data presented above.

The periodic regular pattern shown in Figure 3b exists in a relatively narrow range of acoustic intensities and is modified even slightly above the deformation threshold. In certain places of the network a new structure arises. It originates near the square centres and is in the form of equidistant bright lines twisted into a helix, the lines being spaced at about half the helical pitch (the so-called finger texture[74]). This means that the cholesteric helical axis rotates through an angle about or equal to 90°. We could

†Precisely this situation is realized in cholesteric crystals with helical conformation in which the angle ψ_0 varies while passing from one cholesteric plane to another.

observe this texture transition only at frequencies about several hundred kHz (330 kHz). At higher frequencies the deformation pattern is modified immediately above the threshold and then is destroyed by acoustic flows. Successive stages of the phenomenon are shown in photos of Figures 72a, b, and c for an 80 μm sample with a helical pitch 4 μm at 1.2 MHz; the particle velocity in the incident wave v_s is 3, 8, and 14 cm/s, respectively.

(b) Inhomogeneous distortion

Interestingly, a transition from the planar to confocal texture in cholesterics with a large helical pitch caused by an ultrasonic wave is irreversible. At

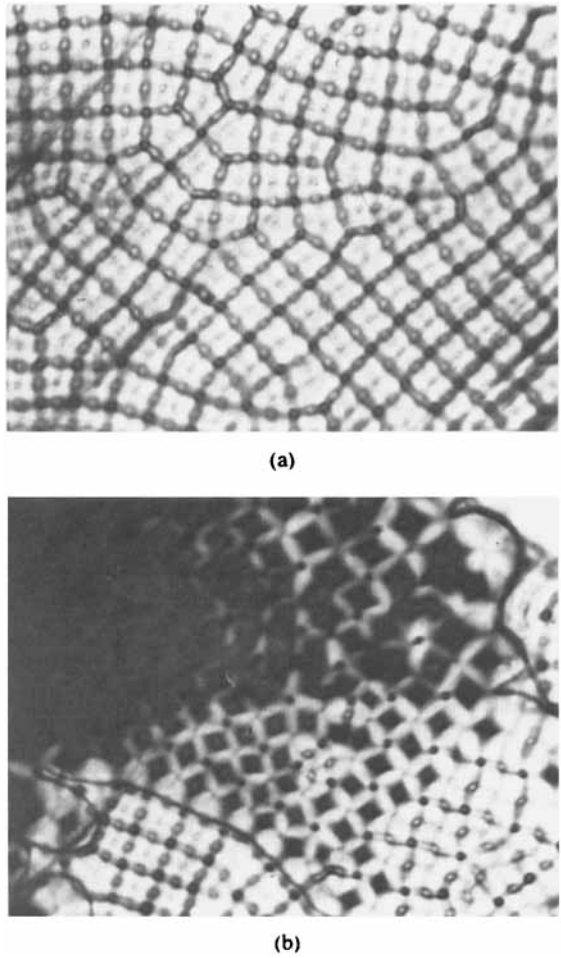

FIGURE 72 Successive stages of the spatial-periodic deformation pattern in an 80 μm planar cholesteric sample with a helical pitch 4 μm on increasing particle velocity; $f = 1.2$ MHz. Details in the text.

high sound intensities acoustic flows (Figure 72d) completely disorder the sample structure, thereby resulting in intense light scattering. The indicatrix of this scattering practically does not differ from that for a planar nematic sample under the same conditions (Figure 59).

Essentially, the threshold particle velocity $v_{s_{DSM}}^{th}$ at which scattering is observed decreases with increasing sample thickness, the larger the helical pitch, the smaller being the threshold (see Table II).[116] These data refer to a mixture of LC-404 nematic and cholesteryl caprinate ($f = 3.2$ MHz; compression; configuration of Figure 1c). The maximal value of the attenuation coefficient $\tilde{k}_0$ of the non-deflected light beam depends on deformation. As the layer thickness and helical pitch vary, the attenuation coefficient de-

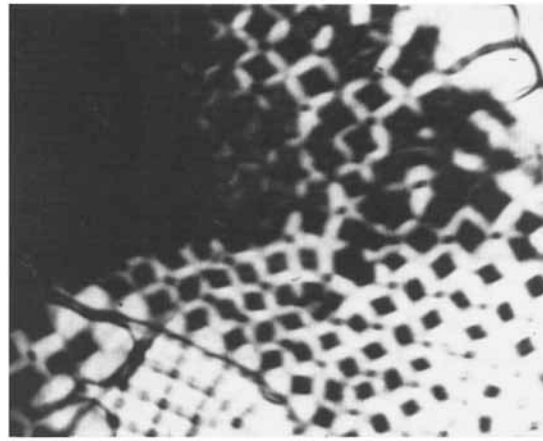

(c)

(d)

FIGURE 72 (*Continued*)

(e)

FIGURE 72 (*Continued*)

TABLE II

Effect of layer thickness and helical pitch on the threshold particle velocity

d, μm	10	10	10	40	40	40	80	80	80
P_0, μm	2	4	10.5	2	4	10.5	2	4	10.5
$v_{s_{DSM}}^{th}$ cm · s^{-1}	3.1	3.7	4	2.5	3	3.5	2.1	2.75	3.3

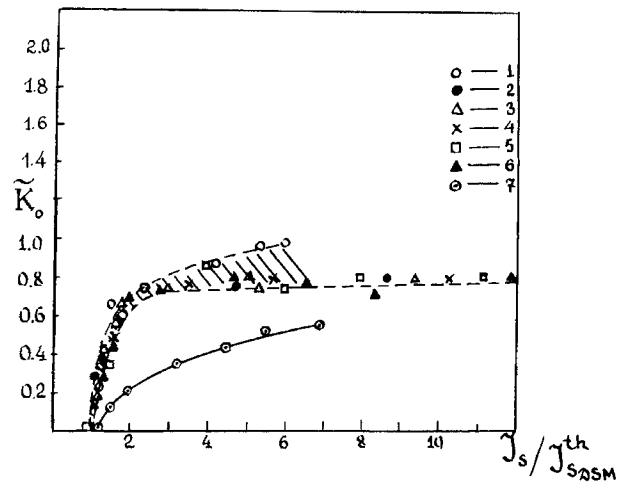

FIGURE 73 Maximal attenuation coefficient of the non-deflected beam in samples with different values of d and P_0. Parameters discussed in the text.

pends on how much the velocity v_s exceeds the threshold value. The corresponding data are presented in Figure 73; items 1–6 refer to samples with the following parameters: $d = 10$ μm, $P_0 = 10.5$ μm; $d = 10$ μm, $P_0 = 4$ μm; $d = 40$ μm, $P_0 = 10.5$ μm; $d = 40$ μm, $P_0 = 4$ μm; $d = 80$ μm, $P_0 = 4$ μm; $d = 40$ μm, $P_0 = 2$ μm.

After the field is switched off, a confocal texture is formed (Figure 72e), so that scattering is retained and, according to Refs. 116, 143 amounts to $\sim 0.5\tilde{k}_0$. The phenomenon resembles dynamic scattering with "memory." A confocal texture can be transformed into a planar one by applying an electric field (20 kHz); in this case the residual scattering is "erased." The inertial properties of the effect are discussed in detail in Section IV.

II.2.2. Confocal texture

A. Compression deformation

Mechanical deformation produced by an acoustic wave may not only destroy an oriented structure, but also order it. This effect was observed on samples with a confocal texture subjected to compression at frequencies 400 kHz and 3.2 MHz[145,146] (configuration of Figures 1b and c, respectively).

Figure 74 (curves 1–5) shows the change in the optical transmittance of a 35 μm sample (a mixture of MBBA and 5 wt.% of cholesteryl oleate) with increasing acoustic intensity for the following irradiation times: 60, 30, 20,

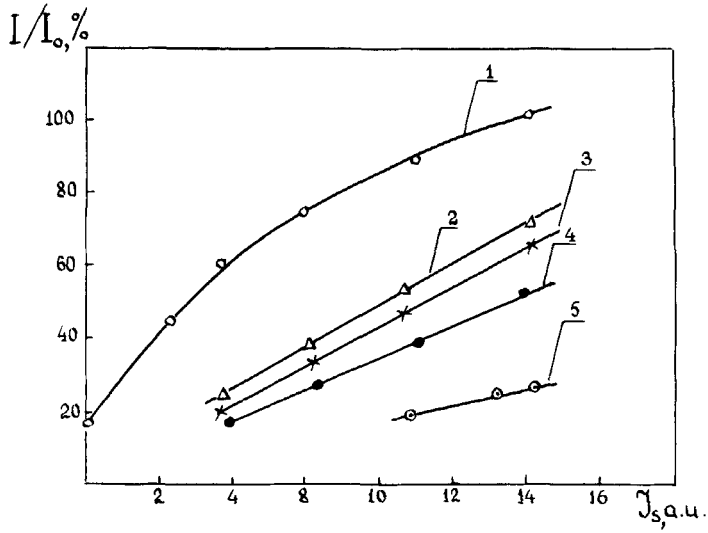

FIGURE 74 Optical transmittance of light in a mixture of MBBA and cholesteryl oleate (5 wt.%) as a function of acoustic intensity for different irradiation times: 60, 30, 20, 10, and 5 s (1–5, respectively); $d = 35$ μm; $f = 400$ kHz.

10, and 5 s (f = 400 kHz).[145] The initial confocal textures were obtained by applying an electric voltage (50 Hz, 50 V) across the sample. It can be seen that the sample transmittance rises with acoustic intensity tending to a value characteristic of a planar texture. Thus, the confocal texture turns into the planar one. Optically, such a transition is characterized by the change from a highly scattering to a transparent state of a sample.

II.2.3. Homeotropic orientation

We start an analysis of the behaviour of the homeotropic texture in cholesterics under mechanical deformation with the effects inherent only in this type of the mesophase.

Finger texture. The type of a texture formed in a cell with homeotropic boundary conditions in the absence of external factors is known to depend on the relation between the sample thickness and helical pitch. Haas and Adams[147] have shown that three types of texture can be formed: homeotropic (for $d < d_{cr} = P_0/2$), finger or periodic (for $d \geq d_{cr}$), and confocal (for $d \gg d_{cr}$).

The finger texture has been studied in detail by Press and Arrott.[148] They have demonstrated that such a texture is most favourable, provided $d \geq P_0/2$. Figure 75 shows the photo of the intermediate region where both the homeotropic and finger textures exist.

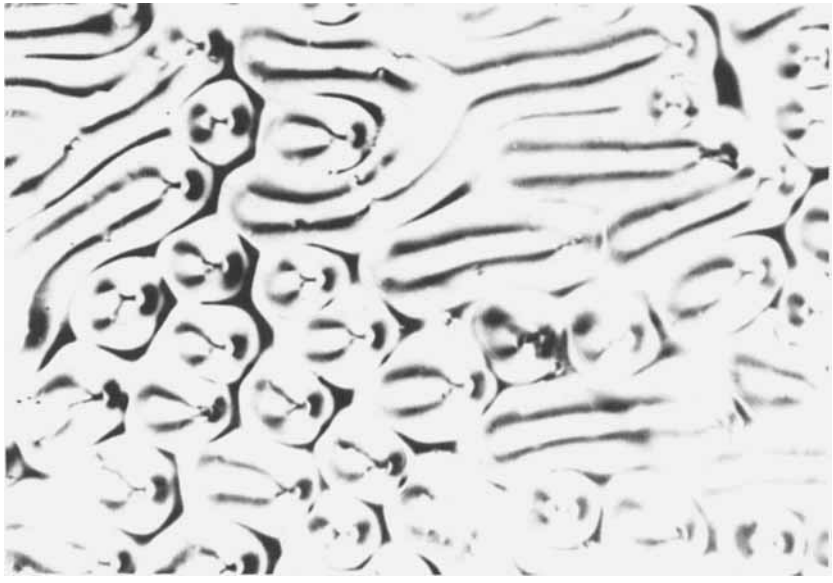

FIGURE 75 Finger and bubble textures in a mixture of MBBA and cholesteryl oleate.

Bertolotti *et al.*[149,150] have recently studied the behaviour of a finger texture formed in a 20 μm sample (a mixture of MBBA and 0.5 wt.% cholesteryl oleate) due to periodic deformation in the frequency range 0.1 Hz–130 kHz (configuration of Figure 1a; free-edge cell). It was found that at very low frequencies ($\sim$ 0.1 Hz) a periodic change in the pattern brightness follows the deformation applied. As the frequency increases, the pattern "darkens" and disappears at 1 Hz. Such a state of the sample persists up to 100–130 Hz when the finger texture appears again; but the wave vector of this distortion is tilted through 90° relative to its orientation in the unperturbed sample. As the frequency increases further, the pattern does not vary up to 14 kHz when the periodic structure disappears again; but it reappears at a slightly higher frequency, and the distortion wave vector returns to the initial position. In a higher frequency range deformation affects the fringe pattern only at resonance frequencies (70–80 kHz), the effect being manifested as a gradual vanishing of the pattern. Essentially, after deformation ceases, the pattern spontaneously arises in several minutes.[149,150]

These experimental results have been analysed in detail[150] within the framework of the familiar Press-Arrott model.[148]

Bubble domains. An interesting effect—the formation of the so-called bubble domains—was observed in cholesterics with the helical pitch satisfying $1.2 < P_0/d < 2$ under the homeotropic boundary conditions when a certain electric or magnetic field was applied to the sample.[151,152] The strength of this field must be higher than that characteristic of texture transformations, but lower than the dynamic light scattering threshold.

It was found that the effect can be initiated by mechanical deformation produced by acoustic waves.[153] Experiments have been carried out on 20–120 μm samples (a mixture of N–8 nematic and cholesteryl chloride and cholesteryl caprinate) at frequencies 216 kHz (shearing, configuration of Figure 1d), 514 kHz (compression, configuration of Figure 1a), and 3.2 MHz (compression, configuration of Figure 1c). The helical pitch was 48 μm, the sample edges were free. Experiments have shown that for $1.2 < P_0/d < 2$ two situations may occur, depending on the deformation level[154]:

1) if the acoustic intensity is less than the inhomogeneous distortion threshold, the initial homeotropic texture reappears in the sample after deformation ceases; 2) if the acoustic intensity exceeds this threshold, a new texture arises in the sample after irradiation ceases: regular circular domains against the background of homeotropic or finger texture. A conoscopic cross is observed in crossed polarizers at the centre of such a domain (Figure 76a). A diagram of molecular orientation inside the domain is schematically shown in Figure 76b.[155] It is a toroidal intermediate region between the outer and inner homeotropic regions. The structure of bubble domains has not so far been understood in detail.

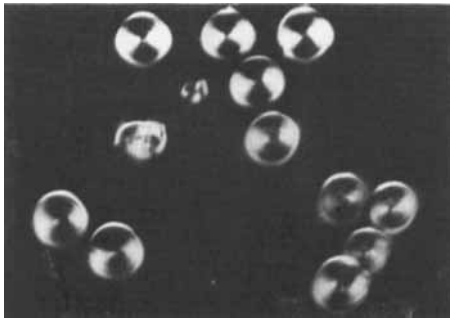

(a)

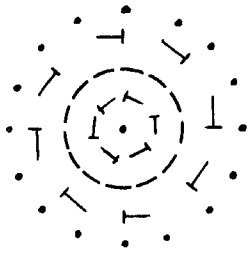

(b)

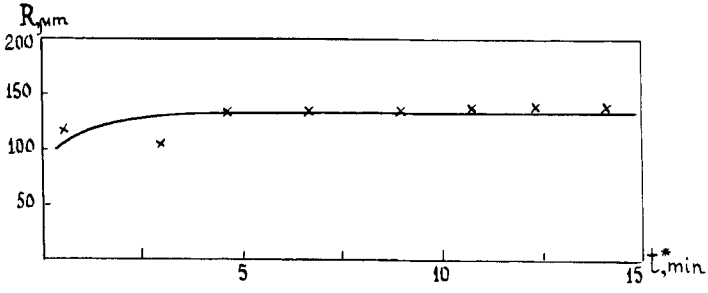

(c)

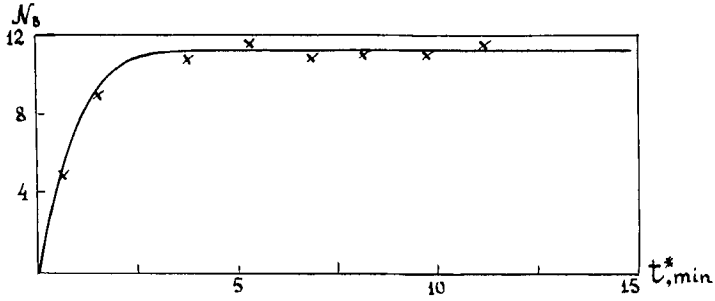

(d)

FIGURE 76 Bubble domains in cholesterics: photograph of bubble domains (a); molecular arrangement in a domain (b); variation with time of the diameter of a bubble (c) and of the number of bubbles (d).

The dynamics of acoustically initiated bubble domains has been studied by I. Gurova.[154] Figures 76c and d shows a typical behaviour of the diameter R of a single "bubble" and of the number of bubbles N_B as a function of time t^* after irradiation (sample thickness = 40 μm; helical pitch = 48 μm; f = 216 kHz; irradiation time = 1 min). It was found that the diameter R_M corresponding to an extremum of the size distribution of the number of bubbles $N_B(R)$ practically does not depend on frequency and deformation type, but is merely determined by the sample thickness ($R_M \sim d$). These data are presented in Figure 77, where 1 and 2 denote compres-

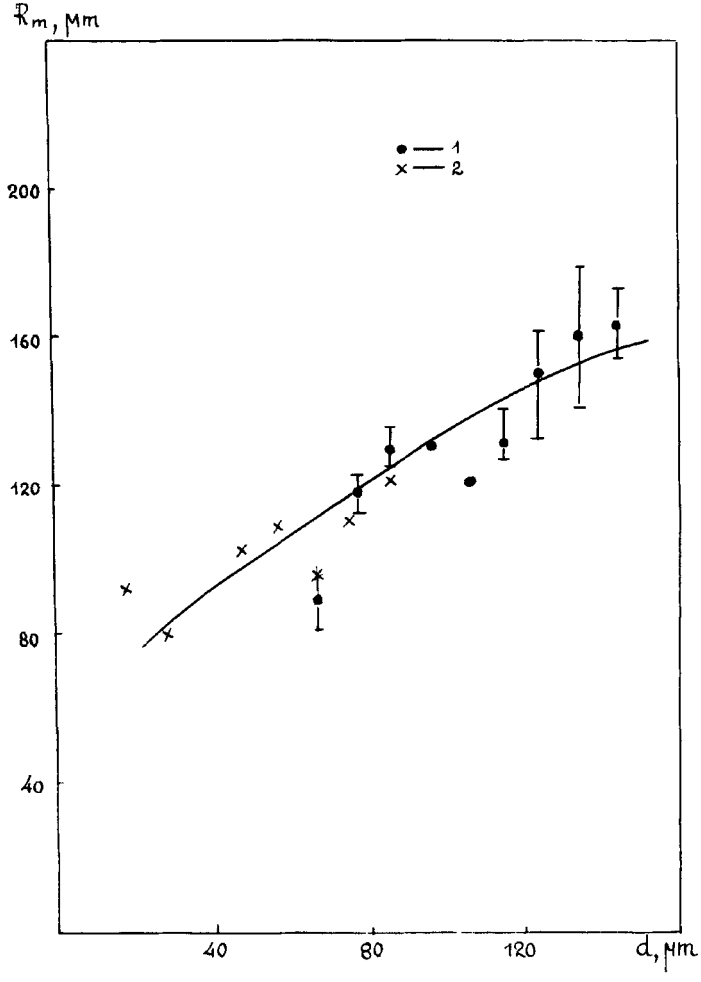

FIGURE 77 Effect of layer thickness on the size of a bubble domain. 1: compression; 2: shear.

sion (~ 3 MHz) and shearing (216 kHz), respectively; $P_0 = 48$ μm. The bubbles are formed in regions with the highest defect density (filament disinclinations) at points where disinclinations appear on the surface, the number of bubbles depending both on the layer thickness and the vibration frequency.

Essentially, the bubble texture possesses a considerable time hysteresis ("long-term" acoustic memory). The initial orientation can be restored by applying an ac electric field (~ 60 V, 20 kHz) the bubbles grow in size, merge, and disappear.

It should be noted that the intensity of light passing through the initial (homeotropic) and final (bubble) texture differs by an order of magnitude.

Let us also point out some transformations in cholesterics which are of no lesser interest than those considered above. They may be classified with regard to the same characteristic feature: relation between the layer thickness and the helical pitch.

1) When $d \ll P_0$ and the bounding plates are so treated as to obtain homeotropic orientation, the helix gets untwisted and a homeotropic nematic structure arises; under deformation this structure experiences all distortion stages considered above (see Section I). According to our data, however, these phenomena are characterized by lower (as compared with nematic) distortion thresholds and steeper contrast curves.

2) If $d \gg P_0$, a homeotropic layer can be obtained near the bounding surfaces without helix untwisting. In this case compression at ultrasonic frequencies produces only inhomogeneous structure distortion: the density of disinclinations gradually increases with acoustic intensity, so that a polycrystalline texture is eventually formed in the sample. Reversibility of this transformation implies that annihilation and nucleation of disinclinations are also reversible. These data refer to a mixture of LC-404 nematic and cholesteryl caprinate (5%) with a helical pitch of 3 μm ($f = 3.2$ MHz; experimental geometry of Figure 1c). It is worth noting that the maximal attenuation coefficient of the non-deflected beam did not exceed 0.5 (see Figure 73; item 7). This can be attributed to the fact that the sample is opaque in the initial state, for homeotropic orientation exists only in a thin surface layer.[116]

III. ACOUSTOOPTICAL EFFECTS IN SMECTIC CRYSTALS

The behaviour of smectic mesophases is the least developed trend in the acoustooptics of liquid crystals. This is mainly because such crystals have a relatively large "stiffness", and oriented samples are rather difficult to obtain and identify. Almost all the data available in the literature refer to *homeotropic samples* of smectic A and C phases, that is why in this section

we shall only discuss the behaviour of homeotropically oriented A and C mesophases.

III.1. Smectic A phase

First experiments with smectics A were performed on non-oriented ethyl para-azoxycinnamate under compression deformation at ultrasonic frequencies (700 kHz). With an acoustic intensity of 3 W/cm^2 the optical transmittance of the sample sharply decreased (during several seconds) and was not restored after deformation ceased.[85] These experiments, carried out more than 20 years ago, have revealed a unique property of "memory" inherent in the smectic phase. Later investigations have shown that deformation of this phase gives rise to all types of structure distortion. Let us consider them in greater detail.

III.1.1. Homogeneous distortion

Bertolotti and coworkers used the conoscopic method to observe this type of distortion in a 50 μm homeotropic CBOOA sample under pulsed compression (configuration of Figure 1a).[51] The duration of square pulses varied from 10 to 20 ms and the repetition rate, from 0 to 200 kHz. The onset of structure distortion was detected as the modification of the conoscopic pattern (the cross turned into hyperbolae). It was found that the region of homogeneous distortion is rather narrow, which makes it difficult to obtain a quantitative relation between the optical and acoustic signals. However, the curves of Figure 78 permit the comparison of the optical signals and threshold stresses corresponding to the aforementioned modification of the conoscopic pattern in nematic and A smectic phases at temperatures close to the point of the smectic A–nematic phase transition. Curves 1 and 1′ show the behaviour of the effective threshold (as regard the voltage across the acoustic transducer $U_{\text{ef}}^{\text{th}}$); curve 2 is the optical signal; dashed curves correspond to smectic A; ΔT is the difference between the sample temperature and the phase transition point T_{S_A-N} (the pulse repetition rate was 16 kHz). It can be seen that in the smectic phase the optical signal changes slower with decreasing temperature than in the nematic phase when the sample temperature increases. The nematic phase also exhibits more considerable changes in the threshold $U_{\text{ef}}^{\text{th}}$. Essentially, at frequencies 400 kHz and higher in the continuous mode of operation the laminar motion in the layer does not modify the conoscopic pattern, i.e. the homeotropic structure is not distorted. These data were obtained on a 50 μm OCB sample in a free-edge cell (experimental geometry of Figure 1a).[156] No birefringence modification was observed in homeotropic CBOOA samples in surface-wave experiments

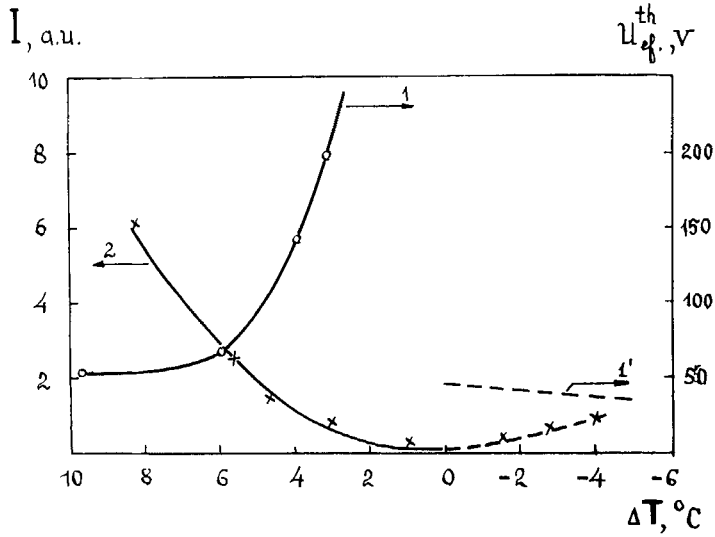

FIGURE 78 Threshold voltage and optical transmittance as a function of temperature for a CBOOA sample in the smectic A and nematic phases. Details in the text.

($f = 12.3$ MHz).[66] At higher vibration amplitudes the structure distortion was revealed as the formation of defects (disinclination lines).

III.1.2. Spatial-periodic distortion

According to the de Gennes theory, extension or compression of a homeotropic A smectic along the normal to the layer plane may result in two types of instability: undulation instability under longitudinal flexure and instability related to molecular tilt inside the layer or, as usually said, under longitudinal director flexure.[74]

In Durand-Ribotta's experiments with periodic compression and tension of a CBOOA sample the undulation instability arose in the tension phase above the threshold displacement ξ_0^{th} as a system of equidistant bright lines.[157,158] At displacements 4–5 times larger than the threshold one this pattern turned into a network of lines crossing at about 90°. As the displacement increased, the intersection angle decreased to 60° and then the structure was split into confocal domains 4–10 μm in diameter.

Essentially, this type of distortion is also accompanied with a change in the scattered intensity as the displacement grows (Figure 79). Scattering begins with the formation of linear domains, while in the stage of domain intersection the scattered intensity approaches a constant value. The curve in Figure 79a corresponds to a 330 μm CBOOA sample; the pulse repetition rate is 2 Hz; temperature is 79°. As the frequency increases up to $f = f_c$ (f_c

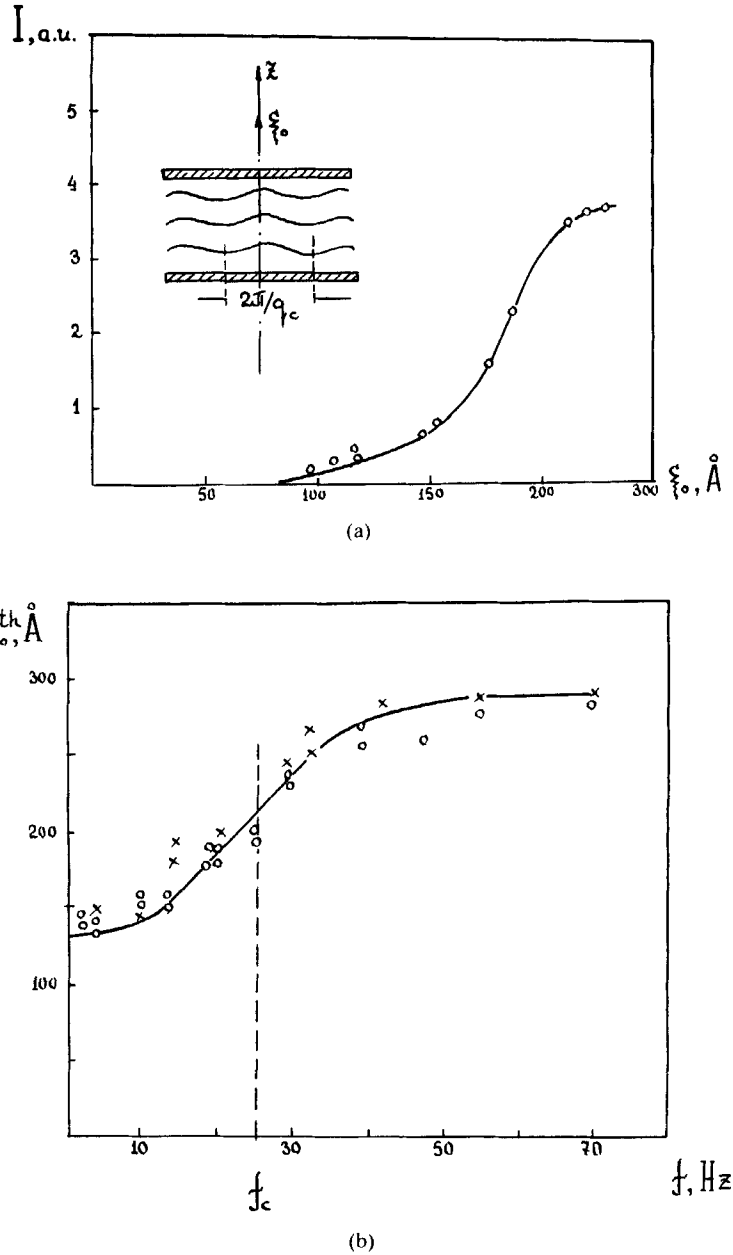

FIGURE 79 Undulation instability in a homeotropic smectic A sample: scattered intensity as a function of displacement in the tension phase (a) frequency dependence of the threshold displacement (b).

is the instability relaxation frequency), the threshold displacement ξ_0^{th} rises and then tends to a constant value (see Figure 79b; $d = 330$ μm, $t = 79°$). It was found that the wave vector determining the instability period varies slightly about the value $q_c = (\pi/\lambda_s d)^{1/2}$ for which the threshold displacement is minimal ($\lambda_s = (K/\bar{B})^{1/2}$ is the characteristic length of A smectic, $\bar{B}$ is the elastic modulus which allows for the change in the spacing of smectic layers under an external force).

Undulation instability was also observed at ultrasonic frequencies on a 50 μm OCB sample in a free-edge cell with a circular transducer. As the voltage across the transducer grew, the structure experienced the following modifications: a) reversible distortion as a system of fringes (with a period of ~ 5 μm); b) irreversible distortion giving rise to confocal domains.[156]

Similar structure modifications arise in the flow of smectic A in a planar capillary. They were observed in a 100 μm cell filled with OCB.[156] This enables one to suggest that the above modifications are the result of the interaction between the orientation and the acoustic flow.

According to the theory, the instability caused by molecular tilt in the layer can be produced by compressing a sample of smectic A at a pressure of ~ 10^5 Pa/cm^2, the value rarely attainable in practice. This type of distortion can, therefore, be observed in experiments at temperatures close to the smectic A–smectic C phase transition point.

Such an experiment was carried out on a soft HOBHA sample at temperatures exceeding the phase transition point $T_{SmA-SmC}$ by 0.2–0.5 °C.[157] The duration of square voltage pulses was 1 s. Figure 80a shows the intensity of light passing through a 20 μm sample (in crossed polarizers) for $\Delta T = 0.20$ °K. Here U_1^{th} is the instability threshold, U_2^{th} is the threshold of the formation of a mosaic structure. The experiment has revealed that near the phase transition point the threshold U_1^{th} rises with the sample temperature (Figure 80b).

III.1.3. Inhomogeneous distortion

The stiffness of smectic phases implies a much higher deformation threshold (for this type of distortion) as compared to nematic and cholesteric crystals, the value of this threshold being practically independent of the choice of a surfactant. For example, in a 60 μm sample (a mixture of 55% OCB and 4-hexyoxyphenyl ester of 4-butylbenzoic acid) under compression deformation at 1 MHz the threshold voltage changed only by 2–3 V with the use of lecithin and chromolan, and after chemical treatment of the surfaces.[116,159] On the contrary, in nematics, as is seen from Figure 81, this factor is rather essential. Here group A is represented by 10 μm MBBA samples oriented by introducing CTAB into the bulk; group B is represented by the samples with a lecithin layer on the surface (P_s^{th} is the effective clearing threshold

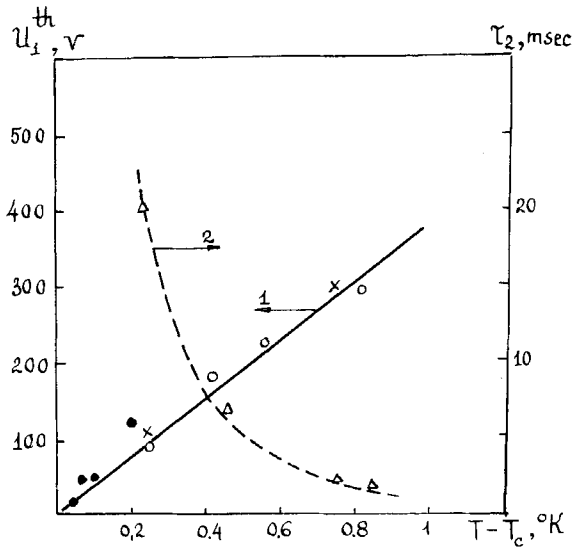

(a)

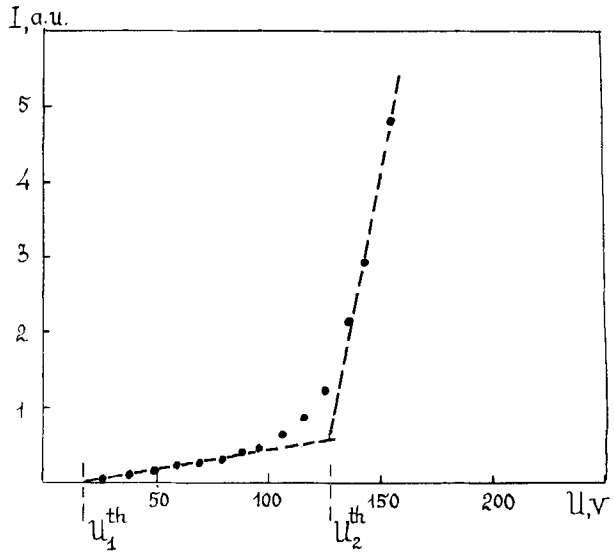

(b)

FIGURE 80 Instability caused by the tilt of molecules within a homeotropic smectic A layer: optical transmittance as a function of transducer voltage (compression) (a); the threshold voltage of instability onset and structure relaxation time as a function of temperature (curves 1, 2) (b).

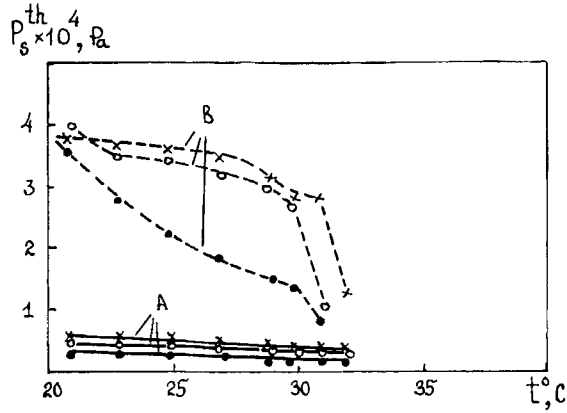

FIGURE 81 Effect of surfactants on the sensitivity of MBBA samples (homeotropic orientation). Parameters discussed in the text.

with respect to acoustic pressure, T_{N-I} is the temperature of the nematic–isotropic liquid phase transition). We see that in smectic A, as well as in nematic, the threshold decreases with increasing temperature. It was found that a surfactant affects the maximal attenuation coefficient of the non-deflected beam. This is also confirmed by the data of Figure 82a where items 1–3 refer to cells whose surfaces are chemically cleaned or treated with lecithin or chromolan. The experiments were conducted on a 60 μm layer at 1 MHz (compression; configuration of Figure 1b).[159] It is essential, however,

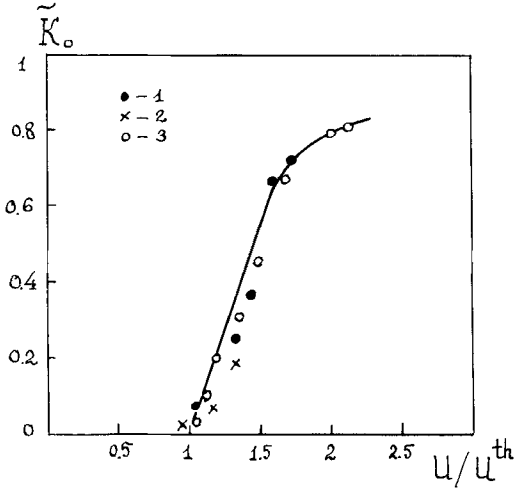

FIGURE 82 Effect of treatment of substrates (chemical cleaning (1), treatment with chromalan (2) and lecithin (3)) on the maximal attenuation coefficient of the non-deflected beam.

that $\tilde{k}_0$ depends on how much the value of U exceeds the threshold $U_{s_{DSM}}^{th}$.

It should be noted that acoustic memory is well pronounced under inhomogeneous distortion of smectic A[159,160]; this effect is discussed in Section IV dealing with the inertial properties of liquid crystals.

III.2. C and C* smectics

Data on acoustoopitcal phenomena in these phases are rather scanty.[157,161] The above-mentioned Durand-Ribotta experiment has revealed a high sensitivity of the smectic C phase to mechanical deformation.[157] In all probability, the optical transmittance varies under such conditions because of the modulation of the molecular axes tilt when a homeotropic structure is distorted as a result of periodic tension and compression of the layer.

As for the chiral smectic C*, the effect of deformation is manifested in a more varied fashion. As in the case of cholesteric crystals, one may observe, besides the effects due to texture modification, helix untwisting typical only of substances with a helical structure.

The possibility of observing this effect was discussed in Refs. 161–163 where it was shown that in the case of incomplete untwisting the conscopic pattern just shifts.[161,162] A detailed study of the optical properties of a homeotropic SmC* sample under such structure distortion caused by a periodic shear of one of the bounding plates was performed by Guyon *et al.* on a DOBAMBC sample with dipole ordering.[163] The dipole moment of this substance is of the order of 10^{-2} D and is oriented almost perpendicular to the long molecular axis. The dipole moments of each layer are aligned in the same direction, but the structure as a whole is not polar (see Figure 83). The symmetry of this structure is described by the group $\infty 2$. Untwisting of such a helix, say due to shearing, gives rise to a polar ferroelectric structure with point symmetry 2.

The experiments were performed with 200–300 μm samples; the light beam propagated along the helix axis, the vibration frequency was not higher than 1200 Hz. The conoscopic pattern was formed on a semitransparent screen at a distance of 165 mm from the sample.[163] Then the screen was replaced by two photodiodes to measure the mean light intensities I_A and I_B at neighbouring areas "A" and "B" of the conoscopic pattern. The size of the areas was (1×10 mm^2) and the angle between their centres, about 0.4°. The design of the experimental setup enabled accurate measurement of the rotation angle ψ_1 of the optical system. Helix distortion under shearing produces a shift of the conoscopic pattern, and the change in the light intensity is measured by the photodiodes. Figure 84 shows a typical dependence of the transmitted intensity on the incidence angle for a DOBAMBC sample in the initial state and under shearing. It can easily be

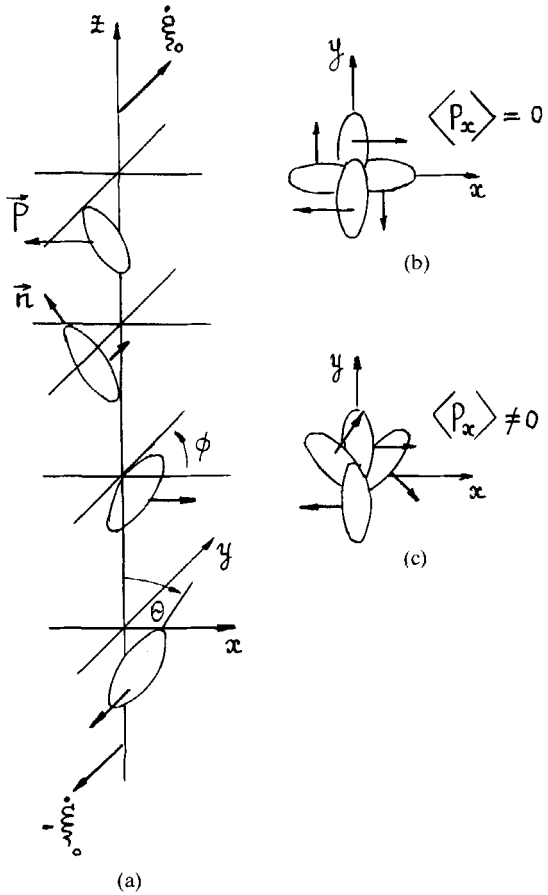

FIGURE 83 Schematic diagram of dipole ordering in a chiral C* smectic: spatial arrangement of molecules (a); view along the helix axis: non-deformed state (b); deformed state (c).

seen that shear deformation affects significantly the transmittance. These curves correlate well with theoretical results[164]; the theory predicting a number of specific features in the intensity behaviour which were not observed in the experiment.

The temperature dependence of the light intensity at fixed incidence angles and constant shearing frequency is shown in Figure 85 (curve 1). It is similar to the temperature dependence of shear-induced polarization.[162] In both cases the maximum of the curves lies below the temperature of transition to the smectic A phase; the same temperature dependence is reported in Ref. 165 for the tilt of DOBAMBC molecules, but the reason for such a behaviour has not so far been understood. One may assume that it is

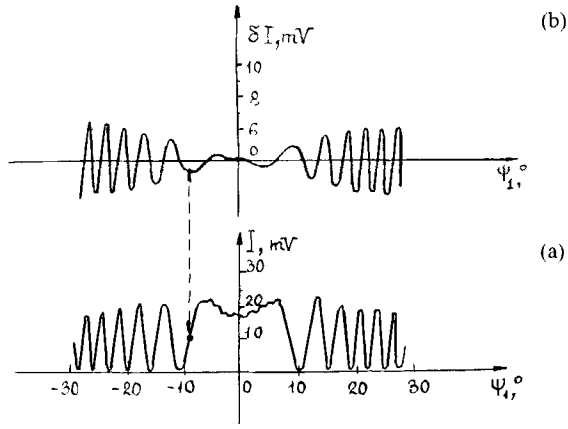

FIGURE 84 Intensity of light transmitted through a DOBAMBC sample vs. the incidence angle: non-deformed state (a); deformed state (b).

caused by transient processes.[163] Curve 2 in this figure shows the phase difference β_{ph} between the distortion of the conoscopic pattern and the shear inducing this distortion. The data refer to a 200 μm sample at 160 Hz.

It was found that the light intensity and phase difference (at constant incidence) depend linearly on the frequency.

The experimental results show that at frequency 30 Hz, amplitude 40 μm, and temperature 80° the centre of the conoscopic pattern in a 200 μm DOBAMBC sample shifts through an angle 0.35°. We note that the phase difference β_{ph} between the conoscopic pattern distortion and shearing increases with the helical pitch. This follows from the study of a mixture of SmC* and its racemic modification.

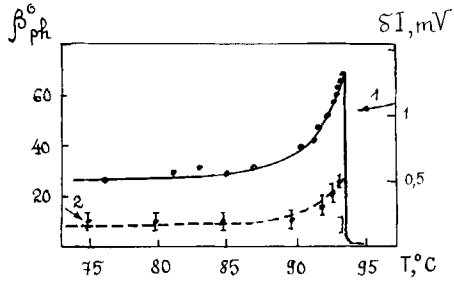

FIGURE 85 Effect of temperature on the transmitted intensity at fixed incidence angle and frequency and on phase difference between the conoscopic pattern distortion and initiating shearing (curves 1, 2); 200 μm DOBAMBC sample; f = 160 Hz.

IV. INERTIAL PROPERTIES OF LIQUID CRYSTALS

To analyse transient processes of "switching-on" and "switching-off" of deformation effects and derive expressions for the response and relaxation times τ_1 and τ_2 of these effects, one has to solve the equation of motion in which the viscous friction moment $\gamma_1(d\varphi/dt)$ is set equal to the sum of the elastic moment $K_i(\partial^2\varphi/\partial z^2)$ and the destabilizing torque.

In the previous sections we have pointed out that the mechanism of deformation distortion and, therefore, the nature of the torque depend on boundary conditions, layer geometry, type of distortion, and frequency. Thus, the inertial properties of liquid crystals under deformation-induced distortion are determined both by the above factors and by their viscous-elastic properties. Since the type of distortion is of most significance, we shall classify the data now available with respect to this factor.

IV.1. Homogeneous distortion

The data concerning the behaviour of different types of mesophases under deformation imply that this type of distortion is mainly observed in the nematic phase.

IV.1.1. Nematic phase

Consider the most common boundary conditions—homeotropic ones. Figure 86 shows the response time (curves 1–3) and relaxation time (curves 1′–3′) for 100 μm samples subjected to compression deformation at ultrasonic frequencies as a function of acoustic intensity. Curves 1 and 1′ are for an MBBA sample at 1.9 MHz[19]; curves 2, 2′ and 3, 3′ refer to PCB samples at 2.1 MHz.[46] The experiments were performed with configuration of Figure 1b; the acoustic wave fell onto the layer at 30°[45] and 20°,[43] respectively.† Comparison of these data shows that only for small J_s does the switching-on time exceed the switching-off time. Interestingly, the times τ_1 and τ_2 differ for MBBA and PCB samples. This may be due to a difference in the viscous-elastic properties of these substances, and also due to inaccurate values of J_s obtained in these experiments.

Both τ_1 and τ_2 increase with the sample thickness. This is clearly seen from Figure 87 referring to the same MBBA sample as in Figure 86, for $J_s = 600$ W/cm^2, $f = 1.9$ MHz.

The same behaviour of τ_1 was also observed under shear deformation. According to the data of surface-wave experiments,[66] τ_1 is ~ 1 s in a 60 μm MBBA layer ($f = 12.3$ MHz). As far as the relaxation time τ_2 is concerned,

†These angles correspond to maximal acoustic transmission of the cells.

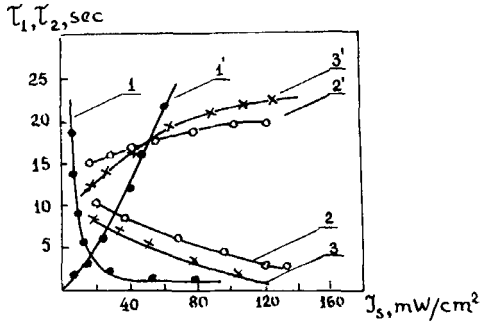

FIGURE 86 Inertial properties of homeotropic nematics under homogeneous deformation: response time τ_1 (curves 1–3); relaxation time τ_2 (curves 1′–3′).

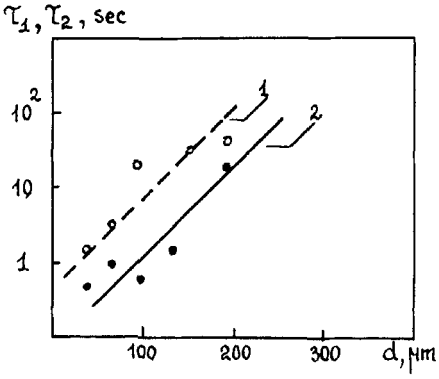

FIGURE 87 Effect of layer thickness on the inertial properties of homeotropic nematics.

the viscous wavelength rather than the layer thickness seems to be a characteristic magnitude. Indeed, the balance condition for the elastic and viscous moments in the absence of acoustic field can be written in a simpler form†

$$K_3 = \frac{\partial^2 \varphi}{\partial z^2} = \gamma_1 \frac{\partial \varphi}{\partial t}, \tag{117}$$

whence

$$\tau_2 = \frac{\gamma_1 \lambda_{vis}^2}{K_3 (2\pi)^2}. \tag{118}$$

†In an acoustic field the director behaviour is described by Eq. (56).

We point out that the relaxation time for the electroopic effect, which is an analogue of the deformation distortion considered here, is given by

$$\tau_2' = \frac{\gamma_1 d^2}{K_3}. \tag{119}$$

IV.1.2. Smectic A phase

As was already noted, homogeneous distortion in a homeotropically oriented CBOOA sample was observed in a rather narrow interval of acoustic intensities.[51] It was found, however, that this distortion is reversible, and after the deformation ceases the conoscopic pattern is restored in a time varying from tens to hundreds of milliseconds. As is seen from oscillograms for a 50 μm CBOOA sample, the optical signal copies the acoustic one with a delay of several microseconds (the data refer to the following repetition rates of driving electric pulses: 5, 14, and 26 kHz).

IV.1.3. Smectic C phase*

As far as we know, the data concerning the inertial properties of this phase are reported in Ref. 163 where helix untwisting in a homeotropic DOBAMBC sample was studied under periodic shearing of one of the substrates according to the law $v = v_0 \exp(i\omega t)$. The destabilizing torque $\alpha(v/d)\cos\phi$ gives rise to the helix distortion

$$\phi(z, t) = qz + \phi_0 \cos qz \exp i(\omega t + \beta_{ph}). \tag{120}$$

Substituting this expression into the balance equation for the elastic, viscous, and destabilizing moments†

$$B_3 \frac{d^2\phi}{dz^2} - \gamma\phi = -\alpha \frac{v \cos\phi}{d} \tag{121}$$

we find the distortion amplitude

$$\phi_0 = \frac{\alpha v}{\gamma d \left[\omega^2 + (1/\tau_2)^2\right]^{1/2}}, \tag{122}$$

†Equation (121) describing the behaviour of the angle ϕ includes the coefficients γ and $\alpha = \gamma\lambda'$. They were introduced in Ref. 166 for the hydrodynamic description of the behaviour of smectics. The elastic coefficient B_3 was introduced in Ref. 74.

where

$$\tau_2 = \gamma P_0^2 / B_3 (2\pi)^2 \tag{123}$$

is the relaxation time of this distortion. Since $\beta' = -(\tan \omega\tau_2)^{-1}$, the slope of the experimental curve $\beta'(f)$ shown in Ref. 163 determines the relaxation time (it amounts to $1.9 \cdot 10^{-4}$ s). We recall that the helical pitch P_0 appears in (123) as a characteristic magnitude.

IV.2. Spatial-periodic distortion

Transient processes in this distortion state have been studied little. In nematic crystals the characteristic times of the onset and vanishing of an orientation instability (it is generally governed by the same torques that operate under homogeneous distortion) seemingly do not differ from the values τ_1 and τ_2 typical of this type of distortion.

No data are now available on the times of instability onset and relaxation of a two-dimensional pattern (network) in planar cholesteric samples. According to Ref. 150, for a finger structure under compression-initiated texture transitions (0.1 Hz–130 kHz) the response and relaxation times are about 1 ms and 30 ms, respectively. These data were obtained on a 20 μm sample of a mixture of cholesteryl oleate and MBBA.

The inertial properties of spatial-modulated structures (corresponding to undulation instability) in A smectics have been studied in Durand-Ribotta's experiments.[157] The network distortion and tension-induced confocal domains in a 200 μm CBOOA sample relaxed so slowly (from 10 s to several hours) that here we may speak about memory effect. In a 20 μm homeotropic HOBHA sample the characteristic times of instability due to molecular tilt and distortion relaxation at the deformation threshold are 0.6 and 1 ms, respectively. Above the threshold, up to deformations when a mosaic structure is formed, the response time does not change, while the relaxation time increases by a factor of two; even larger τ_2 values (hundreds of milliseconds) are typical of the mosaic structure. As the temperature rises (on approaching the SmA–SmC phase transition) the relaxation time decreases. This is evidenced by curve 2 of Figure 80b corresponding to a 20 μm HOBHA sample under compression.

IV.3. Inhomogeneous distortion

We recall that this state of structure distortion is accompanied with intensive light scattering, mainly by director orientation fluctuations, the non-deflected beam being attenuated because of the change in the light

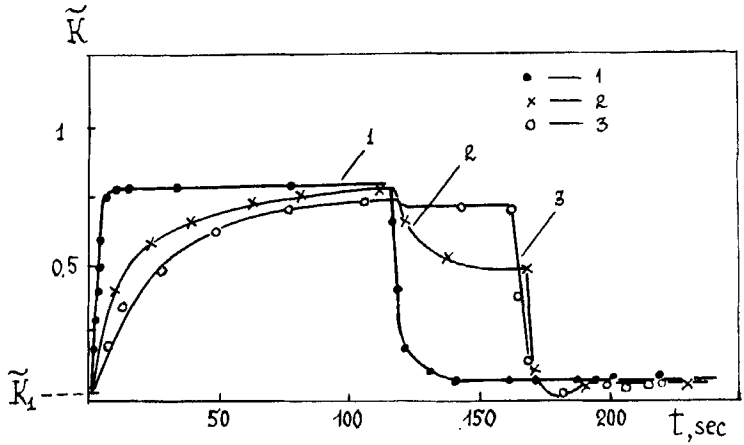

FIGURE 88 The kinetics of dynamic light scattering in nematics, cholesterics, and A smectics (curves 1–3).

propagation direction.[29,110] The transient processes of this deformation effect are especially sensitive to the mesophase type. The time dependence of the attenuation coefficient of the non-deflected beam $\tilde{k}$ (Figure 88, curves 1–3) clearly demonstrates the specific kinetics of the three phases (nematic, cholesteric, and A smectic†) under compression deformation at ultrasonic frequencies. These data were obtained in experiments with the configuration of Figure 1c at 3.2 MHz (curves 1 and 2, $d = 40$ μm) and 1 MHz (curve 3, $d = 60$ μm).[29,159,160] It can be seen that the attenuation coefficient grows from the initial value $\tilde{k}_1$ to the maximal value $\tilde{k}_0$ corresponding to a given acoustic intensity. After the deformation ceases (vertical dashed line in Figure 88) spontaneous complete restoration of the initial orientation and, therefore, of the initial attenuation coefficient $\tilde{k}_1$ occurs only in nematics. Cholesterics and smectics retain, as a rule, an intensively scattering confocal texture, the coefficient of residual scattering being $\tilde{k}_2 \gg \tilde{k}_1$ (dynamic scattering with "memory").[160,168] The initial orientation can be restored in these cases by applying an electric field (~ 20 kHz).[160] As was already noted, the residual scattering in the cholesteric and smectic phases amounts to $0.5\tilde{k}_0$[116,160] and $0.8\tilde{k}_0$,[116,159] respectively.

Since dynamic scattering is an important practical effect, we shall consider its time characteristics at greater length.

†Measurements were conducted with homeotropic nematic and A smectic samples, and also with a planar sample of the nematic–cholesteric mixture with an equilibrium helical pitch of $P_0 \sim 4$ μm.

IV.3.1. Nematics

In this mesophase the times of switching-on and switching-off of dynamic scattering depend both on the layer thickness and on the initial molecular orientation. It was found that for homeotropic, as well as for planar orientation, τ_1 and τ_2 grow with the layer thickness according to the law $\tau_1 \sim d^{1/2}$, $\tau_2 \sim d^{3/2}$.[116,144] This is evidenced by Figure 89 where items 1, 2

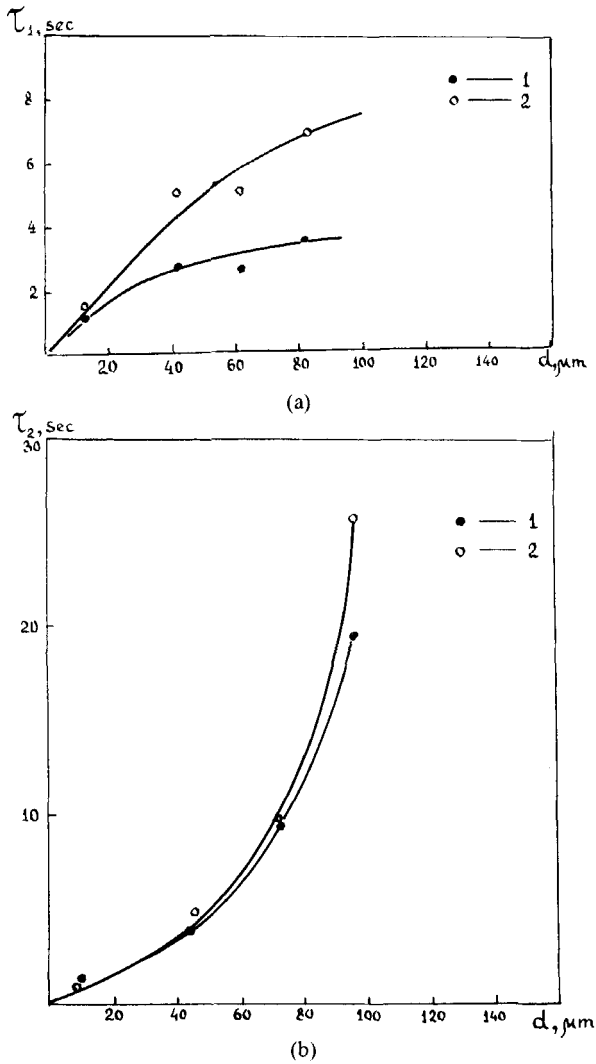

FIGURE 89 Effect of layer thickness on switching-on and switching-off times of dynamic light scattering for homeotropic (1) and planar (2) samples.

refer to MBBA-EBBA samples with homeotropic and planar orientation, respectively; $f = 3.2$ MHz, compression. The times τ_1 and τ_2 were calculated from the time dependence of the attenuation coefficient $\tilde{k}$ in the non-deflected beam (against the level 0.1). Essentially, τ_1 is higher for samples with planar orientation, and τ_2 does not depend on molecular orientation in the layer. With increasing acoustic intensity τ_1 decreases for both types of orientation.

IV.3.2. Cholesterics

The time characteristics of dynamic scattering with memory have been studied most completely for planar samples of nematic–cholesteric mixtures subjected to compression at ultrasonic frequencies. Reference 116 reports the results of such studies for a mixture of LC-404 nematic and cholesteryl caprinate; the concentration of the optically active component varies from 1.9 to 7.4%, corresponding to the change in the equilibrium helical pitch from 2 to 10.5 μm. As in the case of nematics, τ_1 and τ_2 were determined from the experimental kinetic curves of the effect. The portion of this curve corresponding to the rise of the attenuation coefficient $\tilde{k}$ from the initial value $\tilde{k}_1$ to the maximal value $\tilde{k}_0$ (information recording) can be approximated by the expression

$$\tilde{k} - \tilde{k}_1 = (\tilde{k}_0 - \tilde{k}_1)[1 - \exp(-\alpha_1 t)] \tag{124}$$

where $\alpha_1 = A/\tau_1$ is the time constant. Figure 90a shows the behavior of α_1 with increasing particle velocity v_s for samples with the ratio d/P_0 1, 2.5, 4, 9.5, 19, and 20 (curves 1–6) at 3.2 MHz. These data exhibit a distinct

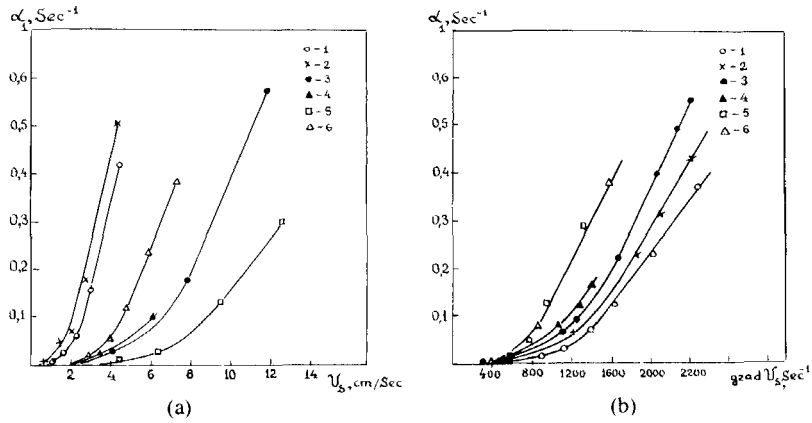

FIGURE 90 Effect of particle velocity (a) and particle velocity gradient (b) on the switching-on time of dynamic light scattering with memory for samples with different d/P_0 values. Details in the text.

correlation: for a constant particle velocity the higher the helical pitch, the larger is the decay of α_1 with increasing layer thickness. Representing these data as plots of α_1 versus particle velocity gradient, we see that curves 1–6 steadily move away from the abscissa axis as the parameter d/P_0 increases, i.e. the time constant α_1 rises (Figure 90b; notation the same as in Figure 90a). It was found that α_1 and d/P_0 are related by

$$\alpha_1 = A\exp(Bd/P_0) \tag{125}$$

where A and B are constants. For a mixture of LC-404 nematic and cholesteryl caprinate grad $v_s = 1300\ s^{-1}$, $A = 0.05\ s^{-1}$, $B = 0.08$.[144] The parameter $\tau_1 = 1/\alpha_1$ shows the "responsiveness" of scattering with memory.

It should be noted that the memory effect is not observed for small-duration deformations. In this case, after deformation ceases the scattering texture spontaneously turns into a transparent planar texture, and $\tilde{k}_0$ relaxes to the initial attenuation coefficient $\tilde{k}_1$. This is confirmed by curves 1–3 in Figure 91 which show the behaviour of $\tilde{k}$ after switching off the field applied for 5, 30, and 120 s, respectively; $f = 3.2$ MHz, $v_s = 4.4$ cm/s, $d = 80\ \mu$m, $P_0 = 4\ \mu$m.

The portion of the kinetic curves corresponding to the decay of the attenuation coefficient (after the field is switched off) is described by

$$\tilde{k} - \tilde{k}_2 = (k_0 - k_2)\exp(-\alpha_2^* t) \tag{126}$$

where α_2^* is the time constant of the onset of a metastable state. It was found that

$$\alpha_2^* = C\exp(-Dd/P_0), \tag{127}$$

which is evidenced by Figure 92 showing the kinetics of the metastable state

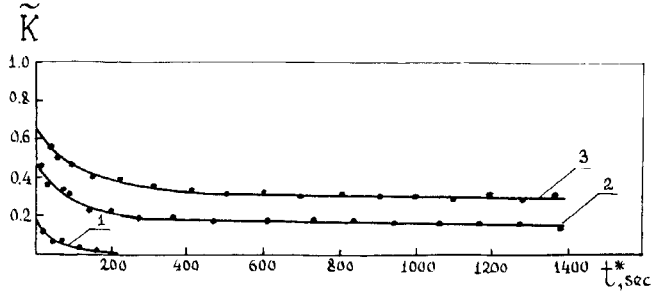

FIGURE 91 Effect of irradiation time t^* on the metastable state kinetics: curves 1–3 correspond to $t^* = 5$, 30, and 120 s.

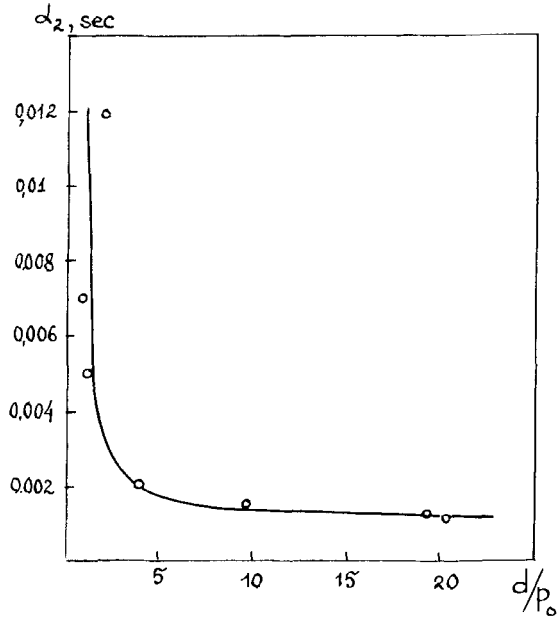

FIGURE 92 The time constant of the metastable state kinetics as a function of the structural parameter d/P_0.

in samples with different d and P_0 after switching off the field with grad $v_s = 1300\ s^{-1}$; $f = 3.2$ MHz.[144] It can be seen that the metastable state is established for several minutes.

The data concerning the time characteristics of dynamic scattering in samples with homeotropic boundary conditions are listed in Table III. They were obtained from the kinetic curves for a mixture of LC-404 nematic and cholesteryl caprinate (concentration of the optically active component is 5%); $f = 3.2$ MHz.[116] It should be noted that in this case the "lifetime" of the scattering texture is no more than 1 min. As the sample thickness

TABLE III

Effect of layer thickness and helical pitch on the response and relaxation times

d, μm	P_0, μm	d/P_0	τ_1 s	τ_2 s	T °C
10	3	3	29	54	29.8
40	3	13	40	56	26.1
40	3	13	30	62	29.8
40	3	13	18	70	30
80	3	27	35	—	29.8

increases (P_0 = const), τ_1 and τ_2 increase little. When the sample is heated its time characteristics are improved slightly.

V. EFFECT OF TEMPERATURE

In this section we shall focus on two of the most interesting and practically important aspects of the influence of temperature on the optical behaviour of liquid crystals under mechanical deformation: the formation (in a certain temperature régime) of optical phase gratings with a controlled period; thermal analysis of acoustic fields.

V.1. Memory effects under the nematic–smectic phase transition in a non-uniformly heated sample

Second-order phase transitions as well as weak first-order transitions are accompanied with a thermal anomaly of many physical properties of a system. In this case, the second thermodynamic derivatives, including the compressibility modulus, K_0,[169] experience a sharp change near the phase transition point T_c. A similar effect is observed under the transition from the nematic to the A smectic phase. Impurities present in the system (in this case in the nematic phase) relax the temperature singularities: for example, the modulus K_0 has a finite minimum at T_c.[170] On both sides of this point under homogeneous temperature distribution in a sample the derivative $\partial K_0/\partial T$ has large finite values; far from the point T_c the derivative $\partial K_0/\partial T$ is small.

It has been found recently that in mesomorphic samples with nematic and A smectic phases subjected to compression deformation under inhomogeneous temperature distribution along the layer there arise steady-state spatial-modulated structures with a controlled period.[171]

Experiments were performed with homeotropic samples of $p-n$-hexyloxyphenyl ester of n-decyl oxybenzoic acid. In this substance phase transformations proceed via the scheme

$$I \overset{85,5}{\longleftrightarrow} N \overset{81}{\longleftrightarrow} \mathrm{SmA} \overset{50}{\longleftrightarrow} \mathrm{SmC} \overset{44}{\longleftrightarrow} \mathrm{SmZ} \overset{35}{\longleftrightarrow} S.$$

The sample was melted between glass substrates in the isotropic state, and visual observations were made in polarized light (crossed polarizers) as the sample cooled down.

As the temperature decreases, one of the layer edges, depending on the temperature gradient along the substrate, reveals a nematic region; its size

grows with time (as the samples cool down) and eventually the entire sample becomes involved in the phase transition to form a single crystal (under appropriate boundary conditions). If such a sample is subjected to compression, its structure is modified, the result being dependent on how close the layer temperature is to the nematic–A smectic transition point. If the temperature is far from the transition point, compression gives rise to layer clearing; after deformation ceases, homeotropic orientation is rapidly restored. On the contrary, near the transition point the sample reveals (after deformation ceases) defective zones of residual perturbation in the form of bright parallel fringes against the dark background. The number of fringes depends on the compression frequency and the rate of temperature variation along the layer, and their width depends on the intensity and duration of the compression. Short and weak compression results in narrow fringes and prolonged compression in wide ones. The zone structure is inhomogeneous and consists of a black filament surrounded by a white halo.

It should be noted that although the layer is compressed over the whole sample plane, defective fringes arise only in a certain area determined by a time-dependent temperature distribution along the layer. In this area the titled molecules do not return to the initial homeotropic orientation, for the substance viscosity increases with the formation of the A phase, and are as if "frozen" in. In the smectic area of the sample the tilt of the molecules does not change under compression. On the other side of a defective fringe, where the nematic phase still exists, compression produces other defective zones in the areas where the temperature reaches a critical value.

Further cooling of the sample leads to the SmA → SmC phase transition; first, the fringes completely disappear and in several minutes the sample reveals a particolored fringe texture. A deeper cooling results in the transition from the C to the Z phase. After this phase transformation the fringe pattern is again fully visualized. On still deeper cooling, when the sample becomes solid, the pattern remains unchanged. Heating the sample, we can observe all the above-mentioned textures, defective fringes being "erased" only in the isotropic state.

These features of the behaviour of mesomorphic substances have a clear physical nature. Imagine that a constant temperature gradient $dT/dx = a$ exists in the layer plane along the x-axis. Then the modulus $K_0(x)$ is inhomogeneous in the same direction: $\partial K_0/\partial x = a\,\partial K_0/\partial T$. Assuming a homogeneous layer deformation $\Delta V/V_0$, we obtain an inhomogeneous pressure distribution $P(x)$ due to $K_0(x)$.† Thus, compression of an inhomoge-

†Pressure P in a medium related to deformation $\Delta V/V_0$ by $P = -K_0(\Delta V/V_0) + P_0$ where ΔV is the change in volume $V - V_0$ for $P > P_0$.

neously heated liquid crystal gives rise to the bulk force

$$f(x) = -\frac{\partial P}{\partial x} = a\left(\frac{\Delta V}{V_0}\right)\frac{\partial K_0}{\partial T}, \tag{128}$$

which makes the substance to move at a velocity $v(x, z)$. This velocity satisfies the Navier-Stokes equation

$$\alpha_0\left(\frac{\partial^2 v}{\partial x^2} + \frac{\partial^2 v}{\partial z^2}\right) + f(x) = 0, \tag{129}$$

where α_0 is the mean viscosity. When the characteristic distance $x = x_0$ at which the force $f(x)$ changes significantly is much larger than the layer thickness d, Eq. (129) takes the form

$$\alpha_0\frac{\partial^2 v}{\partial z^2} + f = 0. \tag{130}$$

Taking into account the boundary conditions $v(x, -d/2) = v(x, d/2) = 0$, we obtain

$$v(x, z) \approx \frac{f(x)}{2\alpha_0}\left(\frac{d^2}{4} - z^2\right). \tag{131}$$

This velocity distribution leads to an orientation deformation of a nematic approximately described by the equation

$$K_3\frac{\partial^2 \varphi}{\partial z^2} \approx \alpha_2\frac{\partial v}{\partial z}. \tag{132}$$

For strong adhesion this equation gives

$$\varphi(x, z) \approx \frac{\alpha_2 f(x)}{6\alpha_0 K_3}\left(\frac{d^2}{4} - z^2\right)z, \tag{133}$$

whence it follows that the maximal director tilt $\varphi_{\max}$ occurs at $z = d/2\sqrt{3}$, i.e. at $\approx 0.2d$ from the substrate surface.† As regard the longitudinal direction (x), the larger the derivative $\partial K_0/\partial T$, the greater is the tilt φ. The angle φ is proportional to the deformation $\Delta V/V_0$ and the temperature gradient a.

†For weak adhesion the tilt is maximal just near the layer surface.

It should be noted that the process remains steady until the hydrodynamic relaxation time exceeds the time of the action of the force $f(x)$. Since in the experiment the point x_c giving the position of T_c moves with time, an increased duration of the force $f(x)$ leads to an expanded defective fringe. The higher the velocity dx_c/dt, the larger is the probability of "freezing" of the defects (disinclinations and dislocations) in the smectic phase. The "warmer" part of the fringe contains a greater amount of defects, since in this region the derivative $\partial K_0/\partial T$ is higher. The central part of the fringe remains virtually unperturbed (dark) because here the total force $f(x_c) = 0$. The "storage" of a fringe structure in low-temperature smectic and solid phases is caused by the relative stability of the defects which are completely "annealed" only in the isotropic phase.

V.2. Thermooptical properties of cholesteric crystals

In many cholesteric crystals the helical pitch is known to be rather sensitive to temperature change, so that the wavelength and intensity of selective light reflection do depend on temperature.[172] This effect is significant for various practical applications of cholesteric crystals such as non-destructive testing and visualization of various thermal fields. In particular, if the field is produced as a result of the absorption of acoustic energy in the substrate on which a liquid crystal is deposited, this substrate should provide a local rise in the layer temperature sufficient for color transition.†

The performance of a detector of acoustic energy employing cholesteric crystals depends on the thickness, heat capacity, heat conductivity, and spectral absorption of the substrates. To enhance the sensitivity, the substrates are coated with special layers that strongly absorb sound. Experimental data now available show that cholesteric crystals are used to visualize acoustic fields in gases,[173-176] liquids,[177-180] and solids[181-183] in the frequency range from hundreds of Hz to several GHz.

The resolution of the method and the time the visualized image persists in the layer depend on thermal diffusion in the absorber. If the absorbing layer represents a disk of infinite radius, and a thermal pulse is applied at $t = 0$ at the disk centre, the temperature will drop e times (as compared with that at the centre) at a distance of $r(t) = 2/b\sqrt{t}$, where b is the constant in the heat conduction equation. Estimates show that for $b^2 = 3 \cdot 10^3$ s/cm^2 r amounts

†Most cholesterics and their mixtures are characterized by short-wavelength shift of the selective reflection wavelength with increasing temperature, the temperature coefficient $\Delta\lambda^s/\Delta T$ exhibiting extremely different values. The highest value of $\Delta\lambda^s/\Delta T$ is observed in cholesteryl erucyl carbonate. For this substance the selective reflection wavelength spans the entire visible spectrum region with the temperature changing by 0.2°C. On the contrary, the temperature coefficient of cholesteryl pelargonate at 74–75°C is about several thousands of Angströms per degree.

to 0.03 and 0.11 cm for $t = 1$ and 10 s, respectively.[177] Thus, thermal diffusion imposes certain restrictions on the image obtained, so that observations should be performed for short time periods and the sample temperature should be kept close to the color transition point.

Cholesteric crystals do not only permit the visualization of an acoustic field itself, but also of objects placed in this field.[177] Experiments on the visualization of acoustic holograms by cholesteric crystals have been described in Ref. 180. Experiments have also been described on the visualization of the fields of acoustic transducers.[178,179,181-183]

An important advantage of this visualization technique is the possibility of obtaining a colored image of an object, the color depending on the signal amplitude and carrying additional information for interpreting the observed pattern.

CONCLUSION

Great progress has recently been made in theoretical and experimental studies of the effect of mechanical deformations on the optical properties of liquid crystals. Among the various types of liquid crystals, nematic crystals have been investigated most comprehensively, although even for these substances many interesting problems remain to be solved: the mechanism of the formation of spatially modulated structures when the viscous wavelength is much smaller than the layer thickness (high-frequency acoustohydrodynamic instability); a detailed study of the effect of surface acoustic waves; theoretical and experimental investigations of acoustical dynamic light scattering; etc.

Virtually no systematic research has been made, so far, in the optical behaviour of cholesteric and smectic crystals. Though a large amount of experimental data is now available, theoretical and numerical estimates are rather scanty and refer mainly to orientation processes in these phases. For example, it would be interesting to study the formation of a metastable state in these phases and elucidate the mechanism of the formation of spatially periodic structures. As was pointed out above, the efficiency of acoustooptical conversion, as well as the evolution of the optical signal under crystal structure distortion due to mechanical deformation, largely depend on the nature of the phenomenon which controls the orientation process. Theoretical and empirical estimates performed so far are usually based on rather crude models; nevertheless, they agree sometimes with experimental results, thereby indicating that these models correctly describe the phenomenon.

A large number of papers have recently been published which deal with the practical applications of the acoustooptical properties of liquid crystals.

Investigations have shown that liquid-crystal acoustooptical devices may control all the parameters of a light beam (amplitude, polarization, spectral composition, propagation direction) and process information carried both by an acoustic wave and a light wave. Liquid-crystal acoustooptical converters can successfully operate as modulators,[48-51,53-55] scanners,[105,108] visualizers of acoustic fields,[3,29,35,43,44,46,110,114,173-189] microphones,[190] seismosensors,[150] and detectors of mechanical deformations.[9] The active element of all these devices is an acoustooptical cell which consists of a "working body," i.e. a liquid crystal where light interacts with an acoustic wave, and a sound source. These topics require an independent study and have not been touched upon in the review.

It should be noted that not every aspect of the problem has been given equally comprehensive coverage. The main attention has been paid to nematics, for precisely these substances have been studied at present most thoroughly. The effect of external (electric and magnetic) fields[13,19,46,146,183,191] is ignored, though, according to recent data,[192] rather interesting practical applications may be expected in this direction. Seemingly, of not less importance is the study of optical behaviour of the mesophase in the phase transition region[6,7,45] and in the isotropic phase.[193,194] These topics are also the subject of independent discussions.

References

1. I. A. Viktorov, E. K. Grishchenko, and T. M. Kayokina, *Acoust. Zhurnal*, **9**, 162 (1963).
2. K. Miyano and J. R. Shen, *Appl. Phys. Lett.*, **28**, 473 (1976).
3. J. N. Perbet, M. Hareug, S. Le Berre, and B. Mourrey, *Revue Technique Tomson-CSF*, **11**, 837 (1979).
4. O. A. Kapustina, E. N. Kozhevnikov, and G. N. Yakovenko, III All-Union Symposium on the Physics of Acoustohydrodynamic Phenomena and Acoustooptics (abstracts), 11, Tashkent (1982) (in Russian).
5. O. Lehman, *Das Kristallisationsmicroscop und die damit gemachten Endeckungen insbesondere die flussigen Kristalle* (Braunschweige, 1910).
6. A. P. Kapustin, Z. Kh. Kuvatov, and A. I. Trofimov, *Izvestiya Vysshikh Uchebnykh Zavedenii, Fizika*, **4**, 150 (1971).
7. A. P. Kapustin, Z. Kh. Kuvatov, and A. I. Trofimov, *Uchenye Zapiski Ivanovskogo Gosudarstvennogo Pedagogicheskogo Instituta*, **99**, 64 (1972).
8. V. V. Zolina, *Trudy Lomonosovskogo Instituta AN SSSR*, **8**, 11 (1936).
9. A. P. Kapustin, Bulleten' Izobretenii i Otkrytii 25, No. 224102 (1968).
10. A. Kapustin and O. Kapustina, *Kristall und Technik*, **8**, 1 (1973).
11. M. Born and E. Wolf, *Principles of Optics* (Nauka, Moscow, 1970) (Russian translation).
12. *Physics and Chemistry of the Action of Ultrasound on Interfacial Surfaces*, Ed. by Abramov (Nauka, Moscow, 1983) (in Russian).
13. W. Helfrich, *Phys. Rev. Lett.*, **29**, 1583 (1972).
14. S. Nagai and K. Izuka, *Jap. J. Appl. Phys.*, **13**, 189 (1974).
15. I. A. Chaban, *Acoust. Zhurnal*, **25**, 124 (1979).
16. J. L. Dion and A. D. Jacob, *Appl. Phys. Lett.*, **31**, 490 (1977).

17. J. L. Dion, *C. R. Hebd, Séan. Acad. Sci.*, **284**, B-219 (1977).
18. H. Bruchmüller, *Acustica*, **40**, 155 (1978).
19. S. Nagai, A. Peters, and S. Candau, *Revue de Physique Appliquée*, **12**, 21 (1977).
20. L. Landau and E. Lifshits, *Mechanics of Continuous Media* (Moscow, Gostekhizdat, 1954) (in Russian).
21. S. A. Pikin, *Structural Transformations in Liquid Crystals* (Nauka, Moscow, 1981) (in Russian).
22. O. A. Kapustina and Yu. G. Statnikov, *Zh. Eks. Teor. Fiz.*, **66**, 635 (1974).
23. Ch. Sripaipan, Ch. F. Hayes, and G. T. Fang, *Phys. Rev. A*, **15**, 1297 (1977).
24. L. K. Zarembo and V. A. Krasil'nikov, *Introduction to Non-linear Acoustics*, (Nauka, Moscow, 1966) (in Russian).
25. E. N. Kozhevnikov, *Acoust. Zhurnal*, **27**, 533 (1981).
26. E. N. Kozhevnikov, *Zh. Eks. Teor. Fiz.*, **82**, 161 (1982).
27. N. K. Gus'kov and E. N. Kozhevnikov, *Acoust. Zhurnal*, **29**, 38 (1983).
28. E. Guyon and P. Pieranski (see thesis J. Lebrun, Univ. L. Pasteur, Strasbourg, 1978).
29. O. A. Kapustina and V. N. Lupanov, *Acoust. Zhurnal*, **23**, 390 (1977).
30. T. Hatakeyama and I. Kagawa, *J. Acoust. Soc. Japan*, **32**, 92 (1976).
31. T. Hatakeyama and I. Kagawa, *J. Sound and Vibr.*, **46**, 551 (1976).
32. J. L. Dion, *C. R. Hebd. Séan. Acad. Sci.*, **286**, B-383 (1978).
33. J. L. Dion, *J. Appl. Phys.*, **50**, 2965 (1979).
34. J. L. Dion, R. Simard, A. D. Jacob, and A. Leblanc, Ultrasonic Symposium, Proceedings (New Orleans, 1979).
35. J. L. Dion, A. Leblanc, and A. D. Jacob, *Acoust. Imag.* (New York-London) **10**, 151 (1982).
36. A. E. Lord and M. M. Labes, *Phys. Rev. Lett.*, **25**, 570 (1970).
37. D. Forter, *Phys. Rev. Lett.*, **26**, 1016 (1971).
38. G. G. Natale, *J. Acoust. Soc. Amer.*, **63**, 1265 (1978).
39. E. N. Kozhevnikov, *Acoust. Zhurnal*, **28**, 136 (1982).
40. S. Candau, A. Ferre, A. Peters, G. Waton, and P. Pieranski, *Mol. Cryst. and Liq. Cryst.*, **61**, 7 (1980).
41. E. I. Zhukovskaya, E. N. Kozhevnikov, and V. M. Podolskii, *Zh. Eks. Teor. Fiz.*, **83**, 207 (1982).
42. J. Lebrun, Thesis, Univ. L. Pasteur (Strasbourg, 1978).
43. J. N. Perbet, M. Hareng, and S. Le Berre, *Revue de Physique Appliquée*, **14**, 569 (1979).
44. J. Lebrun, S. Candau, and S. Letcher, *J. Physique*, **40**, C3-298 (1979).
45. S. Letcher, J. Lebrun, and S. Candau, *J. Acoust. Soc. Amer.*, **63**, 55 (1978).
46. S. Nagai and K. Iizuka, *Mol. Cryst. and Liq. Cryst.*, **45**, 83 (1978).
47. S. Nagai and K. Iizuka, *Jap. J. Appl. Phys.*, **17**, 723 (1978).
48. A. P. Kapustin, *Kristallografiya*, **14**, 943 (1969).
49. O. A. Kapustina, 7th All-Union Acoustic Conf. (abstracts), Leningrad, 1971 (in Russian).
50. M. Bertolotti, S. Martellucei, F. Scudieri, and D. Sette, *Appl. Phys. Lett.*, **21**, 74 (1972).
51. R. Bartolino, M. Bertolotti, F. Scudieri, D. Sette, and A. Sliwinski, *J. Appl. Phys.*, **46**, 1928 (1982).
52. E. N. Kozhevnikov, *Acoust. Zhurnal*, **28**, 238 (1982).
53. Yu. N. Korolev and G. N. Yakovenko, *Acoust. Zhurnal*, **29**, 783 (1977).
54. V. D. Svet and G. N. Yakovenko, *Acoust. Zhurnal*, **26**, 151 (1980).
55. G. N. Belova, E. I. Remizova, and G. N. Yakovenko, 4th Conf. of Socialist Countries on Liquid Crystals (abstracts), 26 (Tbilisi, 1981) (in Russian).
56. N. I. Galaktionov, V. V. Gershun, A. A. Kalmychek, A. A. Mak, O. A. Orlov, and V. I. Ustyugov, *Pis'ma v Zh. Eks. Teor. Fiz.*, **4**, 1001 (1978).
57. O. A. Kapustina, E. N. Kozhevnikov, and G. N. Yakovenko, XI All-Union Conf. on Coherent and Non-linear Optics (abstracts) (Erevan, 1982) (in Russian).
58. O. Kapustina, E. Kozhevnikov, and G. Yakovenko, Abstracts of the 11th Intern. Congress on Acoustics (Paris, 1983).
59. O. A. Kapustina, E. N. Kozhevnikov, and G. N. Yakovenko, 4th Conf. of the Socialist Countries on Liquid Crystals (abstracts), 62 (Tbilisi, 1981) (in Russian).

60. O. A. Kapustina, E. N. Kozhevnikov, and G. N. Yakovenko, *Zh. Eks. Teor. Fiz.* (to be published).
61. O. A. Kapustina, Yu. G. Statnikov, *Zh. Eks. Teor. Fiz.*, **20**, 248 (1974).
62. G. Jeffris, B. Svirs, *Methods of Mathematical Physics* (Mir, Moscow, 1969) (Russian translation).
63. N. A. Tolstoi and A. N. Fedotov, *Zh. Eks. Teor. Fiz.*, **17**, 564 (1947).
64. E. N. Kozhevnikov and I. A. Chaban, *Acoust. Zhurnal*, **21**, 900 (1975).
65. O. A. Kapustina and A. A. Talashev, *Acoust. Zhurnal*, **19**, 626 (1978).
66. K. Miyano and I. K. Shen, *Appl. Phys. Lett.*, **28**, 473 (1976).
67. L. E. Davis and J. Chambers, *Electronic Letters*, **7**, 287 (1971).
68. T. E. Worth, W. G. B. Britton, and R. W. B. Stephens, Ultrasonic Intern. Conf. Proceedings (London 1975), 120.
69. J. S. Sandhu, W. G. B. Britton, and R. W. B. Stephens, 9th Int. Congress on Acoustics. Proceedings (Madrid, 1977).
70. J. S. Sandhu, W. G. B. Britton, and R. W. B. Stephens, Acoustics '80, Spring Conf., Proceedings (London, 1980).
71. S. Sato and H. Ueda, *Jap. J. of Appl. Phys.*, **20**, L511 (1981).
72. Y. Kagawa and T. Hatakeyama, *J. Sound and Vibr.*, **41**, 1 (1975).
73. Y. Kagawa and T. Hatakeyama, *J. Acoust. Soc. of Japan*, **31**, 81 (1975).
74. P. G. De Gennes, *The Physics of Liquid Crystals* (Clarendon Press, Oxford, 1974).
75. V. K. Kondratenko, M. M. Farztdinov, A. N. Chuvyrov, *Fiz. Tverd. Tela*, **17**, 795 (1975).
76. Ch. Gähwiller, *Phys. Letters*, **A36**, 311 (1971).
77. J. Wähl and F. Fisher, *Optic Commun.*, **5**, 341 (1972).
78. S. Meiboom and R. H. Hewitt, *Phys. Rev. Lett.*, **30**, 261 (1972).
79. P. Pieranski and E. Guyon, *Solid State Commun.*, **13**, 435 (1973).
80. P. Pieranski and E. Guyon, *Phys. Rev.*, **A9**, 404 (1974).
81. P. Manneville and E. Dubois-Violette, *J. Phys.*, **37**, 285 (1976).
82. E. Dubois-Violette, E. Guyon, I. Janossy, P. Pieranski, and P. Manneville, *J. Méchanique*, **16**, 733 (1977).
83. F. M. Leslie, *J. Phys.*, **D9**, 925 (1976).
84. G. E. Zvereva and A. P. Kapustin, *Application of Ultraacoustics to the Study of Matter* (MOPI, Moscow, 1961), No. 15, 69 (in Russian).
85. A. P. Kapustin and L. M. Dmitriev, *Kristallografiya*, **7**, 332 (1962).
86. P. Manneville, *J. Phys.*, **37**, 285 (1976).
87. E. Guyon and P. Pieranski, *J. Phys.*, **36**, CI-203 (1975).
88. I. Janossy, P. Pieranski, and E. Guyon, *J. Phys.*, **37**, 1105 (1976).
89. P. Pieranski and E. Guyon, *Phys. Rev. Lett.*, **39**, 1280 (1977).
90. M. Clark, F. Saunders, I. Shanks, and F. Leslie, *Mol. Cryst. and Liq. Cryst.*, **70**, 195 (1981).
91. F. Scudieri, *Appl. Phys. Lett.*, **29**, 398 (1976).
92. I. A. Chaban, *Acoust. Zhurnal*, **24**, 260 (1978).
93. F. Scudieri, *Ann. Phys.*, **3**, 311 (1978).
94. F. Rothen and E. Dubois-Violette, *J. Phys.*, **38**, 1039 (1978).
95. J. M. Dreyfus and E. Guyon, *J. Phys.*, **42**, 283 (1981).
96. J. M. Dreyfus, P. Pieranski, and E. Guyon, Poster Session in the 7^{eme} Congrès Int. sur les Crystaux Liquides, (Bordeaux, 1978).
97. J. Sadik, F. Rothen, and W. Bestgen, *J. Phys.*, **42**, 915 (1981).
98. E. Guazzelli and E. Guyon, *J. Phys.*, **43**, 985 (1982).
99. E. Guazzelli and E. Guyon, *C. R. Hebd. Séan. Acad. Sci.*, **292**, 142 (1981).
100. E. Guazzelli, Thèse 3^{eme} cycle., Univ. Paris-Sud (1981).
101. F. Scudieri, A. Ferrari, and D. Apostol, *Rev. Roum. Phys.*, **21**, 677 (1976).
102. M. Bertolotti, F. Scudieri, and E. Sturla, *J. Appl. Phys.*, **49**, 3922 (1978).
103. F. Scudieri, M. Bertolotti, S. Melone, and G. Albertini, *J. Appl. Phys.*, **47**, 3781 (1976).
104. Ch. Gähwiller, *Mol. Cryst. and Liq. Cryst.*, **20**, 301 (1973).
105. E. Guyon, I. Janossy, P. Pieranski, and J. M. Jonatan, *J. Optics*, **8**, 357 (1977).
106. V. N. Reshetov, 4th Conf. of the Socialist Countries on Liquid Crystals (abstracts), 187 (Tbilisi, 1981) (in Russian).

107. V. N. Reshetov, O. A. Kapustina, and G. N. Yakovenko, 3d All-Union Symp. on the Physics of Acoustohydrodynamic Phenomena and Optoacoustics (abstracts), 12 (Tashkent, 1982) (in Russian).
108. V. N. Reshetov, 11th All-Union Conf. on Coherent and Non-linear Optics (abstracts) 764 (Erevan, 1982) (in Russian).
109. P. Manneville, *J. Phys.*, **49**, 713 (1979).
110. O. A. Kapustina and V. N. Lupanov, *Zh. Eks. Teor. Fiz.*, **71**, 2324 (1976).
111. O. A. Kapustina and V. N. Lupanov, 4th Conf. of the Socialist Countries on Liquid Crystals (abstracts) (Tbilisi, 1982) (in Russian).
112. L. W. Kessler and S. P. Sawyer, *Appl. Phys. Lett.*, **17**, 440 (1970).
113. G. W. Smith, *Advances in Liquid Crystals* (New York, 1975).
114. O. Kapustina and V. Lupanov, *Wiss. Z. Univ. Halle*, **24**, 49 (1977).
115. I. Gurova, O. Kapustina, and V. Lupanov, *Advances in Liquid Crystal Research and Applications* (Pergamon Press. Oxford—Akadémiai Kiado, Budapest, 1980).
116. M. Zulauf, M. Bertolotti, and F. Scudieri, *J. Phys.*, **36**, CI-265 (1970).
117. L. P. Bochkov, B. M. Bolotin, O. A. Kapustina, and V. N. Lupanov, Abstracts of the Eighth Int. Liq. Crystal Conference, 390 (Kyoto, 1980).
118. B. M. Krasovitskii and E. A. Shevchenko, *Khimiya Geterotsiklicheskikh Soedinenii*, **4**, 756 (1968).
119. A. P. Kapustin, *Izv. Vysshikh Uchebnykh Zavedenii, Fizika*, **11**, 55 (1967).
120. J. L. Fergason, *Scientific American*, **211**, 76 (1964).
121. P. Pollmann and H. Stegemeyer, *Chem. Phys. Lett.*, **20**, 87 (1973).
122. Ya. I. Frenkel, *Kinetic Theory of Liquids* (Nauka, Moscow, 1975) (in Russian).
123. B. Böttcher, *Chem. Zeit.*, **96**, 214 (1972).
124. J. D. Bernal and D. Crowfoot. *Trans. Faraday Soc.*, **29**, 1032 (1933).
125. R. Bartolino, F. Simoni, and N. Scaramuzza. *Mol. Cryst. and Liq. Cryst.*, **70**, 315 (1981).
126. N. Scaramuzza, R. Bartolino, and G. Berbero, *J. Appl. Phys.*, **53**, 8593 (1982).
127. S. Mazkedian, S. Melone, and F. Rustichelli, *J. Phys.*, **36**, CI-283 (1975).
128. R. Bartolino and G. Durand, *Phys. Rev. Lett.*, **39**, 1346 (1977).
129. J. M. Pochan and P. F. Erhardt, *Phys. Rev. Lett.*, **27**, 790 (1971).
130. E. J. Klein and A. P. Margozzi, *Rev. Sci. Inst.*, **41**, 238 (1970).
131. L. Melamed, *J. Opt. Soc. Amer.*, **61**, 1551 (1971).
132. D. F. Ciliberti, G. D. Dixon, and L. C. Scala, *Mol. Cryst. and Liq. Cryst.*, **20**, 27 (1973).
133. J. M. Pochan and D. S. Marsh, *J. Chem. Phys.*, **57**, 1193 (1972).
134. J. M. Pochan and D. S. Marsh, *J. Chem. Phys.*, **57**, 5154 (1972).
135. J. M. Pochan and D. S. Marsh, *J. Chem. Phys.*, **58**, 2835 (1973).
136. F. M. Leslie, *Mol. Cryst. and Liq. Cryst.*, **7**, 407 (1969).
137. U. D. Kini, *J. Phys.*, **40**, C3-62 (1979).
138. J. Prost, *J. Phys.*, **39**, 639 (1978).
139. I. Janossy, *Advances in Liquid Crystal Research and Applications* (Pergamon Press, Oxford —Akadémiai Kiado, Budapest, 1980), 625.
140. I. Janossy, *J. Phys.*, **41**, 437 (1980).
141. J. P. Hurault, *J. Chem. Phys.*, **59**, 2068 (1973).
142. L. Bata and I. Janossy, Poster Session in the 7^{eme} Congrès Int. sur les Crystaux Liquides (Bordeaux, 1978).
143. I. Gurova, O. Kapustina, V. Loupanov, and G. Chilaya, Poster Session in the 7^{eme} Congrès Int. sur les Crystaux Liquides (Bordeaux, 1978).
144. O. A. Kapustina, *Acoustooptical Properties of Liquid Crystals and their Application* (Acoustics' Institute of the Academy of Sciences of the USSR, Moscow, 1979) (in Russian).
145. K. Hiroshimo and H. Shimizu, *Jap. J. Appl. Phys.*, **16**, 1889 (1977).
146. O. A. Kapustina and V. N. Lupanov, 2nd Conf. of the Socialist Countries (abstracts) (Bulgaria, 1977), 62.
147. W. Haas and J. Adams, *Appl. Phys. Lett.*, **25**, 535 (1974).
148. M. J. Press and A. S. Arrott, *J. Phys.*, **37**, 987 (1976).
149. M. Bertolotti, L. Sbrolli, and F. Scudieri, *Advances in Liquid Crystal Research and Applications* (Pergamon Press, Oxford—Akadémiai Kiado, Budapest, 1980), 433.

150. M. Bertolotti, L. Sbrolli, and F. Scudieri, *J. Appl. Phys.*, **53**, 4750 (1982).
151. V. G. Bhide, S. Chandra, S. C. Jain, and R. L. Medhekar, *J. Appl. Phys.*, **47**, 120 (1976).
152. C. Obayashi, *Jap. J. Appl. Phys.*, **20**, 1753 (1981).
153. I. Gurova, O. Kapustina, and V. Lupanov, Abstracts of the Eighth Int. Liquid Crystal Conference, 163 (Kyoto, 1983).
154. I. N. Gurova, O. A. Kapustina, and V. N. Lupanov, 4th Conf. of the Socialist Countries on Liquid Crystals (abstracts) (Tbilisi, 1981) (in Russian).
155. N. Nawa and K. Nakamura, *Jap. J. Appl. Phys.*, **17**, 219 (1978).
156. F. Scudieri, A. Ferrari, and E. Gündüz, *J. Phys.*, **40**, C3-90 (1979).
157. R. Ribotta and G. Durand, *J. Phys.*, **38**, 179 (1977).
158. R. Ribotta, G. Durand, and J. D. Litsher, *Solid State Commun.*, **12**, 27 (1973).
159. O. A. Kapustina, V. N. Lupanov, and V. M. Shoshin, *Acoust. Zhurnal*, **26**, 718 (1979).
160. O. A. Kapustina, V. N. Lupanov, and G. S. Chilaya, *Acoust. Zhurnal*, **24**, 136 (1978).
161. R. B. Meyer, L. Liébert, and L. Strzelcki, *J. Phys. Letters*, **36**, 69 (1975).
162. Pawel Pieranski, E. Guyon, and P. Keller, *J. Phys.*, **36**, 1005 (1975).
163. Pawel Pieranski, E. Guyon, P. Keller, L. Liébert, W. Kuczynski, and Piotr Pieranski, *Mol. Cryst. and Liq. Cryst.*, **38**, 275 (1977).
164. D. Taupin, E. Guyon, and P. Pieranski, *J. Phys.*, **39**, 406 (1978).
165. B. I. Ostrovskii, A. Z. Rabinovich, and A. S. Sonin, *Zh. Eks. Teor. Fiz.*, **74**, 1748 (1978).
166. P. C. Martin, O. Parodi, and P. S. Pershan, *Phys. Rev.*, **6**, 2401 (1972).
167. I. N. Gurova, O. A. Kapustina, and V. N. Lupanov, *Proc. of the 2nd All-Union Symp. on the Physics of Acoustohydrodynamic Phenomena and Optoacoustics* (Suzdal, 1979), 60 (Nauka, Moscow, 1982) (in Russian).
168. O. A. Kapustina, V. N. Lupanov, and G. S. Chilaya, The 2nd Conf. of the Socialist Countries on Liquid Crystals (abstracts) (Bulgaria, 1977), 64.
169. A. I. Larkin and S. A. Pikin, *Zh. Eks. Teor. Fiz.*, **56**, 1664 (1969).
170. A. P. Kapustin, *Experimental Investigation of Liquid Crystals* (Nauka, Moscow, 1978) (in Russian).
171. A. P. Kapustin and S. A. Pikin, *Pis'ma v Zh. Eks. Teor. Fiz.*, **33**, 332 (1981).
172. V. A. Belyakov and A. S. Sonin, *The Optics of Cholesteric Liquid Crystals* (Nauka, Moscow, 1982) (in Russian).
173. F. F. Legusha, E. V. Prokhorova, and V. G. Tishchenko, *Trudy LKI*, **109**, 74 (1976).
174. G. M. Ganichev, F. F. Legusha, and A. N. Slavin, *Acoust. Zhurnal*, **25**, 619 (1979).
175. F. F. Legusha, V. A. Murga, and A. N. Slavin, *Acoust. Zhurnal*, **29**, 84 (1983).
176. F. F. Legusha, *Zh. Tekhn. Fiz.*, **52**, 723 (1982).
177. W. H. Sproad and S. E. Cohen, *Mat. Evaluation*, **28**, 73 (1970).
178. B. D. Cook and R. E. Werchan, *Ultrasonics*, **9**, 101 (1971).
179. R. Denis, *Ultrasonics*, **16**, 37 (1978).
180. M. J. Inlekofer and D. C. Auth, *Appl. Phys. Lett.*, **20**, 151 (1972).
181. K. Izuka, *Proc. IEEE*, **58**, 288 (1970).
182. J. F. Havlice, *Electronics Letters*, **5**, 477 (1969).
183. Y. Kagawa and T. Hatakeyama, *J. Sound and Vibr.*, **36**, 407 (1974).
184. P. Greguss, *Acoustica*, **29**, 52 (1973).
185. O. A. Kapustina, *Acoust. Zhurnal*, **20**, 482 (1974).
186. O. A. Kapustina and V. N. Lupanov, Trudy 8 Vsesoyzn. Konf. po Nerazrushayushchim Metodam i Sredstvam Kontrolya (Proc. of the 8th All-Union Conf. on Non-destructive Testing) (Kishinev, 1977) (in Russian).
187. O. A. Kapustina and V. N. Lupanov, The 9th All-Union Conf. on Acoustics (abstracts), 37 (Moscow, 1977) (in Russian).
188. O. A. Kapustina and V. I. Lupanov, The 4th All-Union Conf. on Liquid Crystals and their Practical Application (abstracts), 134 (Ivanovo, 1977) (in Russian).
189. I. N. Gurova, O. A. Kapustina, and V. N. Lupanov, Proc. of the 3d Conf. on Information Acoustics (Moscow, 1977) (in Russian).
190. W. Hamidzada, S. Letcher, and S. Candau, *Acoust. Imag.* (New York-London) **10** (1982).
191. E. Vinogradova, O. Kapustina, V. Reshetov, V. Svet, and G. Yakovenko, *Acoust. Zhurnal* (to be published).

192. H. Mailer, K. L. Likins, T. R. Taylor, and J. L. Fergason, *Appl. Phys. Lett.*, **18**, 105 (1971).
193. H. Hakemi, *J. Appl. Phys.*, **53**, 6137 (1982).
194. E. V. Gevorkyan, *Acoust. Zhurnal*, **28**, 336 (1982).
195. A. N. Chuvyrov, *Zh. Eks. Teor. Fiz.*, **82**, 761 (1982).
196. P. Martinoty and M. Bader, Abstracts of the 9th Int. Liquid Crystal Conference (Kyoto, 1980).
197. P. Martinoty and M. Bader, *J. Phys.*, **42**, 1097 (1981).

Subject Index

Author Index